Modelling and Performance of a Hydrogel-Based Photobioreactor

by

Nicholas Rasmussen

A thesis
presented to the University of Waterloo
in fulfilment of the
thesis requirement for the degree of
Master of Applied Science
in
Chemical Engineering

Waterloo, Ontario, Canada, 2024

Author's Declaration

I hereby declare that I am the sole author of this thesis. This is a true copy of the thesis, including any required final revisions, as accepted by my examiners.

I understand that my thesis may be made electronically available to the public.

Abstract

This work is motivated by the need for in situ food production with respect to future space activities due to the technical and economic in-feasibility of long-term earth-based resupply. The unique size constraints of space have prevented conventional food systems from demonstrating feasibility. Owing to their high growth rates and phototropic activity, microalgae are a promising candidate to meet the caloric and respiratory needs of astronauts as part of a biological life support systems (BLSS). However, the gravity dependence and size of transitional photobioreactors poses a challenged to their utilization in space.

As such, a solid-state hydrogel-based photobioreactor (hPBR) is proposed to achieve inherent phase separation allowing for extra-terrestrial use. Initially proposed for the Canadian Space Agency (CSA) Deep Space Food Challenge (DSFC) (Design A), this design was further iterated to improve productivity and reactor performance (Design B). Using *Chlorella vulgaris*, Design B achieved a biomass productivity of 2.4 and 3.2 $g\ m^{-2}d^{-1}$ when using physically (pPVA) and chemically (cPVA) crosslinked poly(vinyl) alcohol (PVA) respectively with a water demand of 0.44 $kg\ g^{-1}$ biomass. Over 23 days of growth, the lipid content increased from 18.9% to 56.6% and 13.8% to 43.2% for pPVA and cPVA respectively, and the chlorophyll content also decreased. However, cell viability remained high at over 97% and surface coverage analysis showed good coverage within a few days.

Observations made with the prototype suggested mass transport limitations were impacting growth, and that poor humidity control led to the hydrogels drying out. To this end, a continuum model of the hydrogel was proposed to better understand mass transfer and to inform future design iterations. Hydrogels are two phase systems where the polymer is fixed due to crosslinking leading to a moving boundary with changes in water content. The proposed model did not require any parameter fitting as values were determined with independent experiments. The model enabled the prediction of the transient material response to changing relative humidity. This helped to explain why humidity control was critical in maintaining cell viability. Humidity impacted the water content of the gel's surface which needed to be high enough to support algae growth. Using the steady-state solution to the model, the solute transport through the system was also modelled. The solute profile suggested that nutrient concentrations throughout the hydrogel were similar to that in the media tank. This suggests nutrient supply was not the cause of the diminishing biomass quality and that other factors such as photo-inhibition, and mechanical stresses from solid-state cultivation may be issues to address in future work.

Acknowledgements

This thesis was supported financially by the Engineering Excellence Masters Fellowship from the University of Waterloo, Ontario Graduate Scholarship (OGS), the Natural Sciences and Engineering Research Council of Canada (NSERC), and the Canadian Space Agency/Impact Canada Deep Space Food Challenge. I would like to give a tremendous thank you to Dr. Ward and Dr. Abukhdeir for their guidance and support during my graduate studies. Additionally, I would like to thank my research peers for their wisdom, help, and stimulating conversations. In particular I would like to thank Alex Vasile, Christopher Sung, Mattherw Tino, Ittisak Promma, and Arshia Fazeli. For preliminary experimental work that formed the bases for some of this thesis, I would like to thank Craig Harrison and Hannah Czech. Finally, I would like to acknowledge my reviewers, Dr Yim, and Dr. Ioannidis, for their feedback and input on this thesis.

Dedication

I would like to dedicate this work to my parents, Elizabeth and Eric Rasmussen, for their continual support and advice along my academic journey and beyond.

Table of Contents

List of Figures

List of Tables

Chapter 1

Introduction

1.1 Motivation

Even before Yuri Gagarin took his maiden flight into space, there has been considerable interest in space exploration and building a permanent presence outside the confines of earth's atmosphere [1]. The push to develop space habitats suitable for sustaining life comes with a unique set of challenges. The ability to provide food, water, and a breathable atmosphere are some of many technical challenges paramount to realizing this goal. This problem is complicated by the cost and limited payload space available for space launches, meaning resource utilization is a key consideration for space systems [2].

When it comes to providing a liveable environment, the atmospheric composition is an important consideration. Carbon dioxide exhaled by the crew must be sequestered to avoid asphyxiation risk to the crew from the buildup of the compound [3]. Additionally, a reliable supply of oxygen must be provided to meet the metabolic needs of the crews. Respiration also leads to the exhalation of water vapor that will impact the humidity in a closed environment, and if left unchecked can lead to the proliferation of pathogens which can be detrimental to crew health [4].

Current life support systems in use onboard the International Space Station (ISS) depend on physiochemical technologies to recycle as much resources as possible. However, these systems fail to close the resource loop, and thus require regular resource inputs/outputs for operation [6]. This presents a challenge to future long-term space activities due to the

Figure 1.1: Mock up of ECLSS Racks on ISS [5]

high resupply cost and could potentially be infeasible as the space frontier gets pushed beyond the feasible resupply limit of earth.

Currently all food consumed in space needs to be launched at the beginning of the mission from earth. Freeze dried products help to limit the launch weight of consumables, but the long-term nutritional stability of freeze-dried products pose a challenge to long duration space activities [7]. Excess weight will impact the potential range for space missions due to the increased fuel requirement to move a larger mass of consumables leading to diminishing returns on investment.

Figure 1.2: Typical Meal Onboard the ISS [8]

Through the development of a bioregenerative life support system (BLSS), nature can be harnessed to meet the unique challenges of extraterrestrial exploration. There has been considerable interest in using plants and other organisms to reduce or eliminate the resource gap that exists in space systems with respect to food and oxygen [9]. The potential upside of such systems is that in situ food production can enable launch weight savings since less food must be initially carried from earth. Additionally, the use of photoautotrophs can enable the regeneration of oxygen improving environmental sustainability in the closed environment [10]. In a regenerative life support model, there are several subsystems that can be considered which essentially function as processes of coupled unit operations. Food production can be represented as a bioreactor model using growth kinetics. Additionally, oxygen and CO2 exchange can also be modelled using both reactor models and separation processes. Finally waste disposal and resource recovery can be represented by a series of unit operations, though this idea is not explored further in the current work.

Research into BLSS began well before the first crewed missions to space in the 1960s, highlighting the significant challenges life support poses to space exploration. The first large ground experiment was BIOS-I undertaken by the soviet space program. This experiment demonstrated the ability to use microalgae (*Chlorella vulgaris*) to meet the oxygen needs of one crew member. A $20L$ bioreactor with $8m^2$ of illuminated surface was enough to sustain one person for a duration up to 90 days [11]. Further ground experiments extended the BLSS system to include 3 crew members, and a variety of microalgae, plants and insects. Through the Biomass Production Chamber project, NASA successfully used a closed greenhouse system to grow crops for over 1,200 days on a footprint of $20m^2$ [9]. Current projects include the European Space Agency's MELiSSA initiative starting in 1988. This project aims to combine physio-chemical technologies with biology based systems to recycle waste, provide food and atmosphere regeneration [12]. Recent successes of this project include meeting the respiratory needs of three rats (5-10% of the needs of 1 person) using an 83 L PBR cultivating *Limmospira indica* (spirulina) for several months. [13].

The first algae experiment conducted in space, was the launch of *Euglena gracilis* on a Long March II rocket by China where the microorganisms survived the 4.5 day journey [9]. More recently in 2017, the Arthrospira-B experiment studied the online oxygen generation and growth rates of *Limnospira indica* onboard the ISS and was the first experiment of its kind. The bioreactors used consisted of two glass champers separated by a PTFE membrane and operated in batch conditions [14]. This experiment saw technical issues with the online measurements on board the ISS, however, it suggested that the oxygen evolution

rate were similar to that of the control ground experiments. The ESA's PBR@LSR project consisted of a micro-gravity-capable membrane raceway bioreactor that demonstrated operability of 188 days on earth. However during testing onboard the ISS in 2019, technical issues terminated the experiment after a few weeks[15]. Reliability and automation have been major obstacles faced by in situ experimentation of micro-gravity cultivation.

Terrestrially, microalgae are grown in traditional photobioreactor. In these technologies algae is grown in a liquid culture to which light is supplied. Due to light attenuation caused by cells shading one another, light only penetrates a limited distance into the cell suspension, therefore agitation is required to mix the cells to achieve high cell densities [9]. However, even with mixing only around 1-4 $g\ L^{-1}$ of biomass are present in culture [16]. The large volume of water required adds significant weight to the process making their use case for extraterrestrial applications less attractive. Additionally, carbon dioxide must be dissolved in the liquid culture to provide carbon to the microalgae. Due to the low solubility of carbon dioxide, to achieve good mass transfer a carbon dioxide rich gas is bubble through the media. This process is buoyancy driven which is dependent on the presence of gravity [9]. Without gravity there is limited phase separation following phase contact in traditional photobioreactors representing a major hurtle to this technology's application extra-terrestrially.

When microalgae is grown outdoors, sunlight provides the necessary energy for growth. However, in order to facilitate growth during the night, or in indoor facilities, artificial lighting is necessary. Lighting costs, including fixed capital and utilities, represents major cost centres in the production of microalgae industrially. Employing artificial lighting may increase production costs as much as $25 per kg of biomass [17]. As such its viability is limited to high value products or applications where sterility is paramount. Though lighting is the driving factor for biomass productivity, nutrient supply must also be carefully considered to control the algae production cost and biomass quality. Media optimization with varying feedstocks and nutrients is essential for process economies. Other major fixed costs include the bioreactors, method of agitation, and CO2 source. Photobioreactors can range from lower cost open air pond systems to substantially more expensive sanitary closed system designs depending on the biomass end use. With the latter being substantially more expensive based off current practices. The theoretical cost of biofuels produced in open pond systems is $8.52 as compared to $18.10 per gal of biodiesel [18]. CO2 can be supplied at low cost using air, however, to increase productivity supplemental CO2 can be provided. With this would be the associated cost of the CO2 infrastructure which can account for up to 8% of the biomass production costs [16].

Figure 1.3: Air lift photobioreactor [19]

In recent years there has been considerable interest in making algae cultivation less water intensive as the downstream processing of algal biomass suspensions represents a significant cost to algae production. Dewatering the biomass during harvesting can account for 20-30% of the total production cost of algae [20], representing a significant area for potential cost savings. This demonstrates the applicability of low water systems not only in extraterrestrial uses, but also domestically. Proposed ideas include growing algae in biofilm which allows easier separation of the growth media and algal films which can then be harvested through scraping [21]. Zeng et al. proposed using a thermoresponsive hydrogel to release the algae product upon a temperature shift allowing for a concentrated solution to be made from the immobilized algae [22]. There have also been attempts to grow algae on the surface between a solid air boundary where water and nutrients are

supplied through the porous substrate [23] . Additionally, membrane-based bioreactors have also been proposed to separate media and algal suspensions[24].

1.2 Research Objectives

The objective of this thesis is to try a novel approach to food cultivation in space in order to overcome the challenges previously outlined. As shown, BLSS are complex systems comprising many interdependent processes, the most important being food production and oxygen revitalization. Algae based system have promise with respect to meeting these objectives, however, current technologies lack the mass efficiency, low resource requirement, and reliability required for extraterrestrial use.

1. Design and build a proof-of-concept system.

In conjunction with the Canadian Space Agency's Deep Space Food Challenge, the first objective of this project is to design a hydrogel based photobioreactor to grow algae in space. With our design we hope to meet the challenges previously outlined with existing photobioreactor systems with respect to gravity dependence, water utilization, and productivity.

2. Quantify performance of new system

Once a working setup has been developed, the performance of the system can be validated and compared to existing technologies. The performance of the system can be compared with respect to productivity, resource utilization, and quality of the final food product.

3. Develop an unsteady state continuum model for transport through hydrogel.

With developing the proof-of concept system there is a need to model the transport of inputs through the system to inform further design iterations. To do this a continuum model of the hydrogel transport phenomena will be explored to understand how gel dehydration will impact the reactor design. The transport of water through hydrogel is a complex process. Firstly, hydrogels tend to shrink as the water content decreases [25]. This

represents a moving boundary layer problem which required special consideration with respect to developing the model [26]. Secondly, it has been established that permeability within the hydrogel depend on the gel's water content further complicating a dynamic model of the system [27]. There has been considerable research into modelling hydrogel swelling, however, there still lacks a generally accepted explanation of the theory with wide applicability. Instead, several semi-empirical models have been proposed.

4. Incorporate growth kinetics and continuum model to develop a unit model for the bioreactor

With quantifying the algal growth kinetics, the algae growth on the gel boundary can be incorporated into the continuum model. This will give insight into how algae growth will impact hydration and nutrient diffusion through the system.

The ultimate goal of this work is to dynamically model the bioreactor so that simulation can be used to identify failure modes and to understand how the bioreactor can operate in the context of life support system. Further work will allow a unit model to be proposed which can then be integrated into a process model for a closed environmental system., as well as allowing for process intensification and scaleup.

Organisation of This Work

This work is organised into two parts. Part I of this work will be focused on the design and characterization of the bioreactor system that has been designed as part of the CSA design competition. This includes the design iteration process as well as the experimental work conducted in order to quantify the reactor design's performance. This will span Chapters 2, 3 and 4 and will cover objectives 1-2. It will be seen in this part that there are challenges in the bioreactor with respect to mass transport presenting opportunities for improving the system's design. Part II of this thesis will explore the transport phenomena of water in hydrogels to gain insights into the bioreactors operation. Chapters 5, 6, and 7 will cover objective 3. In the conclusion (Chapter 8) the two aspects of this project will be connected to address the final objective.

Part I

Bioreactor Design & Characterization

Chapter 2

Background: Bioreactors

2.1 Why Microalgae?

There are two major considerations to in situ food production. The first is the resource requirements for growth. Autotrophic organisms can convert energy such as light into stored energy in the form of complex organic compounds like carbohydrates, fats, and proteins using simple carbon compounds like carbon dioxide. On the other hand, heterotrophs rely on the metabolism of organic carbon compounds for energy [28]. The advantage of photoautotrophs, autotrophs that utilize photosynthesis, is that they do not require organic carbon to be supplied for metabolism. This will help lower the launch weight of in situ food systems. They can simply use the carbon dioxide produced by the crew as the carbon source for photosynthesis. The second consideration is the food system productivity relative to its footprint. High productivity is a key design consideration due to mass and volume constraints in space habitats. Microalgae satisfies both constraints as they are photoautotrophs and have a relatively high growth rate compared to that of higher order plants like grassy crops [29]. Additionally, the high growth rate, on the order of days, means a relatively short harvesting schedule as compared to higher order plants which can take months to mature. This reduces food system risk as it can take months to recover from crop failure, but only weeks for microalgae. This can help to reduce food insecurity in space activities; a key consideration when resupplies may take months to years to arrive.

2.2 Traditional Photobioreactors

Traditional photobioreactors (PBR) involve microalgae cultures suspended in liquid media. The media provides the required nutrients for growth, while inorganic carbon (CO_2) is usually provided through sparging air that has either been enriched or atmospheric carbon dioxide concentrations (0.04 %) [30]. Flue gas has been directly used before at concentrations as high as 10 % [31]. Dissolved CO_2 decreases pH through the formation of carbonic acid [32]. Low pH leads to inhibitory effects on growth setting a limit on allowable CO_2 concentrations [33]. Photosynthetic energy may come from sunlight, or artificial sources. Photobioreactors can be classified as either open or closed systems. Open systems such as raceway ponds utilize sunlight and atmospheric carbon dioxide helping them realize a low operating cost. However, these systems have low productivity due to suboptimal growth conditions, suffer from excessive evaporative losses, and contamination by other microorganisms [34]. Closed systems on the other hand, offer better control and optimization of growth conditions as light, inorganic carbon and media composition can readily be controlled. This allows higher cell densities to be achieve at the cost of more complex and expensive capital. Examples of closed systems include tubular PBR, plate PBR, and cylindrical tank PBR.

Figure 2.1: raceway bioreactor [35]

Illumination requirements presents additional complexity for PBR design and operation. For heterotrophic bioprocesses growth is typically limited by substrate uptake, which commonly occurs enzymatically. As such Michaelis-Menton type enzyme kinetics are commonly adapted to microbial growth. In Monod-type kinetics nutrient uptake is coupled with a growth yield that relates substrate consumption and biomass production and maintenance [31].

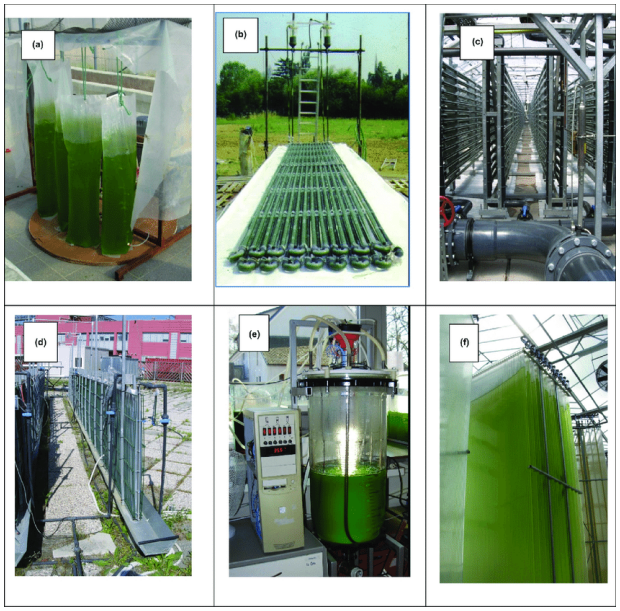

Figure 2.2: closed bioreactor [36]

$$r_S\ (c_S\ ) = r_{S,max}\frac{c_S}{c_S + k_S}$$
$$r_X\ (r_s) = y_{X,S}r_S - r_{X,m}$$

However, in phototrophic systems light is predominantly the limiting input. Unlike a substrate concentration, light is a flux. As such assuming enzymatic kinetics can be misleading, obscuring the physiological processes that determine growth. The first step in photosynthesis is light absorbance. This is a linear process dependent on the chlorophyll content in the chloroplast, which varies temporally in cell populations [31]. Light adsorption is related to the effective absorption cross section σ_X $[m^2 g^{-1}]$ of the biomass. At high irradiance, a limiting step in the metabolic pathway leads to a maximum specific growth rate $r_{X,max}$, which is dependent on the culture conditions. If irradiance is further increased, a decrease in growth rate can occur from light inhibition. From an economic perspective, artificial light often represents the largest operational expense, and thus is the ideal limiting input. By having the growth kinetics light limited wasted energy from inefficient light utilisation is avoided.

$$r_{hv,abs} = \sigma_X I_{hv}$$

$$r_X\left(r_{hv,abs}\right) = y_{X,hv} r_{hv,abs} = r_{X,m}$$

$$r_X \leq r_{X,,max}$$

The characteristic response of photosynthetic activity in microalgae to light intensity can be represented in a photosynthesis-irradiance (PI) curve, which is a piece-wise function capturing the different growth regimes associated with phototrophic microalgae [37]. The x-intercept represents the maintenance energy required to maintain the cell population. The slope of the linear increasing part of the curve is related to light absorbance, while the plateau is the maximum growth rate of the culture. Several models have been proposed to describe PI curve with varying sophistication.

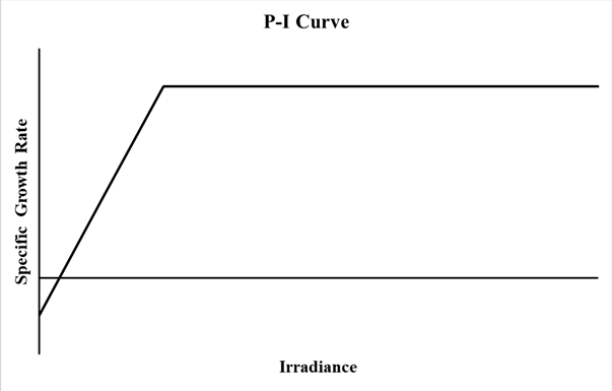

Figure 2.3: Simple PI Curve

2.2.1 Challenges in Photobioreactor Design

A multitude of complexities arise when applying kinetic models to photobioreactor design. These complexities make it challenging to design effective photobioreactors that are scalable and predictive. The three main considerations to microalgae growth are temporal, spatial and cellular variations within the photobioreactor. Temporally, photo-acclimation is the long-term adjustments of pigment content and cellular composition to variations in nutrient and lighting conditions. This process may happen on timescales ranging from hours to days, effecting the culture response to environmental conditions over time [38]. As the microalgae environment changes, the cells respond with physiological changes that impact the cellular makeup of the culture and the productivity of the system. This response can be exploited to tailor the resulting biomass composition. Spatial variations in

culture conditions drastically impact the growth rate in real systems. Uniform light distributions are challenging due to the attenuating effect of suspended microalgae. This creates spatial light gradients that impact the local growth rate. Shading within the reactor can significantly lower the realized growth kinetics in the overall system [31]. Finally, the cell population is variable in the reactor. Cellular composition is influenced by heterotrophic kinetics and nutrient variations within the medium. Locally depleted nutrients will affect growth rates as cellular processes other then photosynthesis may become limiting factors in growth [39].

$$r_{X,\ max,\ true}\left(I_{hv}\right) = \min\left(r_{X,Chl}\left(I_{hv}\right),\quad r_{X,env}\left(c_{comp}\right),\ r_{X,max,\ int}\right)$$

2.2.2 Light Gradients

When accounting for spatial variations in growth kinetics, in response to light attenuation, there are two possible approaches. The first method is light integration. Here the average intensity over the reactor volume is used to determine the growth rate. However, the localized effects of light inhibition and dark spots are not captured [40]. This meaning that the true growth rate in the total volume may be obscured. The other method is growth integrating. This method integrates the local growth rate over the reactor volume [41]. However, this requires detailed knowledge of light gradients within the bioreactor which may not be available due to the complexity of cell shading.

$$r_{X,av}\left(I_{hv,0}\right) = r_x\left(\frac{1}{D_R}\int_0^{D_R} I_{hv}\left(l_{path}\right) dl_{path}\right)$$

$$r_{X,av}\left(I_{hv,0}\right) = \frac{1}{D_R}\int_0^{D_R} r_X\left(I_{hv}\left(l_{path}\right)\right) dl_{path}$$

2.2.3 Maximum Growth Rate

The first step in photosynthesis is photon absorption, which is a linear process. The energy from the absorbed photon is then transferred to the electron transport train to synthesize ATP. This is a discrete process requiring a specific amount of energy. Excess energy of absorbed photons is dissipated as fluorescence or heat, a process known as non-photochemical quenching [42]. The time scale of this energy transfer, usually controlled by photosystem II (PSII), determines the overall photosynthesis rate as excited chlorophyll

molecules cannot be further excited by a second photon [43]. Due to the time scale of relaxation of the complex, there is a maximum flux of photons that the system can utilized before all photosynthetic units are saturated. Though lacking physical meaning [31], the photosynthetic process involving chlorophyll, PSII, PSI and carbon fixation in the cell can be broken down into discrete units called photosynthetic units (PSUs) [44]. These units can be either reactive or active depending on if it has absorbed a photon or not. Accounting for photon absorption, and the relaxation time of PSII, the number of available PSUs for additional irradiance can be modelled through the following system of equations:

$$\frac{dn_{reactive}}{dt} = -\sigma_X I_{hv} \frac{n_{reactivce}}{n} + \frac{n_{excited}}{\tau} = 0$$

$$\frac{dn_{reactive}}{dt} = \sigma_X I_{hv} \frac{n_{reactivce}}{n} - \frac{n_{excited}}{\tau} = 0$$

$$n_{reactive} + n_{excited} = n$$

Given that the time scale of biomass growth is orders of magnitude greater than the relaxation time of the PSU, the PSU model can be assumed to be at steady state $\frac{dn}{dt} = 0$. As such the specific transport rate $r_{hv.act}$ $[mol\ g^{-1}s^{-1}]$ of excited photon energy is equal to:

$$r_{hv,act} = \frac{n_{excited}}{\tau}$$
$$r_{hv,act} = \frac{\sigma_X I_{hv} n}{\sigma_X I_{hv} \tau + n}$$
$$r_{hv,act} = \frac{n}{\tau} \frac{I_{hv}}{I_{hv} + \frac{n}{\sigma_X \tau}}$$

Grouping parameters leads to the following rational expression, comparable to Michaelis-Menton kinetics. However, this new expression has parameters directly related to physiological mechanisms associated with the photosynthetic pathway. The maximum transport rate corresponds to all PSU's being in the excited state ($r_{hv,act,max} = n/\tau$), and the light limitation constant (k_I) is equal to $\left(\frac{n}{\sigma_X \tau}\right)$.

$$r_{hv,act} = r_{hv,act,max} \frac{I_{hv}}{I_{hv} + k_I}$$

Finally, the biomass growth rate can be determined as:

$$r_X\left(I_{hv}\right) = y_{X,hv}\ r_{hv,act,max}\frac{I_{hv}}{I_{hv}+k_I} - r_{X,m}$$

At high irradiance, there can be a decrease in specific growth due to light inhibition. This should be avoided in practice due to diminished energy efficiencies. When accounting for light inhibition, the PSU model previously described can be modified by including a third inhibited state as described by the Eilers-Peeters (photosynthetic factory, PSF) model [45]. PSUs in the reactive state can be damaged if hit by an additional photon leading to the inhibited state. This prevents it from passing an electron to the dark stage of photosynthesis, and therefore unable to contribute to energy production in the cell. Inhibited PSUs can recover to the active state. Formulating the model with respect to kinetic constants, the absorption of light, in both excitation (α) and inhibition (β), is assumed to be first order with respect to irradiance. The energy transfer from both the exited (γ) and inhibited states (δ) are assumed to follow zeroth order kinetics [46]. Energy for growth is solely associated with the energy transfer from the excited complex (x_2), as such the model may be formulated as the following system of equation. It is worth noting that both PSU based models are limited to growth phase kinetics and as such do not consider the production of secondary metabolites.

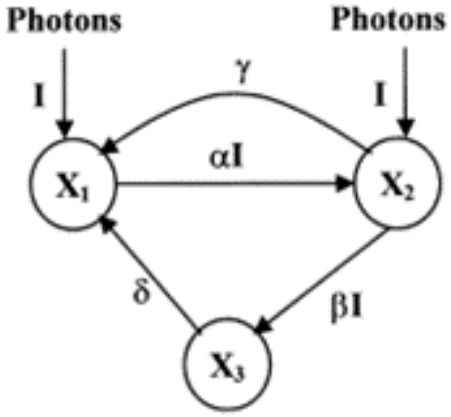

Figure 2.4: Eilers-Peeters Model [45]

$$\frac{dx_r}{dt} = -\alpha I_{hv} x_r + \gamma x_e + \delta x_i$$

$$\frac{dx_2}{dt} = \alpha I_{hv} x_r - \gamma x_e - \beta I_{hv} x_e$$

$$\frac{dx_3}{dt} = \beta I_{hv} x_e - \delta x_i$$

$$x_r + x_e + x_i = 1$$

$$r_X\left(I_{hv}\right) = y_{X,hv}\gamma x_e - r_{X,m}$$

The number of PSUs in the inhibited state can be determined experimentally through fluorescence. The ratio of variable fluorescence (F_v) to the maximum fluorescence (F_m) is linearly related to the activity of PSII, and therefore correlates to PSU inhibition. $(F_v/F_m)_{max}$ has been shown to be 0.6 for several blue-green algae. f is a proportionality coefficient [45].

$$\frac{F_v/F_m}{(F_v/F_m)_{max}} = f\left(1 - x_3\right)$$

Letting $(F_v/F_m)_{max}$ $f = f'$:

$$\frac{F_v}{F_m} = f\left(1 - x_3\right) = f\prime(x_1 + x_2)$$

f' is an additional parameter that can be solved for.

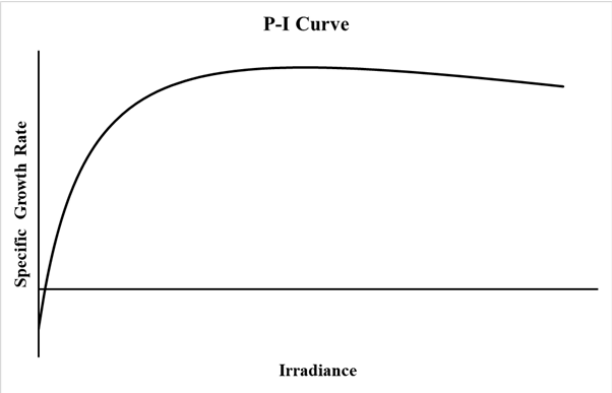

Figure 2.5: PI curve based off Eilers-Peeters Model

As can be seen the PI curve, the initial response to growth rate to an increase in irradiance is linear, corresponding to the linear process of light absorption as previously mentioned. As irradiance increases, the effect of light inhibition becomes more pronounce ultimately leading to a decrease in specific growth rate at high values.

2.2.4 Carbon Dioxide Supply Considerations

The control of inorganic carbon is important to optimize biomass production. The culture should ideally not be carbon-limited, however the loss of CO2 in the off-gas can represent a system inefficiency. The typical carbon content of microalgae is 0.5 g/g [47]. The inorganic carbon demand of algae is dependent on the cell's composition. The carbon dioxide transfer rate required for the formation of starch is $Y_{CO_2/X} = 1.6\ g\ g^{-1}$, while that for lipids it is $Y_{CO_2/X} = 3.1\ g\ g^{-1}$. However, a typical CO2 to biomass efficiency is $Y_{CO_2/X} = 1.8\ g\ g^{-1}$ [31].

In a liquid culture, the dissolved CO2 concentration in the media must be high enough to meet the CO2 consumption rate of the algae while also considering the uptake mechanism for CO2 into the cell, which can be described through an Michaelis-Menten type kinetic with a half-saturation constant of $k_{co2} = 0.486mg\ L^{-1}$ [31]. The main carbon fixation enzyme is ribulose-1,5-biphophate carboxylase/oxygenase (RuBisCo). This enzyme forms the main bottleneck in carbon fixation. This enzyme has a half-saturation constant of 740-1120 ppm, and a maximum turnover rate of 4 s^{-1} [48]. This enzyme has high expression in cells and may constitute 1.4-3.7% of the whole cell's protein content [49]. A factor that influences the fixation of carbon dioxide by RuBisCo is the competitive binding of oxygen to the enzyme in a process called photorespiration. Physiologically this process is thought to help suppress the oxygen radicals generated in the chloroplasts limiting oxidative stress. However, this negatively impacts the efficiency of ATP production and CO2 fixation in the cell [50]. As such, limiting the partial pressure of oxygen can improve CO2 uptake by the culture. Oxygen inhabitation typically occurs when partial pressure of oxygen is above 40% [31]. The partial pressure of CO2 in the gas phase must be sufficiently high to achieve sufficient mass flux across the gas-liquid interface to meet the cells carbon requirements. This can be modelled using a two-resistance model for convective mass transfer between phases. Using the liquid film convective mass-transfer coefficient, the rate of carbon dioxide consumption in the media can be related through the following expression [51].

$$r_{CO2}c_x = k_L a\ \left(c^*_{CO2,\ gas} - c_{CO2,liquid}\right)$$

Typically, the CO2 partial pressure is often controlled via media pH to avoid the unreliability of online P_{CO2} measurements [31]. This method suffers from inaccuracies however, due to the pH change associated with ammonia or nitrate uptake by the cells during growth. The flashing light effect is the phenomenon in microalgae cultivation where light/dark cycles enhance the photosynthetic efficiency of the cells. Algae when grown in saturating photon flux densities suffer from low photosynthetic efficiencies. This is thought to be due to the ability for cells to store excitation energy for short time scales (ms). Dark cycles are thought to enhance dark reactions' rates. Dark reactions include the transfer of electrons between photosystem II and photosystem I [31]. This is because under continuous illumination, oxygenic photosynthesis is limited by the rate of electron transfer which is around 10 times slower than the rate of light capture by chlorophyll [52]. It is proposed that under high light flashing frequencies, the amount of ATP generated in the electron transfer chain is enough to support the much slower Calvin cycle during the dark cycle.

2.2.5 Nutrient Control

Media design is an important consideration in photobioreactor design, as nutrients play a critical role in biomass production. The most essential of which are the nitrogen and phosphate sources [31]. Under ideal conditions, nutrient concentrations should be high enough to prevent kinetic limitation, such that the growth rate results from other limiting conditions such as light. Nitrogen and phosphate containing salts represent a significant operating expense which must be carefully considered in order to balance algal productivity with the cost of production. Dosing strategies should aim to limit the amount of nutrients used to improve process economics. Potential nitrogen sources include nitrate, ammonia and urea each with their own respective benefits and limitations including cost and toxicity in high concentrations [53]. In wastewater applications, and in natural habitats, microalgae often grow under nutrient deficient conditions rather than light limiting, impacting the kinetic modelling used in these processes. Typically, Monod-type kinetics for the limiting nutrient is used [54].

$$\mu = \mu_{max} \frac{[S]}{K_s + [S]}$$

In wastewater applications, there are complex conditions involving multiple nitrogen and phosphate sources. Due to this stoichiometry, it is difficult to determining the limiting ion species and to predict the effect of varying media conditions. The uptake mechanisms for

different nutrient types will impact availability within the cell [55]. Additionally, the ability of microalgae to store nitrogen and phosphate hinders the ability to precisely predict kinetics solely off the nutrient profile, as the effects of nutrient limitation will be delayed from the drop in media concentrations. This requires the culture history to be tracked. However, this ability of microalgae to efficiently take up, and store, nutrients can allow for more sophisticated dosing strategies such as providing nutrients in short peaks. The microalgae will take up the nutrients immediately and use it over time leaving low concentrations in the media. This can help to reduce the bacterial contamination in the culture [31].

The media stoichiometry can greatly influence the macromolecular composition of the microalgae. Like acclimation, which is the temporal response of the cells to a change in lighting conditions, adaptation is the temporal response of microalgae to the nutrient conditions and can greatly influence its macromolecular composition [31]. There is a complex interplay between macromolecular composition, light and nutrient uptake within the cell. For example, the chlorophyll content effects absorbance, and light gradients within the bioreactor and therefore reactor kinetics [56]. However, the protein content of the cell is also influenced by the stoichiometry between chlorophyll molecules and proteins in the light harvesting antenna. The principal reason for stoichiometric variability in microalgae is the use and storage of compounds within the cell. Nitrogen limitation can be employed to reduce anabolic activity in the cell leading to the accumulation of lipids and carbohydrates, and therefore decreasing the relative protein content [57]. Lipid contents as high as 70% have been reported in high salinity and nitrogen depleted media [58]. Similarly, phosphate depletion reduces biomass yields as well as induces the production of lipids [59]. It is worth noting that nutrient starvation can lead to excessive oxidative stress, which can be detrimental to cellular health and productivity [60]. Additionally high accumulation levels can reduce photosynthetic efficiency. In outdoor cultivation systems, starch is accumulated during the day, which is then consumed during the night to support the creation of more biomass, rather than for respiration.

2.3 Alternative Bioreactor Designs

Open pond systems are the most widely adopted cultivation method due to their low capital cost. However, their productivity remains low with an aerial productivity for *C. vulgaris* in the range of 3.4 to $11.2\,g\ m^{-2}d^{-1}$ [61]. The low cell densities in the system make dewatering the biomass a challenge and these open systems suffer from evaporative loss

and contamination problems. Dewatering steps can account for up to 10.7% of biomass cost or \$53/ton of the minimum biomass selling price of \$491/ton determined by NREL for open pond systems [62]. In contrast, enclosed photobioreactors (PBR) are protected from contaminants and reduce water usage, but pose different challenges related to oxygen degassing which can inhibit carbon fixation and high capital and operational costs [63, 64].

To overcome the difficulties posed by open pond cultivation and similar suspended PBRs, there has been considerable research into improved technologies and alternative cultivation methodologies. One area that has shown promise is in solid-state cultivation techniques. In these biofilm PBRs, the microalgae cells grow as a dense paste or film on the surface of a material instead of being suspended in liquid. By keeping the media and biomass separate, substantially less water is required for biomass production and higher productivities based on device footprint can be achieved, up to 30 $g\ m^{-2}d^{-1}$ [65]. These devices are further divided into either fully submerged, intermittently submerged, and non-submerged designs based on how they received the nutrients and water needed to support growth [65]. Examples of these types of reactors are shown in Figure 2.6. Submerged designs have been primarily applied to wastewater treatment scenarios using naturally formed algae biofilms [66, 67, 68, 69]. In such systems the algae form a biofilm attached to a surface and remain submerged in media. On the other hand, intermittently submerged systems have the algae attached to a surface that moves in and out of media continuously. This allows for greater growing area for cultivation and is commonly designed as a partially submerged drum or belt that rotates [70]. An example of non-submerged systems are twin-layer porous substrate reactors, which are composed of a glass plate sandwiched by filter papers have been used for the xenic cultivation of *Scenedesmus sp.* [71, 72, 23, 73], *C. vulgaris* [74], and even *H. pluvialis* for astaxanthin production [75, 76, 68]. Very high cell density of the biofilm paste also simplifies harvesting and could potentially eliminate the dewatering step required for most downstream applications.

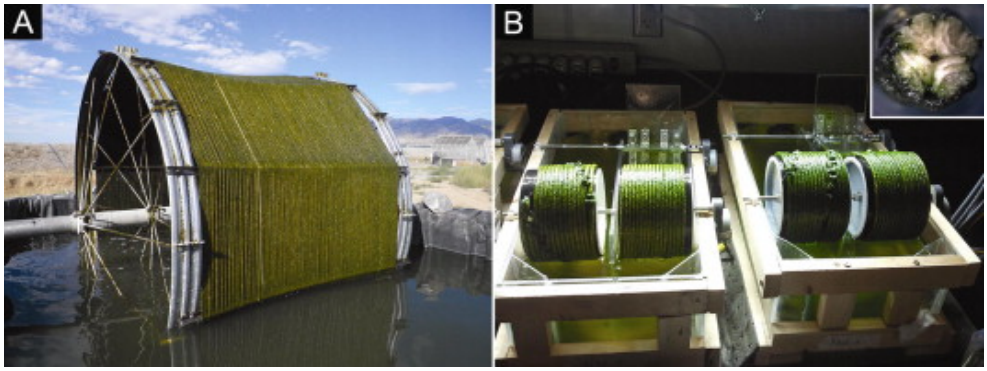

(a)

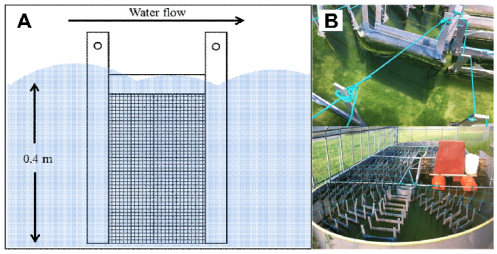

(b)

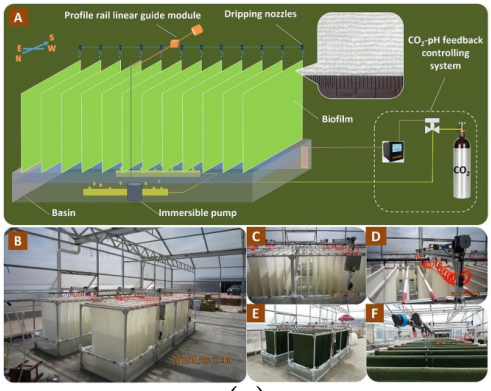

(c)

Figure 2.6: Solid state cultivation designs: **(a)** intermittently submerged [70], **(b)** fully submerge [77], **(c)** non-submerged PBRs [67]

Over the last decade, various design elements of non-submerged solid-state PBRs have been studied, including the type of solid support used for microalgae growth. The majority of the designs incorporate highly permeable porous materials such as cellulose-based filter paper [23], polyester nylon blends [67], and other substrates [66, 78]. In many cases, these are directly placed on a glass panel for mechanical support and the nutrient solution is trickled from the top of the vertical module over the algae film, but in some cases, sponges can be placed in between the glass and filter paper as these designs can easily result in dry spots [74]. Such systems have demonstrated lower water usage in closed operation [79, 80], and improved area growth rates compared to suspended cultures [23]. The first large-scale attached cultivation trial outperformed open pond systems in productivity [67]. However, this system was considerably more expensive than an open pond and while the total water

consumption was lower, it still suffered from excessive evaporative losses when operated in an open system as compared to open pond systems [67, 80].

To address some of the challenges described here, in Chapter 3 a new solid-state cultivation system is presented. This system avoids the formation of dry areas by way of a hydrogel substrate that is continuously supplied with water and nutrients. This constitutes a closed system where the media is completely separated from the algae growth surface allowing for better operational control and contamination prevention. To the best of our knowledge, no previous work has attempted to supply water and nutrients for attached algae growth through a hydrogel from a replenishable liquid media reservoir. By doing so we aim to reduce further the water demand of algae cultivation compared to other attached cultivation designs. Additionally, by achieving complete phase separation our design will be gravity independent allowing for potential applications for life support in extraterrestrial environments.

Chapter 3

Methods: Experimental

3.1 Photobioreactors

Two hydrogel photobioreactors (hPBRs) were designed to cultivate microalgae. Design A was the microgravity prototype for the CSA design competition, while Design B offered better control over operating conditions. Design B was used to test bioreactor kinetics and investigate biomass quality.

Design A

This bench scale prototype was used to demonstrate the feasibility of the hPBR design principles. This design consisted of two hydrogel modules placed on either side of a spacer. This allowed media circulation within the device. Each hydrogel was held between two aluminium frames and had a stainless steel mesh embedded in the gel to maintain its structure. The frame components were cut using a CNC from 1/8" (11 GA) aluminium. The spacer was made from a 9mm acrylic sheet. Neoprene gaskets (1/8") created a watertight seal between the framed hydrogels and the spacer. stainless steel nuts and screws held the assembly together. Having gels on both sides of the module allowed for greater cultivation space. The hydrogel sheets were 6 cm x 14 cm bring the total available growing surface for each module to 168 cm^2. The modules were then placed in a humidified enclosure in a rack system with alternating LED light panels. This allowed for a modular design. A peristaltic pump was used to circulate media to the modules. Humidity was controlled through bubbling air through flasks containing water. In the prototype system

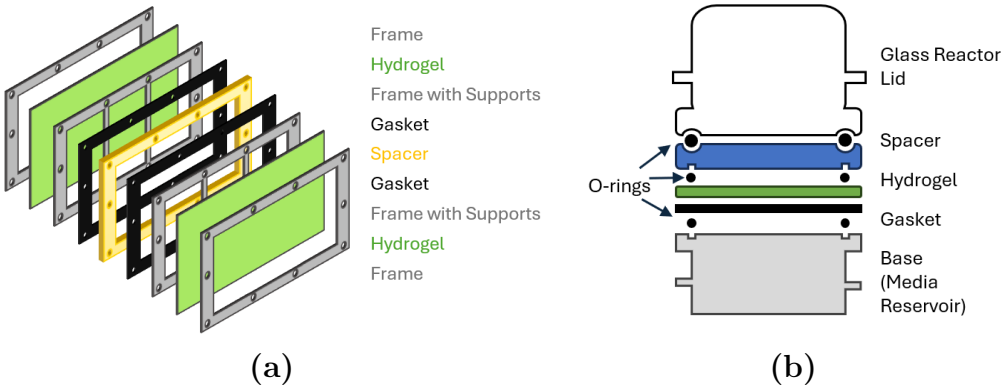

Figure 3.1: Hydrogel Reactor Designs: **(a)** Design A **(b)** Design B

two modules were installed with 3 light panels. Each light panel consisted of 4 rows of 5050 SMD LED Plant Strip Lights (AveyLum, China) producing an output of 2,400 lux.

Design B

To explore the growth kinetics, smaller bioreactors were designed to better control environmental conditions. Eight reactors were fabricated for the growth study. Glass flanges (CG-138 Chemglass) were modified such that the pipe ends were closed and side ports added to act as the upper half of the new reactors. Next, bases were 3D printed out of ABS or resin to serve as the media reservoir. Inlet and outlet tubing connectors were added to the media reservoirs to allow fresh media circulation. The 3D printed parts were sealed with silicone to make them watertight. Spacer rings to hold the hydrogels in place, and to fit O-ring (#-153) seals, were 3D printed from PLA. Neoprene gaskets (1/8") were used to form a seal between the hydrogel and ABS base. The glass compartment was sealed against the spacer with a GC-305 O-ring. The reactors were held together by clamps (made from 2mm aluminium) around the flanged surfaces of the media reservoir and glass sections. Two 2550 Im LED light arrays (SBLED24 Sunblaster, Canada) were used as the lighting source (30,400 lux at the gel surface). The available growing area of the hydrogel sheet is 22.9 cm^2. The bioreactors were cultured upside down with the light source below them to ensure the hydrogel remained in contact with the nutrient solution. The inlet air was humidified by bubbling it through water.

Hydrogel

An in depth discussion of hydrogel properties is presented in Chapter 5. As Design A was used for the CSA design competition, one hydrogel material was explored to demonstrate design feasibility. For Design A, hydrogel sheets were prepared from a 15% polyvinyl alcohol solution (87-90% hydrolysed, average mol wt. 30,000-70,000, Sigma-Aldrich, USA) that was subject to 5 freeze/thaw cycles. Prior to freezing a stainless-steel mesh was inserted into the middle of the PVA solution. The hydrogels were cast in place between the metal frames with an additional plate across the face of the frame to form the mold. The design rationale behind the process presented here will be expanded upon in Chapter 4.

Design B was used to quantify hPBR performance and act as a platform to study solid-state algae growth. Three hydrogel materials were explored for this design. These were physically crosslinked PVA (pPVA), chemically crosslinked PVA (cPVA) and bacterial cellulose (BC). These materials were investigated as they are shown to be nontoxic and food contact safe [81]. Additionally, algae growth on these materials have previously been demonstrated [82]. The pPVA gels followed the same procedure in Design A, however without the mesh. The gel size needed for this reactor was 100mm in diameter. As such, these gels were cast in 100mm petri dishes (VWR, USA) using 20mL of the 15% polyvinyl alcohol solution. The cPVA gels were prepared following a procedure previously outlined [83]. In summary, a 10% PVA solution, 15 w/v% sodium trimetaphosphate, STMP, (Sigma-Aldrich, USA) solution, and 30 w/v% sodium hydroxide (Sigma-Aldrich, USA) solution were mixed in a ratio of 12:1:0.4 to form the crosslinking solution. This solution was first centrifuged then poured into 100mm petri dishes. The hydrogels were placed in a humidity controlled enclosure to cross-link and dry for 4 days. Following this, the hydrogels were removed from the petri dishes by submerging them in water. The de-molded gels were placed in DI to equilibrium before use. The BC gels were sourced from Rojas Research Group (Vancouver, Canada) [84]. These materials were evaluated based of several selection criteria including mechanical strength, easy of synthesis, and transport properties. As nutrients and water will be transported through the hydrogel in this design it is essential to understand how the material perform in this respect.

Water Flux Comparison

To estimate the water availability to the microalgae, the water flux through the different hydrogel materials was measured using a flux cell. The different hydrogel materials were

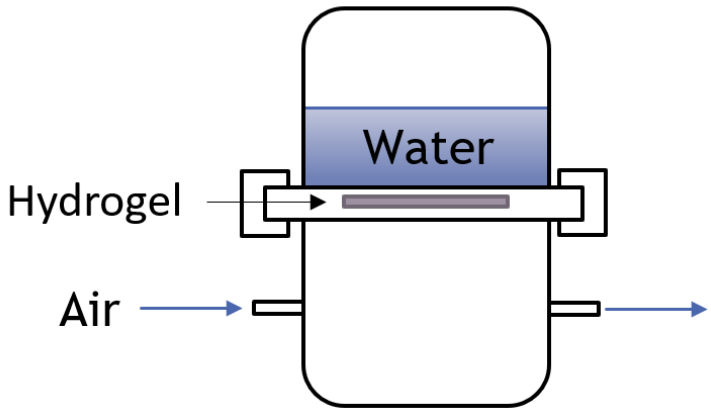

Figure 3.2: Flux Cell

placed in the diffusion cell with a specified volume of water on an analytical balance. As air passed over the exposed gel surface, water will be convected away. As such, the mass of the cell will decrease allowing the steady-state flux through the material to be measured. By testing each material under similar conditions, the transport properties of the different hydrogels can be compared.

3.2 Microalgae strain and Growth Media

Strain

Chlorella vulgaris UTEX 395 was obtained from The University of Texas at Austin culture collection of algae (UTEX, United States). Axenic cultures were maintained in the TAP media and subcultured as needed.

TAP Media

The inoculum was grown in TAP media [85]. 1L of media contains 2.42g tris, 25mL of Tap Salts, 1mL of glacial acetic acid, 375 μL of phosphates solution, and 1 mL of Hunter's Trace Elements. Details on making these solutions are provided in Table 3.1.

Solution	Compound	$g\ L^{-1}$	Compound	$g\ L^{-1}$	Compound	$g\ L^{-1}$
TAP Salts	NH_4Cl	15	$MgSO_4 \cdot 7H_2O$	4	$CaCl_2 \cdot 2H_2O$	2
Phosphates	KH_2PO_4	28.8	$K_2H_2PO_4$	14.4		
Hunter	EDTA	50	$ZnSO_4 \cdot 7H_2O$	22	H_3BO_3	11.4
	$MnCl_2 \cdot 4H_2O$	5.08	$CuSO_4 \cdot 5H_2O$	1.56	$FeSO_4 \cdot 7H_2O$	4.988
	KOH	17				

Table 3.1: TAP Media Recipe

Bold's Basel Media

BBM was the preferred growth media in the bioreactors, as this is a carbon free media [86]. The media is made following the recipe outlined in the following tables and making up the media volume to 1L.

Stock Solution	1	2	3	4	5
mL per L	10	10	10	10	10
Stock Solution	6	7	8	9	10
mL per L	10	1	1	1	2

Table 3.2: BBM Recipe

Stock	Compound	$g\ L^{-1}$	Stock	Compound	$g\ L^{-1}$
1	$NaNO_3$	25	2	$CaCl_2 \cdot 2H_2O$	2.5
3	$MgSO_4 \cdot 7H_2O$	7.5	4	K_2HPO_4	7.5
5	KH_2PO_4	17.5	6	$NaCl$	2.5
7	$EDTA$ & KOH	50 & 31	8	$FeSO_4 \cdot 7H_2O$ acidified	4.98
9	H_3BO_3	11.42	10	Trace	Table 3.4

Table 3.3: BBM solutions

Compound	$g\ L^{-1}$	Compound	$g\ L^{-1}$	Compound	$g\ L^{-1}$
$ZnSO_4 \cdot 7H_2O$	8.82	$MnCl_2 \cdot 4H_2O$	1.44	MoO_3	0.71
$CuSO_4 \cdot 5H_2O$	1.57	$CoNO_3 \cdot 6H_2O$	0.49		

Table 3.4: Trace Salt Solution Composition

3.3 Bioreactor Operation

Inoculation Procedure

The inoculum was prepared by adding 10% v/v maintenance culture to fresh TAP media and incubating at 25°C for 3 days at 150 rpm with 150 $\mu mol\ m^{-2}s^{-1}$ of photosynthetically active radiation (PAR) (Innova S44i, Eppendorf). To inoculate the hPBRs, 15 mL aliquots were centrifuged (at 3250 x g for 10 min, 5810R, Eppendorf Germany) and resuspended in 10 mL of DI to remove residual TAP media. Cells were centrifuged again and resuspended in 0.5 mL of DI water, applied evenly to the surface of the hydrogels, and incubated at RT for 5 min. After 5 minutes the excess inoculum was allowed to drip off the gel surface.

Harvesting Protocol

At the specified harvesting interval, the algae was scraped off the hydrogel surface using a spatula and collected in 1.5 mL centrifuge tubes. Some sample loss occurred during the scraping process that would be more significant at lower biomass densities. This was suspended in 1 mL DI water, and centrifuged (at 20,000g for 2 min Sirvell Legends Micro 21, Thermo Scientific). The supernatant was stored at $4°C$, and cell pellets frozen at $-80°C$ until further analysis.

3.4 Bioreactor Performance

3.4.1 Growth Kinetics

Using eight Design B reactors, the growth rate of algae in the system was measured. On day 0, all reactors were inoculated as previously described. In duplicates, the biomass was allowed to grow for between 3 and 24 days before harvesting using the previously

described procedure. The cell pellets were freeze-dried for 24 hours (FreeZone 2.5 plus Labconco, USA) and weighed to determined dry cell weight (DCW $g\ m^{-2}$). From this the area productivity was calculated.

Cell growth is typically reported volumetrically. However, solid-state cultivation systems have area productivity and hard to compare to traditional suspended systems. As specific growth rate is in terms of existing biomass it can be determined irrespective of the cultivation method and thus can be a basis of comparison.

3.4.2 Algae Nutrient Supply

As the algae is not grown in suspended, the supply of nutrients and water are dependent on the hydrogel's transport properties. The algae paste adjacent to the hydrogel contains the nutrients directly available to the algae which may be different to the quantities found in the media reservoir. Therefore, to measure the nutrients available for growth the biomass is suspended in DI water and centrifuged. The resulting supernatant is analysed for nitrate and phosphate content.

Phosphate Analysis

The phosphate content was determined through an ascorbic acid assay based off the US EPA Method (Method 365.3) [87]. Ammonium molybdate (Ward's Science, USA) reacts with phosphate(V) ions to produce a coloured complex. Excess ascorbic acid (Sigma Aldrich, USA) is used to prevent the oxidation of the complex along with sulfuric acid(Sigma Aldrich, USA) . Using a spectrophotometer, the phosphate concentration can be correlated to colour, allowing the phosphate content of the original sample to be determined. Samples were diluted to between 2.5 and 15 $mg\ L^{-1}$, and absorption was measured at 650 nm (Synergy 4, Biotek Instruments, USA). A calibration curve was made for concentration between 1-30 mg of phosphate.

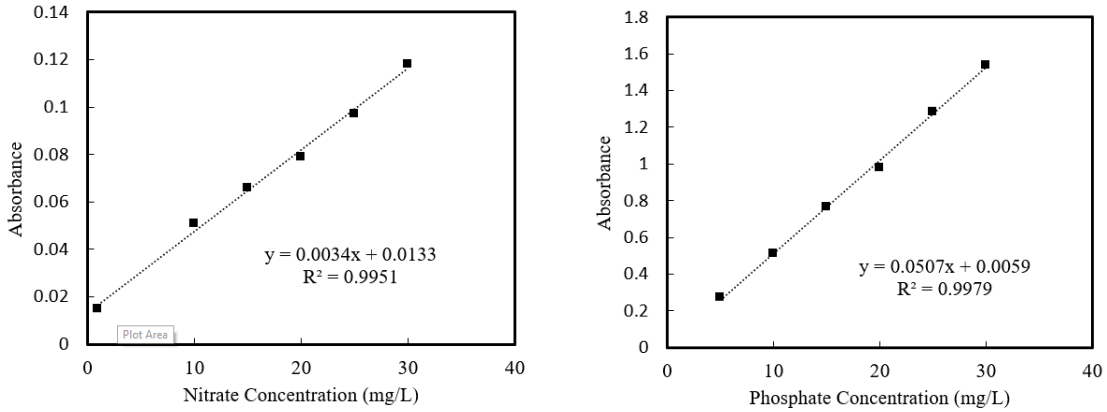

(a) **(b)**

Figure 3.3: Nutrient Assay Standard Curve **(a)** Nitrate **(b)** Phosphate

Nitrate Analysis

Nitrate content was determined using NitraVer® 5 reagent (Hach GmbH, Germany), which is compliant with US EPA standards. This is a cadmium reduction method using nitrite colorimetry to determine concentration. Samples were diluted to between 0.3–30 $mg\ L^{-1}$, and absorption was measured at 500 nm. From this the original nitrate concentration of the sample can be determined. A standard curve was made using known concentrations between 1-30 $mg\ L^{-1}$ of Sodium Nitrate.

3.4.3 Surface Coverage Analysis

To assess the performance of the reactor it is important to understand how efficiently the growing surface is utilized. As the coverage initially will be irregular and nonuniform, direct surface coverage measurements are impractical. As such, it was investigated using OpenCV at various growth time points. It is expected that the surface coverage will increase as the algae grow. The surface ideally will be fully covered in a few days. If poor coverage is observed, it may be an indicator that the inoculating procedure needs to be improve or an issue with the bioreactor design.

Using Reactor B, pictures without the glass compartment were taken against a black background at different time points. These images were analyze using OpenCV [88]. This

analysis aimed to quantify algae coverage by comparing the number of green pixels to the total number of pixels that make up the hydrogel surface. First these images were gray-scaled and the edges detected using a Canny edge detection algorithm. The resulting edges were first dilated to enhance features, and then eroded to remove noise from the image. Contours were extracted from the image and sorted by enclosed area. The contour corresponding to the gel boundary was then manually selected and drawn on a black background. To ensure the contour formed a closed shape the Douglas-Peucker algorithm was used to approximate a closed shape. The selected contour mask was then applied to the original image to separate the hydrogel from the background. This image was then converted from BGR to HSV colour coding. HSV coding represents colours in cylindrical coordinates as compared to the Cartesian BGR representation. By transforming colours into hue (H), saturation (S) and value (V) components, thresholds become easier as HSV is perceptually more intuitive then BRG coding as the hue is continuous. Using an upper and lower colour thresholds for light ([20,100,0] to [80,255,255]) and dark ([40,10,0] to [75,255,200]) green the green parts of this image were extracted. The percent coverage was determined by dividing the pixel area of the final image from the pixel area the contour captured.

3.4.4 Pigment Analysis

Chlorophyll content was analysed following US EPA Method 446 [89]. Procedure required mixing 0.05 g of freeze-dried sample with 1.5 mL of acetone solution (10:1 Acetone:water) in a 1.5 mL centrifuge tube. The tube was resealed immediately to prevent solvent loss [90]. Samples were refrigerated for 3 hours with vortex mixing every 30 minutes. Following the extraction period, samples were centrifuged at 20,000g for 2 min and the supernatant analyzed. Absorbance was measured at the following wavelengths: 750, 664, 647, 630 nm,

$$C_a = 11.85Abs_{664} - 1.54Abs_{647} - 0.8Abs_{630}$$

$$C_b = 21.03Abs_{647} - 5.34Abs_{664} - 2.66Abs_{630}$$

3.4.5 FAME (Fatty Acid Methyl Esters) Analysis

Lipids are present in many forms within microalgae which can be analysed using FAME analysis [91]. This method uses biomass transesterification to determine the fatty acid

profile within the biomass. To 10 mg of dried biomass 25 μL of methyl nonadecanoate (C19:0Me) recovery standard was added followed by 200 μL of chloroform:methanol (2:1), and 300 μL of 0.6M HCl:methanol. Samples were heated for 1 hour at $85°C$. 1 mL HPLC grade hexane was added to each sample and mixed. After letting the samples sit for 1-4 hours to allow phase separation, the hexane phase was transferred to a a new 1.5mL GC vail, diluting 450 μL of extract with 50 μL of methyl heptadecanoate (C17:0Me) internal standard. Samples were then stored at $-20°C$ until GC analysis. Then samples were measured using a Flame Ionization Detector (FID) and compared to a calibration standard. Total lipid content was determined by subtracting the recovery and extraction standards. Measurements were taken in four replicates to get statistically significant results. Means were compared at different sampling intervals using a one-tailed student T-test with unequal variances. The alternative hypothesis was unequal means, while the null hypothesis was indistinguishable means.

3.4.6 Cell Viability

Cell viability was measured to determined how the culture health may evolve with time. Ideally, the bioreactor should be able to operate with good efficiency for extended periods of time. Cell viability was explored using flow cytometry (Accuri™ C6 Plus, DB Bioscience, USA) with the aid of the nucleic acid stain sytox™ green (ThermoFisher, USA). This stain is impermeable to living cells as it cannot cross intact cell membranes. However it can readily penetrate the compromised membranes of dead cells. Using this stain living and dead cells can be distinguished based off fluorescence. The stain has a $>$ 500-fold fluorescence enhancement upon binding to nucleic acids allowing cells to be easily distinguished. Dead cells will result in bright green fluorescence with an emission peak of 523 nm when excited by a 450-490 nm source. This allows for the health of cells in the bioreactor to be quantitatively observed. Fluorescence was observed in the green range with the FL1 channel (excitation at 488 nm and 533/30 nm filter).

The cell staining and cytometry procedure starts with adding 6 μL of 0.03 nM stock stain solution to 1 mL of sample that has been diluted to 10^6 $cells\ mL^{-1}$ with 0.2 μm filtered DI water. Samples were incubated for 15 minutes prior to fixing cells with 27 $\mu L\, mL^{-1}$ of 37 % formaldehyde. After 30 minutes the fixed cells were ran through the flow cytometer observing the FL1 and FL4 channel. Example analysis is shown in Figure 3.4 where 25% of the liquid culture cells were killed through heat treatment. The flow cytometer was set to capture 10,000 events with a flow rate of 14 $\mu m\ min^{-1}$, core size of 10 μm, and a

threshold of less then 80,000. Undyed samples were used for gating. The chlorophyll gating was applied based off the observed florescence peak in the undyed sample. Then using the chlorophyll containing population, the Sytox stain was gated based off the FL1 channel. Without any Sytox Green, all cells should show alive, thus the gate will capture all the undyed sample. This fluorescence range was used to determine where live cells would be expected in the dyed sample.

Before determining viability, chlorophyll fluorescence was used to distinguish algae cells from contamination. The contamination could be either pathogenic or cellular debris. Though not strictly bacterial or fungal pathogens, the chlorophyll intensity can give an idea on the level of contamination present in the sample. By first gating the data using red fluorescence via FL4 channel (excitation at 488 nm and 670 LP filter), the chlorophyll containing events can be distinguished from non-chlorophyll containing ones (the proposed contamination). Viewing these populations separately in SSC vs FSC supports the idea that the chlorophyll containing cells are a distinct distribution compared to the non-chlorophyll containing event.

Using flask grown samples as a control, a portion of it was heat treated at 85° for 20 min to kill the cells. Next several ratios of living and dead cells were mixed. Comparing the fluorescence of unstained control samples to ones stained with Sytox green allowed the sensitivity of the assay to be investigated. Running the stained control with 0% viability showed 96% of the cells dead based of the cutoff found with the unstained sample. This results suggests the method has reasonable precision as the heat treating may not have been completely effective. Figure 3.4 shows the method applied to a sample with a target of 75% viability. It was found to have an overall viability of 69.5%, which is reasonably close to the control.

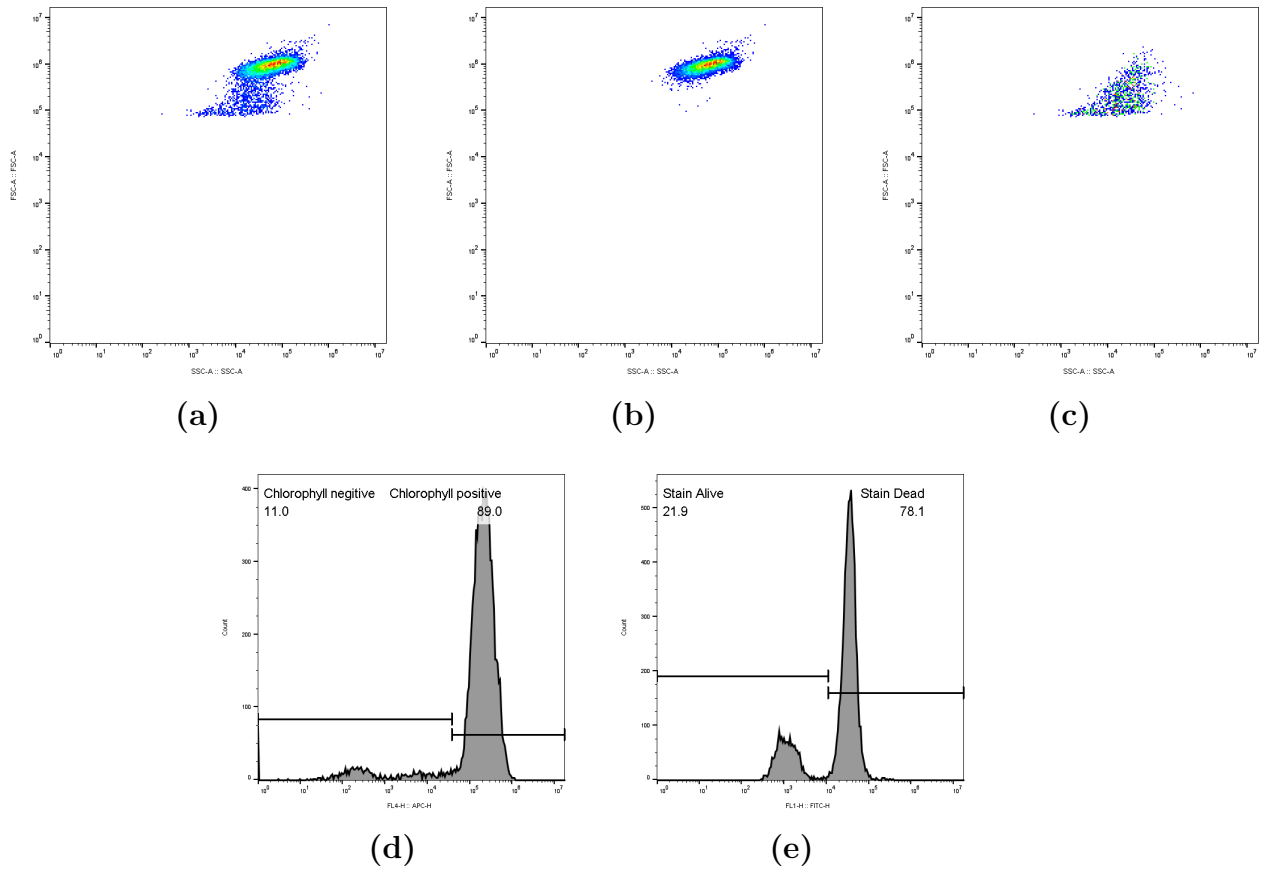

Figure 3.4: Example analysis using heat treated liquid culture (75% cells alive) **(a)** FSC vs FSS ungated sample **(b)** FSC vs FSS for chlorophyll containing events **(c)** FSC vs FSS for non-chlorophyll containing events **(d)** Chlorophyll bisection on FL4 channel (red) **(e)** Dead cell bisection on FL1 channel (green) chlorophyll containing population. (n=1)

Chapter 4

Results: Experimental

4.1 Hydrogel Selection

For the CSA design competition, only pPVA hydrogels were used. However with Design B, three hydrogels materials were investigated. The gel's physical properties and synthesis procedures are compared in Table 4.1. Physical properties of interest include tensile strength, strain at breaking, and water permeability. Main considerations regarding synthesis include synthesis time, consistency and apparent defeats of the final gels. The tensile strength of cPVA and pPVA gels were similar, while BC gels were significantly stronger. As a point of comparison, the tensile strength of arterial tissue is around 0.23 MPa [83]. This suggests though weaker, the PVA gels would still be strong enough to withstand the harvesting protocol in the bioreactor setup. The strain at time of breakage results indicates PVA to be more elastic than BC hydrogels. The superior elasticity of the PVA hydrogels would help the gel handle any shrinking/stretching that may occur during operation.

Hydrogel	pPVA	cPVA	BC
Tensile Strength (MPa)	0.6 [92]	0.563 [83]	1.62 [93]
Strain at Break (%)	130 [92]	120 [83]	39 [93]
Water Flux $\times 10^5$ ($g\ s^{-1} cm^{-2}$)	1.47	4.04	7.41
Synthesis Time (days)	2-3	3-4	12-17
Visible Defects	Bubbles	Shrinkage	Nonuniform

Table 4.1: Hydrogel Comparison

The final physical property compared was water permeability. This was investigated by measuring the water flux through each material under identical conditions. Using the flux cell previously described in Figure 3.2, the water transport through the hydrogel materials were measured using linear regression of the temporal mass data. The water transport was then divided by the exposed hydrogel area to determine a water flux. Only the linear portion of the data was used, as there was an initial transient response associated with the gel shrinking. Dry air at 15 psi was flown over the gel surface. As a control, aluminium foil was used in place of the hydrogel to investigate the setup accuracy. aluminium has essentially no water permeability ($< 0.01 g m^{-2} d^{-1}$) [94]. As seen in Figure 4.1, the aluminium foil had essentially no mass change. The calculated hypothetical flux using aluminium was $6.33 \times 10^{-7}\, g\, cm^{-2} s^{-1}$. This result is three orders of magnitude less than the hydrogel transport rates. This suggests the experimental resolution is at least two significant figures. The water flux of all hydrogels were on the order of $10^{-5}\, g\, cm^{-2} s^{-1}$. BC showed the highest water transport rate, followed by cPVA and pPVA. This result suggests BC would be able to deliver the most water and potential nutrients to the algae if used. However, seeing that all gels are on the same order of magnitude their performance should be comparable in this respect.

Looking at the synthesis procedures, the PVA-based gels had shorter synthesis times (days) compared to BC (weeks). Additionally, their synthesis method was simpler as cells do not need to be cultured. Between pPVA and cPVA gels, the latter has the distinct advantage of not needing refrigeration reducing equipment needs. The hydrogel quality is also a consideration when assessing synthesis procedures. The uniformity of the BC hydrogels is uncontrollable as live cultures are used to produce the material, and the pPVA hydrogels suffered from bubbles forming within the material. The cPVA gels showed the best uniformity of the three materials. Though shrinking of the gels could happen if the dehydration rate was too high, this was easily resolved by increasing the humidity in the drying enclosure. This was accomplished by using saturated sodium chloride solutions for humidity control (Relative humidity of 75%).

The pPVA and cPVA materials were selected for further investigation. Physical properties were comparable across all three materials. The superior elasticity of the PVA materials, as seen in the breaking strain, was attractive for the bioreactor design for improved reliability during the algae harvesting. The key consideration for selecting these materials however was the ease of synthesis and consistency of the resulting gels. As such bioreactor performance was investigated with pPVA and cPVA hydrogels and compared.

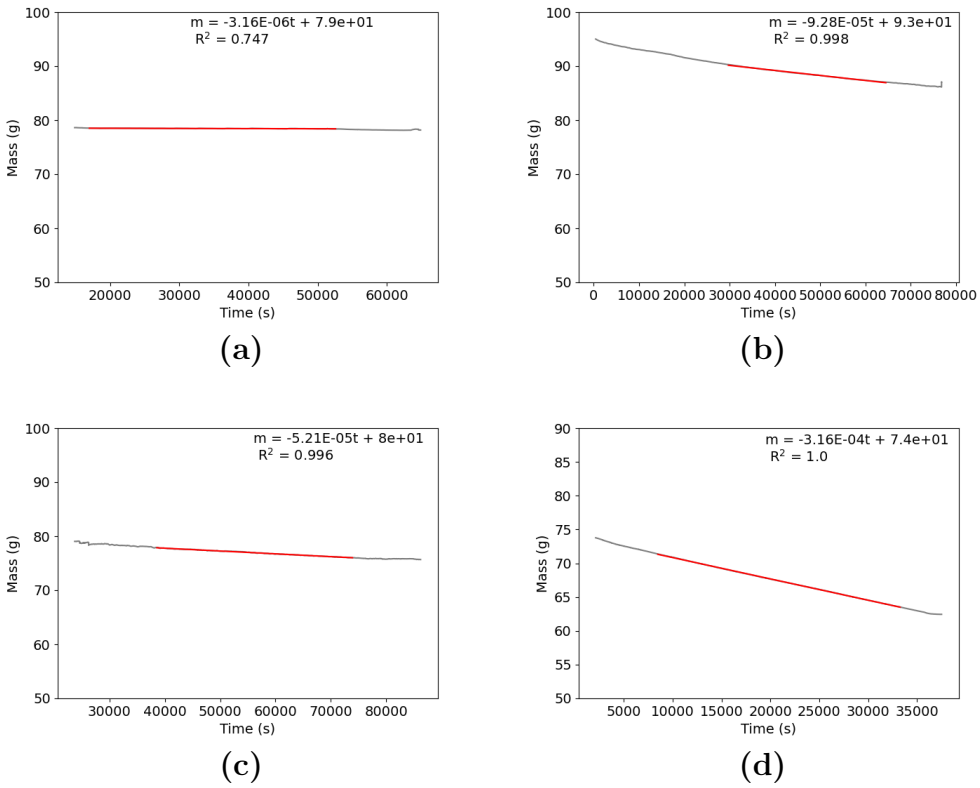

Figure 4.1: Transport results for **(a)** aluminium foil **(b)** pPVA **(c)** cPVA **(d)** BC

4.2 Bioreactor Design and Operation

The inoculation procedure successfully attached algae to the surface. The amount adhered varied between attempts, however increasing inoculum contact time to 5 min allowed for more consistency in initial cell loading. This suggests time impacts initial cell adhesion, and that longer contact times are beneficial for bioreactor performance. Growth was achieved with carbon free media (BBM). This supports the design principle of supplying inorganic carbon through the gas phase. The harvesting procedure was simple and effective. Using a handheld windshield scraper, or spatula, the algae was easily removed with no visual damage to the hydrogel surface. Furthermore, algae samples did not visually show any hydrogel debris. The simple and quick procedure helps to reduce labour time for operation. The harvested biomass had a paste like consistency suggesting limited amount of dewatering would be required for biomass processing.

(a) **(b)** **(c)**

Figure 4.2: Reactor B design **(a)** spacer ring to prevent leaking **(b)** reactors in operation **(c)** reactor side profile

An issue encountered with both reactor designs was leaks between joining parts, such as the frame and spacer. To remedy this issue design iterations were made with the frame, hydrogels and joining method. A combination of O-rings and gaskets proved most effective in design B in minimizing leaks. Additionally, the gel holder was modified with an extruded ring around the exposed hydrogel to compress against it to prevent liquid leaking into the glass compartment. To improve the seal between the base and gel holder, O-rings were added to both sides of a gasket to help make a tighter seal with the frame. This helped to minimize leaks with minimal torque on the clamp screws holding the assembly together. This reduced stress on the glass compartment which were liable to cracking when over tightened. The glass compartments allowed for conditioned air to be flown through the reactor that helped to limit the dehydration experienced in previous trials with Design A.

Due to the growing area size in Design A shrinking was an issue. Holes would form allowing media to drain from the internal flow channel drying the hydrogels out. To better support the substrate with minimal effect on transport properties, a fine wire mesh was cast inside. Introducing humidity control and the wire mesh limited the hydrogel shrinkage preventing it from tearing. Another issue observed in the original design, was bulging of the gel in the middle. To further improve mechanical strength, cross supports were added to the internally facing hydrogel frame component. This helped to produce a more structurally stable surface at both the small and large scale, reducing the bulging of the gel. As Design B had better humidity control, an internal mesh and supports were not needed.

The small scale Design A system was placed in a humidified enclosure to prevent excessive dehydration of the hydrogel. In this system a final yield of 0.1042 g corresponding to 6.202 $g\ m^{-2}$ was achieved. This result translated to an average productivity of 0.239 $g\ m^{-2}d^{-1}$. Initial experiments with reactor B design showed a $4.8x$ improvement in biomass production to 1.149 $g\ m^{-2}d^{-1}$. This suggests that the better humidity control in the reactor B design greatly enhanced the system operation. As such the reactor B design was further explored to evaluate the hydrogel-based bioreactor system.

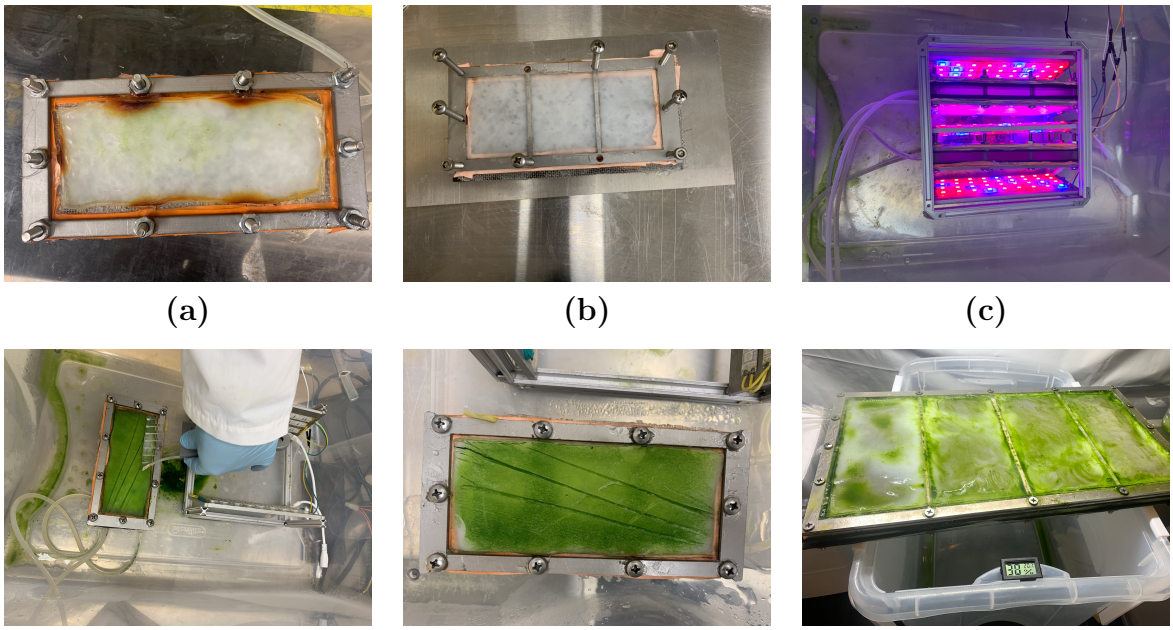

(a) **(b)** **(c)**

(d) **(e)** **(f)**

Figure 4.3: Reactor A design **(a)** shrinking issue **(b)** internal supports and PTFE tape **(c)** small scale **(d)** harvesting algae **(e)** algae growth **(f)** full scale module

4.3 Surface Coverage

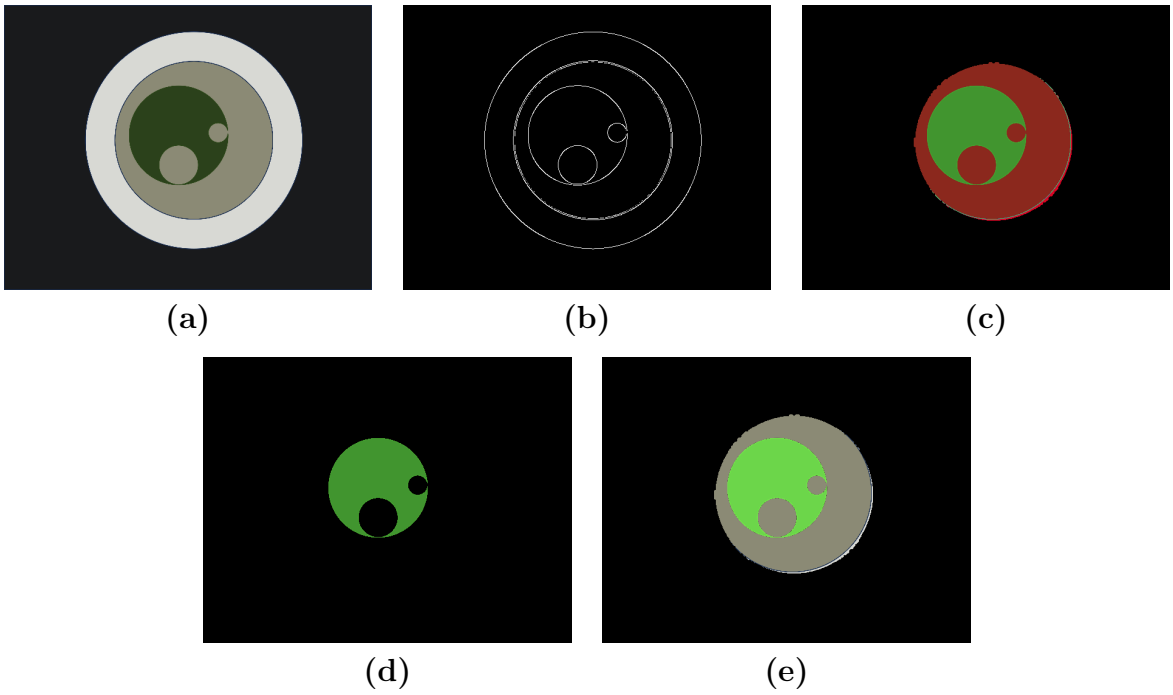

Figure 4.4: **(a)** Test Image **(b)** Detected Edges **(c)** HSV Colouring **(d)** Colour Threshold Applied **(e)** Final Image

The surface coverage analysis was first demonstrated on a toy image with a known surface coverage of 31.3%. Using the outlined algorithm, the calculated coverage was 31.1%. This result indicates reasonably accuracy for the algorithm. Though there is some discrepancy, having a defined procedure will allow different hydrogels to be compared. In some of the images, the algorithm failed to find the contour line corresponding to the gel edge. By marking the image with a colour contrasting circle around the gel, it greatly enhanced the algorithm's performance.

	Percent Coverage %			
Hydrogel	PPVA		CPVA	
Day	Total	Dark Green	Total	Dark Green
0	17.35	0.53	29.48	0.95
1	49.94	6.20	77.37	14.086
2	73.94	47.46	75.36	22.88
3	82.49	71.89	81.81	58.84
4	86.025	72.46	83.87	65.01

Table 4.2: Hydrogel Coverage Analysis for first 4 days

Surface coverage was analyzed over the first 4 days of growth. As can be seen in Table 4.2, the gel coverage steadily increased with time. Initial coverage was between 17.35% to 29.48% of the surface with only 0.53% to 0.95% of the area being above a darkness threshold. The drastically different coverage between the two gels could be explained by one having the inoculum more concentrated rather than evenly spread over the gel's surface. This is consistent with cPVA having a higher dark coverage amount initially. This threshold was used to distinguish between spares and dense coverage as it is important to understand not only how the algae layer spreads but also how it becomes denser. These results show that the inoculation technique used in the experiment were reasonable effective in producing growth across the entire gel surface within a few days. The majority of the hydrogel was covered with algae within 2 days, however dense coverage took significantly longer to occur.

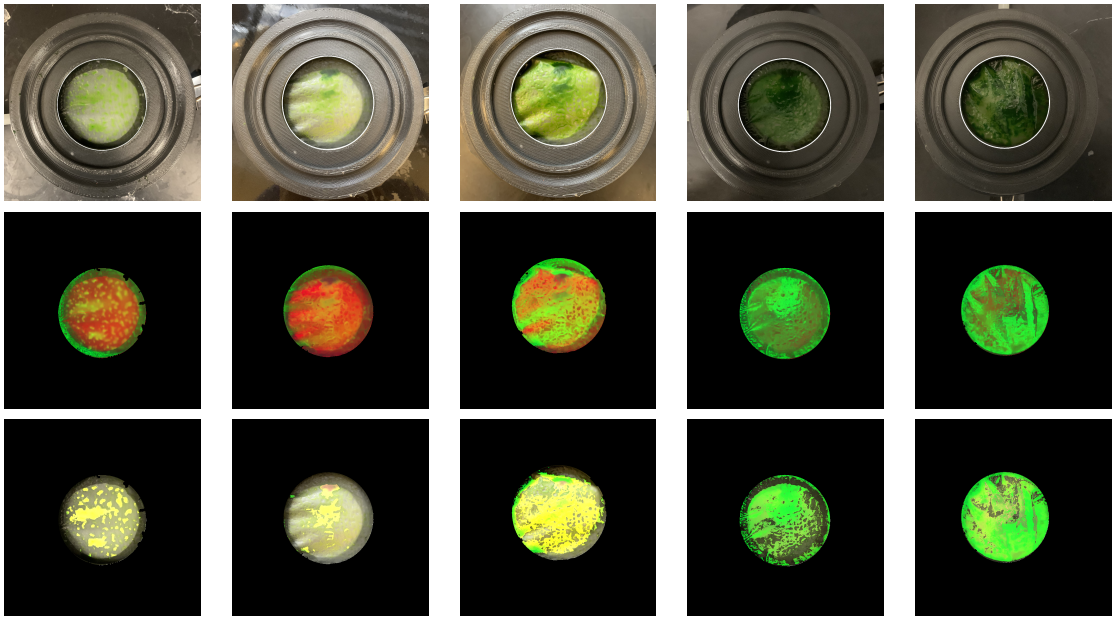

Figure 4.5: Original, HSV colouring and coverage for cPVA gels for first 4 days

In previous attached cultivation experiments initial cell loads were considerable higher than in our setup. Liu et al. evenly filtered 10.6 $g\ m^{-2}$ of algae for the initial cell loading [23], while our starting concentration was just 0.2 $g\ m^{-2}$. As coverage was not uniform for several days, using an inoculation technique similar to their method may result in improved growth rates. However, in applications where inoculum size is constrained, as is the case for extra-terrestrial use, the inoculation procedure outlined in this work may be beneficial from a launch weight perspective. Using this procedure would require just 218 mL of algae concentrate per m^2 of growing area.

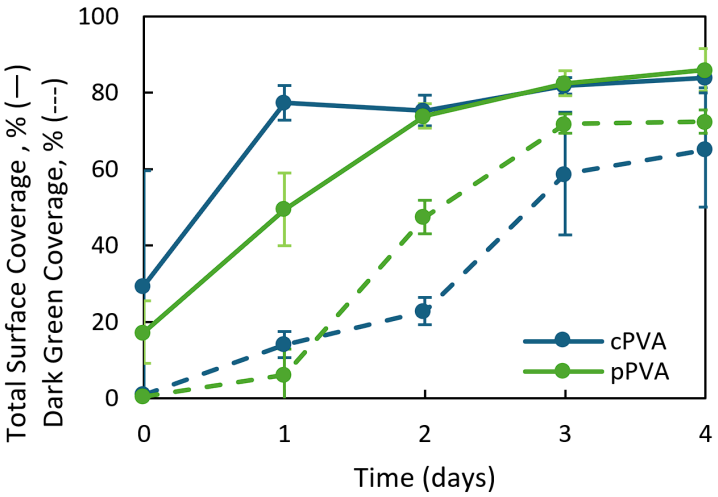

Figure 4.7: Surface Coverage Results

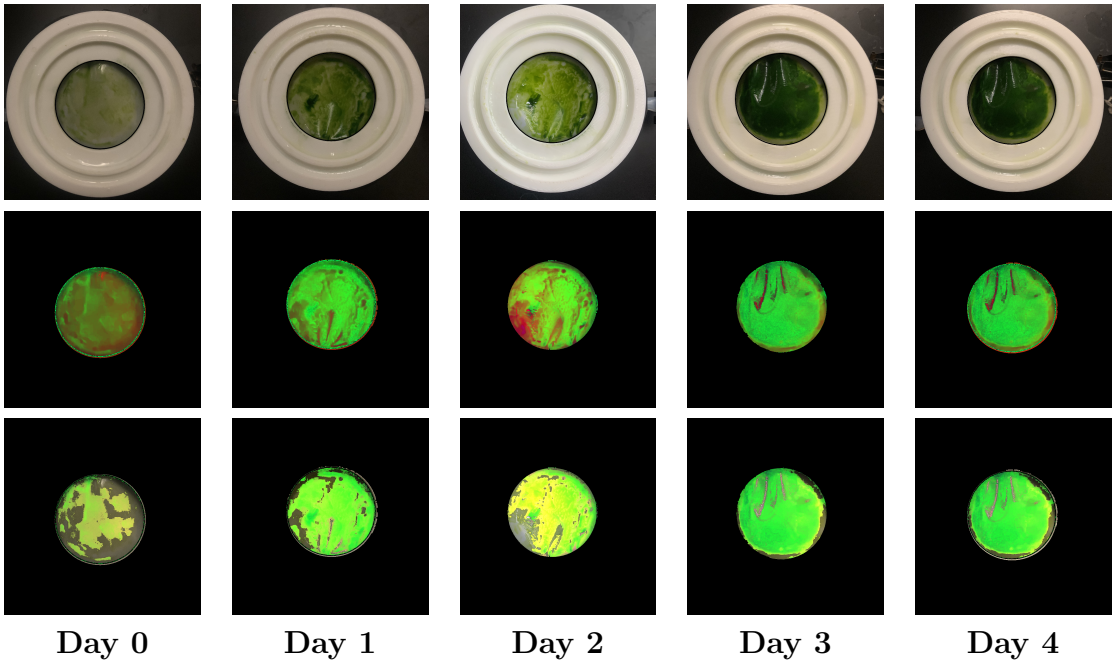

Figure 4.6: Original, HSV colouring and coverage for pPVA gels for first 4 days

4.4 Growth Results

The hPBRs were seeded with approximately 0.2 $g\ m^{-2}$ of inoculum. As not all the inoculum attached to the gel it is difficult to accurately measure the initial cell loading. However, reasonably consistent results were found between independent trials suggesting it could be reasonably constant. Over 23 days, the biomass on the gels steadily increased to a maximum of 53.2 $g\ m^{-2}$ and 71 $g\ m^{-2}$ for pPVA and cPVA respectively. The average biomass productivity achieved in the experiments were 2.4 $g\ m^{-2}d^{-1}$ (pPVA) and 3.2 $g\ m^{-2}d^{-1}$ (cPVA). The biomass growth was lower than observed in the system described by Lui et al [23]. They achieved a biomass productivity of 5.2 $g\ m^{-2}d^{-1}$ with a final accumulation of 66.3 $g\ m^{-2}$ of biomass using *Scenedesmus obliquus*. However, in their study they used 2% CO_2 enriched air.

As seen in Figure 4.8, the specific growth rate decreases substantially in the first few days. However, as compared to a flask culture also grown in BBM, the specific growth rate of the algae-based cultivation system was similar. The high specific growth rate initially may be contributed to the cell utilising stored nutrients and energy from its growth in the starter culture containing TAP media. In a recent study, another green microalgae, *Graesiella emersonii*, was found to grow in nitrogen depleted conditions and store nitrogen as protein [95]. A similar phenomenon may be possible here. Alternatively, the low cell densities could reduce the amount of cell shading allowing for higher growth rates. This result shows that the algae-based attached cultivation method had promise as it performed as well as a liquid culture in terms of specific growth rate. Attached cultivation experiments involving *C. vulgaris* reported similar final biomass densities in the range of 50-80 g/m2 [96].

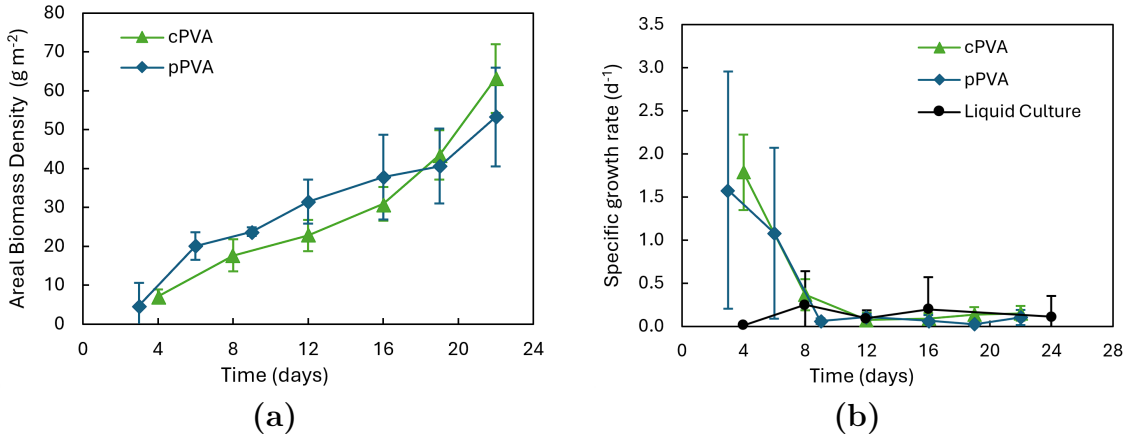

Figure 4.8: Reactor B **(a)** growth rate **(b)** Specific growth rate compared to flask culture

4.5 Water Consumption

The estimated mean evaporative loses from an open pond system placed in the US was calculated to be 24.4 $kg\ m^{-2}d^{-1}$ for a stream producing 25.2 $g\ m^{-2}d^{-1}$ [97]. Evaporation and harvesting are a major challenge with respect to water usage in algae cultivation. In the hPBR system water usage was determined by comparing the liquid reservoir volume at the beginning and end of a trial. The average water loss rate was found to be 1.42 $kg\ m^{-2}d^{-1}$. This represents a 92% water saving. Though the productivity of our system did not match that used in their analysis, the water demand per g of biomass was less. In our experiment we found that just 0.44 $kg\ g^{-1}$ of water were needed for cultivation as compared to $1-1.6\ kg\ g^{-1}$ in the open pond system [98]. Other attached cultivation systems achieved water consumption rate around $0.714kgg^{-1}$ [80, 99].

Though not stated, inferring from the design and observations Wang et al. achieved a water demand between 1.01 and $1.69kgg^{-1}$ in their pilot plant system with $57.6m^{-2}$ of growing surface on a $11m^{-2}$ area footprint [67]. It is important to note that conditioned air was used in our experiment which impacted overall water demand. Other solid-state cultivation experiments that used conditioned air achieved water demands as low as $0.0669kgg^{-1}$ [80]. In this study batch cultivation approach was employed. However, by optimising the growth in a semi-continuous fashion may allow for higher overall productivity, and better water utilization.

4.6 Cell Viability

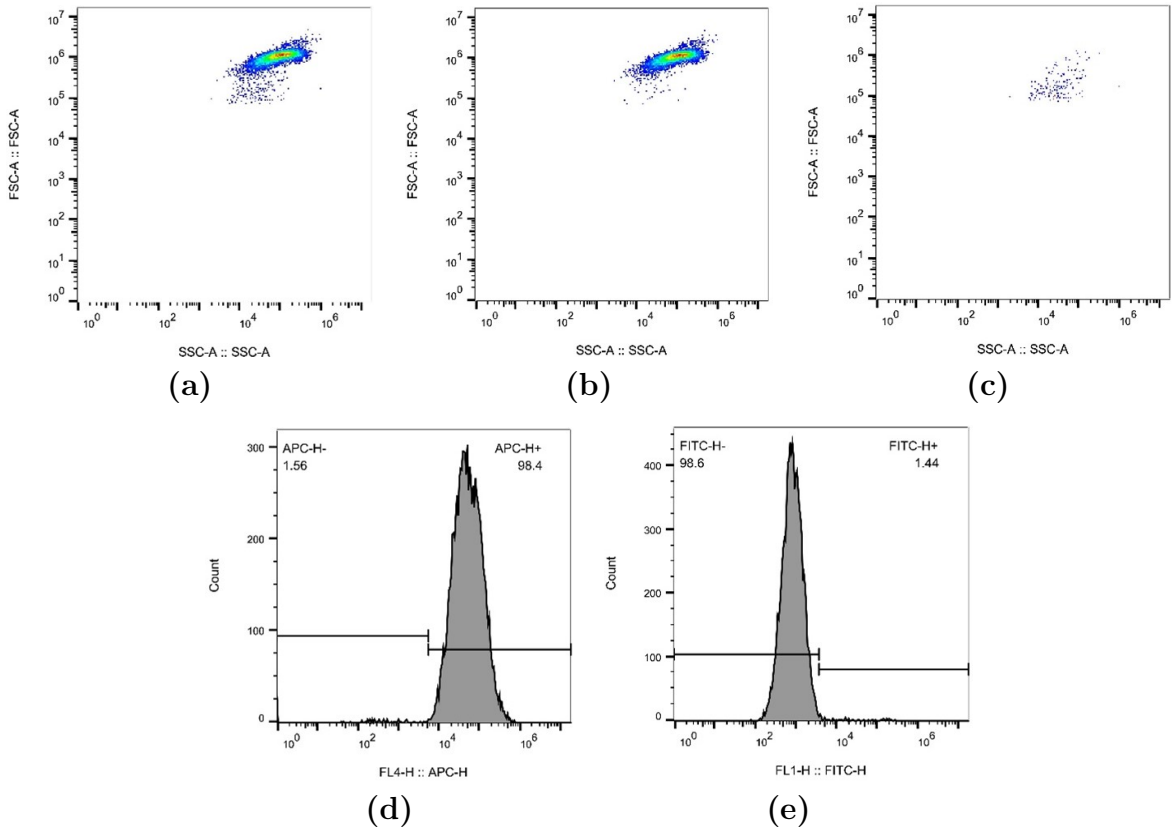

Figure 4.9: cPVA hPBR on day 6: **(a)** Flow cytometry population **(b)** chlorophyll containing population **(c)** non chlorophyll containing population **(d)** FL4 chlorophyll segmentation **(e)** FL1 live cell segmentation for chlorophyll containing population.

Using flow cytometry and Sytox green staining, the health of the cell culture was evaluated in order to assess the long term viability of the bioreactor design. Samples were taken from the bioreactors for analysis on day 6. The health of the algae in the solid-state cultivation system was investigated using flow cytometry. It was seen that following 6 days of cultivation the cell viability remained high. Chlorophyll florescence was observed in 98.4% of events with both substrates which suggests a low level of contamination and/or cell debris in the cultivation system. The overall cell viability was determined to be 97%

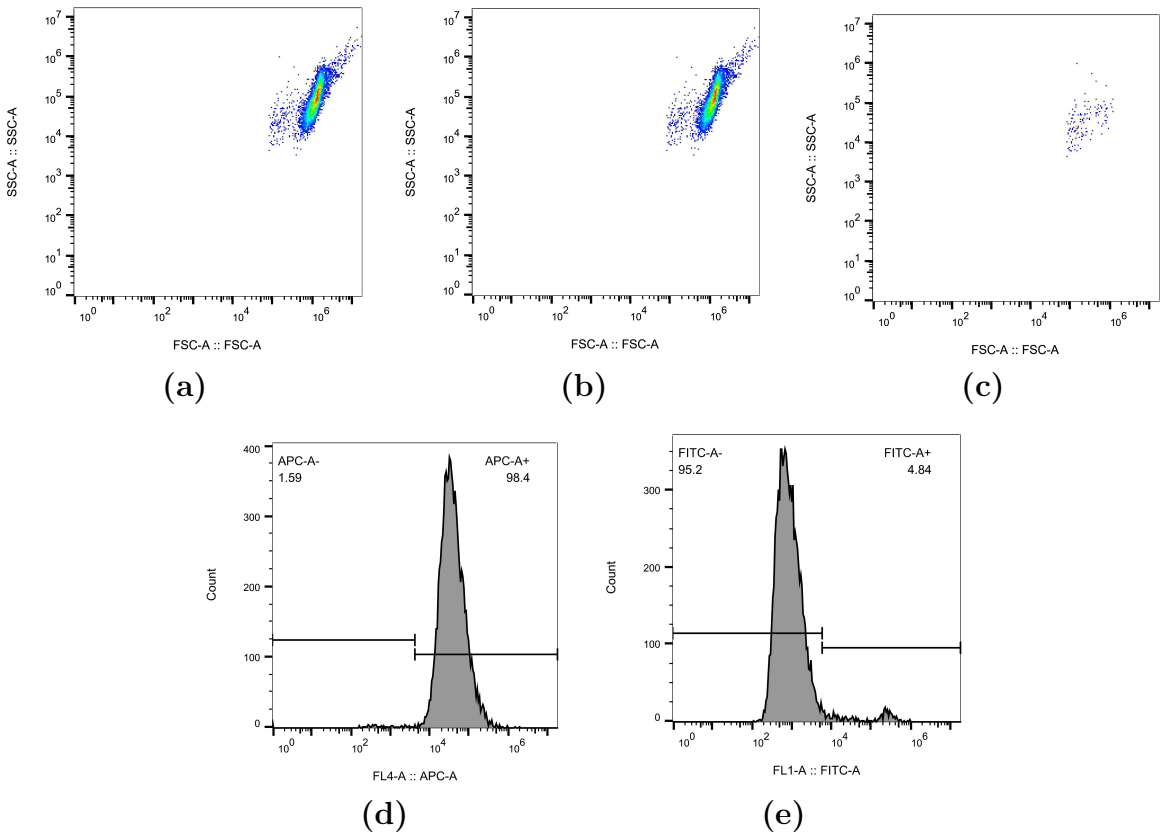

Figure 4.10: pPVA hPBR on day 6: **(a)** Flow cytometry population **(b)** chlorophyll containing population **(c)** non chlorophyll containing population **(d)** FL4 chlorophyll segmentation **(e)** FL1 live cell segmentation for chlorophyll containing population.

and 93.7% for cPVA and pPVA respectively. This suggests that the algae culture is maintaining good health as the majority of the cells are alive. As a point of comparison, the maintenance culture used for *C vulgaris* in the stationary phase was found to consist of 80% living cells. To the best of our knowledge culture viability has not been explored in other solid-state cultivation studies. This result demonstrated the feasibility of the operating principle of the system as the reactor can maintain the cell populations health.

4.7 Nutrient Supply

At each time point the nutrients available to the microalgae were measured by suspending the harvested algae in DI water and analysing the supernatant upon centrifugation. The phosphate and nitrate concentrations were measured using standard procedures. As seen in Figure 4.11, the nutrients available per gram of biomass fluctuated substantially throughout the trails and within replicates. This suggests high variability in the nutrient diffusion though the hydrogels. However, a more likely explanation is that the resolution of the methods used in the experiment was not able to capture the low concentrations present in the samples introducing error to the measurements. As the algae do not grow in a suspension, it was difficult to quantify available nutrients, and by which metric to compare the results to. Previous work in this area avoid quantifying nutrient supply, and rely on qualitative results to indicate nutrient quality to the biomass. Instead of milligram of nutrient per gram of biomass, a better metric may be milligrams per gram of free water in the paste, however this was not measured in this work.

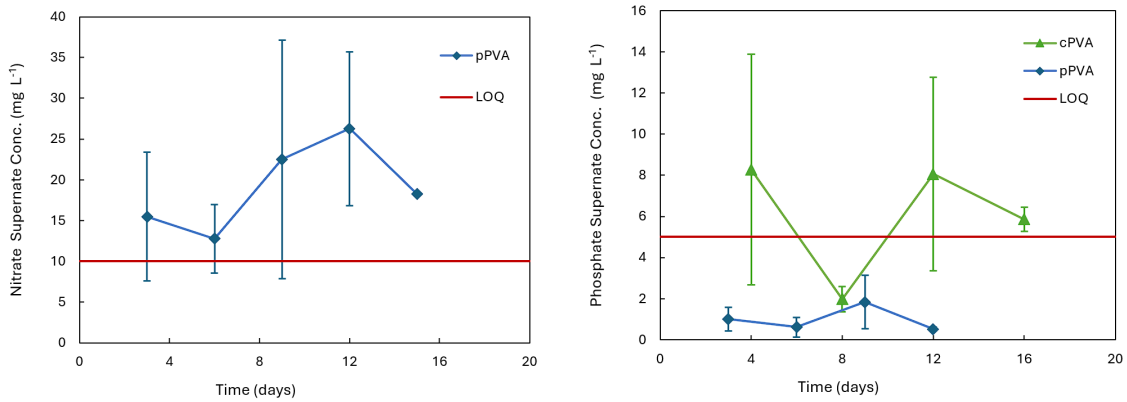

Figure 4.11: Nutrient supply Results **(a)** Nitrate **(b)** Phosphate

4.8 Biomass Composition

As biomass quality is dependent on the cellular environment, it is import to understand how the biomass composition may change with time. FAMEs content was determined using gas chromatography. The lipid content of the microalgae increased with cultivation

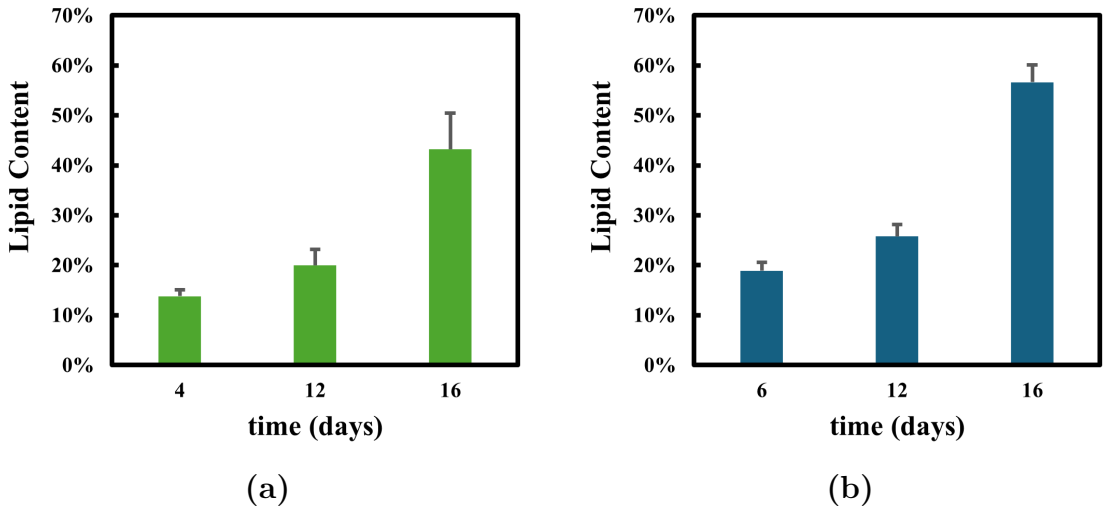

Figure 4.12: Lipid content of algal biomass **(a)** cPVA **(b)** pPVA

time in the system as seen in Figure 4.12. From day 4 to 16 the lipid content of algae increased from 13.8% to 43.2% when grown on cPVA and from 18.9% to 56.6% from day 6 to 12 on the pPVA gel. On day 16 the lipid content of the cPVA and pPVA gels were not statistically different suggesting the two hydrogel substrates had similar performance in terms of biomass quality. This result suggests that the cultures may be nitrogen limited, which is supported by the nutrient measurements made. Meng et al., found the lipid content of *C. vulgaris* to be between 20-25% using a porous substrate PBR [74]. Another study looking at biofilm-based growth on a concrete slab found a lipid content of 26.8% [21]. Other solid-state cultivation experiments observed lipid synthesis and lower nitrogen content for attached growth as compared to suspended cultures [100, 74]. The development of the algae layer on the substrate surface may add to the mass transfer resistance of nutrients through the gel leading to decreasing nitrogen and phosphate availability to the microalgae. This is consistent with the nutrient supply analysis that suggested that the biomass is nitrogen limited in the system. It has also been shown in the literature that mechanical stresses can also induce lipid accumulation in microalgae [101]. As the algae is not in a free suspension, but is accumulating on the gel's surface, there will be more mechanical stresses experienced by the cells. The stresses will arise from contact with the hydrogel as well as other cells in the paste that forms. This may help explain the lipid content change over time in the reactor. In line with our results, Ye et al. found in their experiments a final lipid content of 47.53% though over a shorter cultivation time [96]. It has been observed that high light intensities can induce lipid production [102] as well.

4.9 Pigment Analysis

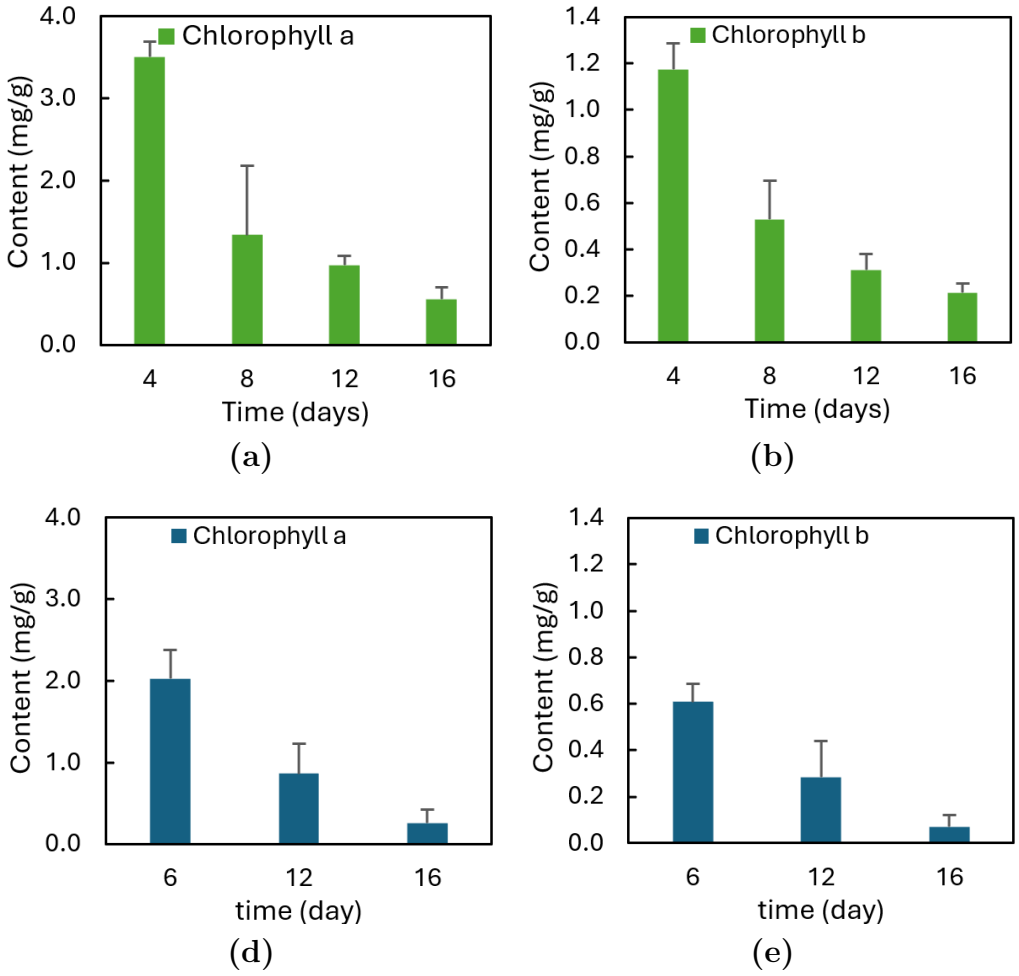

Figure 4.13: For cPVA trials **(a)** Chlorophyll a and **(b)** Chlorophyll b content. For pPVA trials **(d)** Chlorophyll a and **(e)** Chlorophyll b content.

The pigment content of microalgae can be an indicator on the health of the culture, and its ability to efficiently utilise light for photosynthesis. Figure 4.13 shows the impact of the hPBR design on chlorophyll content with time. Chlorophyll extraction was performed on dried biomass in triplicates. It was observed that the chlorophyll content steadily decreased with time. For pPVA, the change for the most abundant pigment, chlorophyll a, was from

1.44 $mg\ g^{-1}$ on day 6 decreasing steadily to 1.26 $mg\ g^{-1}$ on day 12, and 0.48 $mg\ g^{-1}$ on day 16. Similarly, chlorophyll b content decreased from 0.477 $mg\ g^{-1}$ for day 6 to 0.363 $mg\ g^{-1}$ and 0.129 $mg\ g^{-1}$ on day 12 and 16 respectively. Chlorophyll c content is typically negligible in *C. vulgaris* so was not analysed. The same trend was observed for cPVA. Typical pigment concentrations in *C. vulgaris* range from $0.25 - 9.63\ mg\ g^{-1}$ for chlorophyll a, $0.072 - 5.770\ mg\ g^{-1}$ for chlorophyll b [103]. This suggests that the pigment content is on the low end of what is typical for this species. The decrease in chlorophyll content may be explained by the microalgae redistribution it's intracellular nitrogen in response to nitrogen depleted growth conditions [104]. This explanation would be consistent with other results indicating low nitrate availability. Other nutrient limitations may also result in low pigment content in microalgae. Phosphorus is essential for ATP synthesis. As such, low phosphate concentrations has been shown to lead to decreasing chlorophyll content in microalgae [105]. The absence of other micronutrients such as iron, zinc, and manganese can have similar effects. Exposure to a high light intensity is an alternative explanation for the reduction in chlorophyll content [102]. It is important to note that in liquid cultures individual cells are not constantly exposed to light, but will be shaded by each other. This creates light attenuation within the culture where light intensities experienced by the algae varies. In our system the algae is fixed in space. The algae on the surface will experience no light intensity variation during growth. To over come this challenge light dark cycles may be effective in increasing pigment content. It has shown in liquid cultures that light/dark cycles can increase chlorophyll compared to continuous light cultures [105]. Other solid-state cultivation experiments involving C. vulgaris also observed decreasing pigment content with time [96].

4.10 Discussion

In this work, two hPBRs were designed that achieved complete phase separation. Growth parameters were quantified for two solid supports, cPVA and pPVA. Design B was more reliable, while design A suffered from reliability concerns and lower productivity. Design B provided better conditions for growth and higher cell viability. A terminal biomass of 71 $g\ m^{-2}$ was achieved in the system corresponding to a average growth rate of 3.2 $g\ m^{-2}d^{-1}$. The specific growth rate was found to be similar to a flask culture. Lipid accumulation over time suggests nutrient limitations are present. Lipid content increased from 18.6% to 56.6 % over 10 days. Similarly, Chlorophyll content decreased over time. Further studies exploring the effects of harvesting schedule on growth rate, and the concentration of nutrients in the nutrient reservoir will help elucidate if growth rate and nutrient

limitation are occurring. Different hydrogel substrate may also help improve productive due to differences in transport properties and can be explored as well. Future design iterations should also start considering material costs and the target minimum biomass selling price.

Part II

Continuum Modelling

Chapter 5

Background: Hydrogels

5.1 What are Hydrogels?

Hydrogels are a class of materials composed of a crosslinked hydrophilic polymer lattice surrounded by adsorbed free water. The interstitial water is allowed to flow through the matrix, just as in porous media [106, 107]. These materials can experience large reversible volume changes in response to their environment and can hold tremendous amounts of water; 10-1000 times their original weight [108]. A wide variety of polymers are suitable for forming hydrogels, allowing them to have properties tailored to a wide variety of applications. The polymers used, cross-linking mechanism, and manufacturing process can influence the resulting gel properties. Crosslinking can be achieved through covalent bonding, hydrogen bonding, van der Waals interaction or physical entanglement of polymer chains [109].

Hydrogels can be synthesised in a number of ways. Crosslinking can be initiated through physical means like temperature cycling, which involves repeated heat or freeze treatments of the gelling solution [110]. This is particularly effective with protein-based hydrogels as temperature can disrupt their tertiary structure, and other long chain polymers to promote entanglement. Alternatively, chemical crosslinking can be employed to form hydrogels through the addition of a crosslinking agent. Chemical crosslinking can be initiated through pH changes (by altering polymer solubility), ion interactions, and bonding between side chains [111]. With respect to food applications, chemical crosslinking agents pose a challenge due to the residual unreacted chemicals that may be present in the final hydrogel. This finding was supported by previous work done by Hannah Czech &

Valerie Ward (unpublished). However, there are several crosslinkers that have low toxicity, and residual contamination can potentially be drawn out of the gel by diffusion. In this project poly(vinyl) alcohol (PVA) gels are used for the hPBR system (Chapter 3). They were synthesized using physical and chemical crosslinking. Physically crosslinked gels were formed through chain entanglement from repeated freeze-thaw cycles (4 cycles). Chemically crosslinked gels were formed through the addition of sodium trimetaphosphate (STMP) in a basic environment. STMP phosphorylates the hydroxyl side groups on PVA forming linkages between chains [112].

Hydrogels have a plethora of applications ranging from life sciences, material science, food and electronics. In life sciences, the high degree of biocompatibility the material exhibits have been exploited for medical implants such as artificial cartilage [113], wound dressings [114], and scaffolds for grafts [115]. Soft Contact lenses are often produced from hydrogel networks as well [116, 117]. Hydrogels are also well suited to tissue engineering application as they produce a similar micro environment as human tissue [118]. Drug delivery is another major research area for the material [119]. In the food industry, hydrogels have been used as additives to improve texture and nutrition of products. For example, many low fat dairy products contain protein-based hydrogels to mimic the creamy texture of fat in the product [120].

Unique properties hydrogels may poses include their ability to retain water, tunable mechanical properties, and responsiveness to external stimuli such as temperature, pH, and voltage potential. Hydrogels can form rigid structures at low water content while also becoming more elastic as water content increases [121]. The ability to vary the elastic modulus of hydrogels has allowed hydrogels to be used in tissue engineering application where the functional micro environment can be manipulated to drive cell differentiation [122]. Some hydrogels have also been shown to have shape memory, allowing them to be deformed and return to their original shape under specific conditions. Hydrogel may experience mechanical changes in response to external factors such as temperature, pH, electric fields and light [123]. Another relevant mechanical property of hydrogels is the effective network pore size. Pore size is dependent on the crosslinking density in the network and is also impacted by the degree of swell of the material. Pore size is a particularly important property in drug delivery applications as it directly impacts the diffusion of small molecules through the material. As the water within the material is free to move, small molecules can diffuse through the liquid within the gel, however this diffusion is hindered by the tortuosity and size of the pores in the material [109]. By tailoring the diffusion rates through the hydrogel, drug release from hydrogel implants can be engineered for more

sustained delivery of therapeutics to target location allow for more effective treatments. Bio-compatibility is another property that is favourable in many hydrogels for applications in medicine and food additives.

5.2 Thermodynamics of Water-Polymer Mixtures

As previously mentioned, hydrogels are hydrophilic polymer networks that do not completely dissolve in water due to crosslinking between chains. As such, the starting point for understanding the thermodynamics of hydrogel networks is the thermodynamics of polymer solutions. Flory-Higgins theory may be used to describe such systems. Suppose instead of a continuum the system is presented as a lattice. Each site in the lattice can either be occupied by a solvent or solute molecule. Using this framework, Flory accounts for the dissimilarity between the size of the polymer and the solvent molecules by specifying each segment of the macromolecule being one lattice site, similar to each solvent molecule. The entropy of mixing can thus be determined by applying mean field theory and Boltzmann's equation $S = k \ln \Omega$ where k is the Boltzmann constant ($k = 1.381 \times 10^{-23} J\ K^{-1}$) and Ω is the number of unique arrangements of molecules [124]. The Gibbs free energy change of mixing can be determined where n is the number of moles, ϕ is the volume fraction, and χ_{12} is the Flory-Huggins Parameter for the polymer-solvent system, which is a material-specific parameter that captures the interactions between polymer and solvent molecules.

$$\Delta G_{mix} = RT \left[n_1 \ln \phi_1 + n_2 \ln \phi_2 + n_1 \phi_2 \chi_{12} \right] \tag{5.1}$$

The first thermodynamic framework for hydrogel swelling was proposed by Flory and Rehner. Starting with Gibbs free energy of mixing, additional contributions were considered for the elastic energy from configurational changes in the polymer, and an ionic osmotic pressure term for polyelectrolyte hydrogels (not considered here) [126]. Flory-Rehner's thermodynamic model includes the enthalpy and entropy of mixing between the polymer and solvent derived using the Flory-Huggin's Theory previously described, and the entropy from the polymer elasticity. The change in Gibbs free energy for the water in a hydrogel system can be described as:

$$\Delta G = \underbrace{k_B T \left(n_1 \ln x_1 + n_2 \ln x_2 \right) + k_B T \chi n_1 x_2}_{\text{Mixing Term}} + \underbrace{\frac{k_B \nu_e T}{2} \left(3a_s^2 - 3 - \ln a_s^3 \right)}_{\text{Elasticity Term}} \tag{5.2}$$

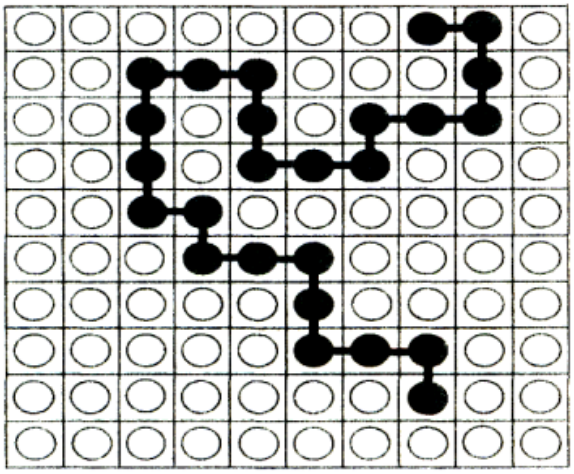

Figure 5.1: Lattice where polymer is black and solvent white [125]

with:

$$x_1 = \frac{n_1}{n_1 + n_2}; \quad x_2 = \frac{n_2}{n_1 + n_2}; \quad a_s^3 = \frac{V}{V_0} = \frac{V_0 + n_1 v_1}{V_0} = \frac{1}{x_2}; \quad \nu_e = \nu - 2n_2 \tag{5.3}$$

Where n_1 is the number of molecules of solvents, n_2 polymer molecules, x_1 and x_2 are mole fractions, ν is the number of crosslinking units, ν_e excludes the two free ends of the original polymer to give the number of elastic segments, and a_s is the ratio of chain extensions in one direction. For isotropic swelling a_s is related to the volume of the polymer before (V_0) and after (V) swelling. The first term is the entropy of mixing contribution followed by the enthalpy of mixing, where χ is the Flory-Huggins parameter. $\chi > 0$ means the mixing is endothermic, and $\chi < 0$ means mixing is exothermic, which is the case for most polymers. The last term is the configuration entropy of the polymer as the chains extend. It is important to note that the effect of pressure is not considered. In reality the pressure within the hydrogel can be considerably greater than ambient pressure. Chemical potential is the change in Gibb's free energy with number of molecules:

$$\begin{aligned}\mu - \mu_0 &= \frac{\partial \Delta G}{\partial n_1}_{T,p,n_2} \\ &= (\Delta\mu_1)_{pl} + (\Delta\mu_1)_{el} \\ &= RT\left[\ln(1-x_2) + x_2 + \chi x_2^2\right] + \frac{RT\nu_w n_e}{V_0}\left(x_2^{1/3} - \frac{x_2}{2}\right)\end{aligned} \tag{5.4}$$

Where $n_e = \nu_e/N_a$ is the molar number of the effective crosslinking unit, and ν_w is the molar volume. The first term accounts for the solvent-polymer interaction. $-(\Delta\mu_1)_{pl}/\nu_w$ is the osmotic pressure. The second term is the polymer conformation change, where $-(\Delta\mu_1)_{el}/\nu_w$ is the elastic stress in the polymer [126]. When only isotropic stresses are considered, as in a one-dimensional frame, this stress is an elastic pressure p_e, or the effective pressure of the porous medium. When at equilibrium with a pure solvent (μ_w^0) , the following expression can be posed:

$$\left[\ln(1-x_2) + x_2 + \chi x_2^2\right] + \frac{\nu_w n_e}{V_0}\left(x_2^{1/3} - \frac{x_2}{2}\right) = 0 \tag{5.5}$$

In Flory-Rehner Theory the chemical potential of the water within the hydrogel has contributions from the free energy change from favourable polymer-water mixing and the free energy from elastic changes within the material due to the crosslinking. These contributions are related to pressures within the material. As will be shown in Section 5.3, the thermodynamics of water within the hydrogel can be presented in terms of an osmotic pressure and elastic pressure generated by the crosslinked polymer chains, and in the limit of small polymer fractions (van't Hoff"s law) this relation can be further simplified.

5.3 Transport through Hydrogels

There has been several models proposed to describe the movement of water through a hydrogel matrix, with varying success. Many proposed models are empirical in nature, lacking the fundamental understanding of the underlining mechanism, and/or poorly capturing the transport phenomena occurring. Previous investigation into the transport properties of polymer gels can be classified as either solution-diffusion models or poroelastic models [127]. Solution-diffusion models view the polymer-water system as homogeneous and take diffusion as the dominant process for mass transfer within the hydrogel. Poroelastic models

on the other hand attempt to capture the physics of hydrogel systems by accounting for both fluid transport and the deformation of the polymer lattice in response to the fluid movement. These models follow a continuum approach, where fluid flow can be either modeled with diffusion, but more commonly through purely advective transport using Darcy's law against the porous media like polymer phase. Thermodynamics govern the movement of water and polymer within the system. Poroelastic models applied to hydrogels incorporate the free energy of swelling, similar to Flory-Rehner Theory [128] where there are contributions from the deformation of polymer chains, mixing between water and polymer, and the chemical potential of the mixed water.

5.3.1 Solvent - Diffusion Models

Many water transport models for hydrogels have been centred around soft contact lenses as high water transport rates may deplete the post-lens film leading to corneal desiccation and discomfort [129]. Of these models many prescribe diffusion as the underlining mechanism for transport.

Diffusion based transport models have found wide acceptance for the transport of solutes through saturated hydrogels submerged in fluid with applications in agriculture and drug delivery. Ritger and Peppas were the first to demonstrate that molecule release from a hydrogel can be accurately modelled for roughly half of the time release profile (M_t/M_∞) either by Fickian or non-Fickian diffusion through a simple semi-empirical exponential relationship shown below for a semi-infinite hydrogel slab [119].

$$\frac{M_t}{M_\infty} = kt^n \tag{5.6}$$

Where the constant k captures the characteristics of the polymer-solute system, and n is a diffusion exponent. Fickian diffusion is present when $n = 0.5$, and is non-Fickian when greater [130]. Similar correlations have been proposed for other geometries as well. Other researchers have built on this model for solute diffusion and have applied it to water transport as well.

Fick's first law of diffusion is a closure for diffusion. It describes the relative movement of one chemical species (A) through a binary mixture of A and B due to a gradient in chemical potential (commonly a concentration gradient of A) [131].

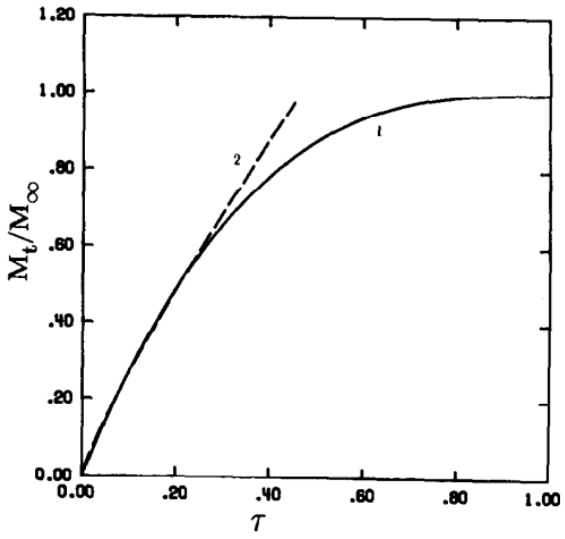

Figure 5.2: Ritger-Peppas release profile (line 2) [119]

$$\mathbf{j}_A = -\rho \mathscr{D}_{AB} \nabla \omega_A \tag{5.7}$$

However, the canonical definition of diffusion, with respect to component velocities, is the difference between component A's velocity and the mass-average velocity of the mixture. The mass flux from diffusion is therefore defined as the following

$$\mathbf{j}_A = \rho \omega_A (v_A - v) = -\rho \mathscr{D}_{AB} \nabla \omega_A \tag{5.8}$$

From this definition it can be shown that for diffusion to take place the dilute species, A, and the bulk species, B, must freely move, or rather that there must be counter-diffusion of the other species if the continuum is assumed to be stationary ($v = 0$). Therefore the mass continuity of a multicomponent mixture has two main contributions, movement through advection, and movement through diffusion (if homogeneous reactions are ignored).

$$\frac{\partial \rho}{\partial t} = \underbrace{-\nabla \cdot (\rho v)}_{\text{advection}} + \underbrace{\nabla \cdot (\mathscr{D} \nabla \rho)}_{\text{diffusion}} + \underbrace{r}_{\substack{\text{Homogeneous} \\ \text{reaction}}} \tag{5.9}$$

When considering transport through a hydrogel, the solute is diffusing through the water contained within the gel, and *not* the polymer. The polymer is not a mobile species due to crosslinking which fixes the relative position of polymer molecules. The diffusivity ($\mathscr{D}$) within the hydrogel will be lower than the diffusivity in a bulk solution due to the tortuosity of the pores that water can flow through within the hydrogel similar to that of porous media. This leads to an effective diffusivity of solutes within the hydrogel which is dependent of pore size that is affected by water fraction, chemical makeup of the gel, and crosslinking density.

Water transport though a hydrogel does not match this definition of diffusion. Firstly, though combined, the water and polymer form two distinct phases as demonstrated by the inability to dissolve a hydrogel. Secondly, though the polymer phase will move in response to the swelling and shrinking of the domain (representing a moving boundary), the polymer does not respond directly to the movement of water within it as the polymer chains are fixed due to crosslinking. As such the polymer does not act as a counter-species for the molecular diffusion of water. This can be observed through the steady-state flow of water through a hydrogel in equilibrium between water on one side, and air on the other.

Diffusion based models for water transport through hydrogels are essentially empirical in nature relying on an effective diffusivity to relate the chemical potential within the hydrogel to the flow of water through it. The Stefan-Maxwell (S-M) diffusion framework (equation 5.10), which is a more generalized version of Fickian diffusion, has been used to empirically fit water flux data. S-M diffusion accounts for multiply modes of diffusion while also accounting for multi-component transport. It can be interpreted as a force balance between the friction species (i) is exposed to due to its relative motion to another species (j), and the overall driving force the molecule is exposed too [116]. This more generalized model accounts for the non-ideal nature of the polymer-water solution due to the size difference between the molecules. This helps to reduce the concentration dependence of the diffusion coefficient. The swelling/shrinking of the domain is determined through conserving the

mass of polymer to calculate the gel thickness [27].

$$\underbrace{c_i \nabla \mu_i}_{\substack{\text{Concentration}\\ \text{Diffusion}}} + \underbrace{(\phi_i - \omega_i)\nabla p}_{\substack{\text{Pressure}\\ \text{Diffusion}}} \underbrace{- \rho_i \mathbf{g}_i + \omega_i \sum_j \rho_j \mathbf{g}_j}_{\substack{\text{External Force}\\ \text{Diffusion}}} = RT\Big[\underbrace{\sum_{\substack{j=1\\ j\neq i}}^{n} \frac{c_i c_j}{c_T D_{ij}} (v_j - v_i)}_{\text{Drag Term}} + \underbrace{\frac{c_i c_j}{c_T D_{ij}} \left(\frac{D_j^T}{\rho_j} \frac{D_i^T}{\rho_i}\right) \nabla(\ln T)}_{\substack{\text{Thermal}\\ \text{Diffusion}}}\Big] \quad (5.10)$$

Where D_{ij} is the binary Maxwell-Stefan diffusivity, D_i^T is the thermal diffusion, coefficient, c_T is the total molar concentration, c_i is the component molar concentration, and v_i is the component velocity. From this definition, the difference in component velocities term $(v_j - v_i)$ can be thought of as a frictional resistance, with the inter-molecular friction factor equivalent to [116]:

$$K_{ij} = \frac{RT}{c_T D_{ij}} c_i c_j \quad (5.11)$$

However, there is a fundamental issue when applying the S-M framework to hydrogels. Due to the crosslinking the molar concentration of the polymer is undefined as the polymer forms a continuous material. Thus the molar concentration has no physical meaning (the hydrogel is technically one macromolecule). As such, the frictional resistance cannot be determined and with it the S-M diffusion coefficient. In the literature, a number of closures have been proposed to overcome this issue, however many lack physical justification [116]. Attempts include assuming the polymer concentration is negligible (ie. $c_p << c_1$), and using weight fractions, or volume fractions, in lieu of molar concentrations. These however are inconsistent with non-equilibrium thermodynamic postulates, mainly Onsager's reciprocal relation and Gibbs-Duhem equation [116, 131]. This demonstrates the infeasibility of diffusion models to capture the underlining transport phenomena for water in hydrogels, and an alternative approach is needed to succinctly capture the transport phenomena present.

5.3.2 Poroelastic Models

Poroelastic models are a continuum framework formulated using the free energy of swelling, similar to Flory-Rehner [128]. Poroelasticity was first proposed by Biot [132] to describe soil consolidation, but has since been adopted to hydrogels [133, 134]. As water is exchanged with the environment, the resulting material deformation leads to strain within the polymer network and changes in free energy. Starting with thermodynamic equilibrium, this free energy change and the work done by the chemical potential of the solvent describe the thermodynamic response of the material [133]. Though in long timescales hydrogels change volume, at short timescales they are considered incompressible materials. This inherently ties water transport to the gradient in chemical potential within the material. In linear poroelasticity the free energy density due to polymer deformation is assumed to be quadratic in strain following from Hooke's law for linear stress [133].

$$W = G\left[\varepsilon_{ij}\varepsilon_{ij} + \frac{\nu}{1-2\nu}(\varepsilon_{kk})^2\right] \tag{5.12}$$

Where W is the Helmholtz free energy, ε is the strain, ν is Poisson's ratio, and G is the shear modulus.

This formulation is limited to infinitesimal strains, but have shown validity for some system with intermediate deformations. Nonlinear poroelastic models on the other hand are formulation that use nonlinear strain relations for hyper-elastic materials and have been applied to problems with moderate strain however are numerically complex. Building on earlier works like Yoon et al. [133], subsequent poroelastic models incorporate free energy contributions from polymer-solvent mixing in their formulations commonly using Flory-Huggins solution theory. The free energy change of polymer deformation along with the free energy of mixing is analogous to Flory-Rehner theory for thermodynamic equilibrium in swelling polymer gels. Poroelastic models assume the material starts in mechanical equilibrium and is subject to a disturbance.

As observed by Etzold et al. and others, the computation complexity of poroelastic models in more than one dimension makes such models impractical to apply to real system [128]. As such they propose a one-dimensional model for unconstrained swelling of a hydrogel material subject to isotropic elastic stresses. They argue that the key physics of the system in one-dimension can model the behavior of a unconstrained hydrogel without the complexity of nonlinear poroelastic theories. They were able to demonstrate reasonable

agreement between their model and experimental results following parameter fitting. As seen in equation 5.13, their model derivation include a divergence-free phase-averaged material flux ($q_0(t)$).

$$\frac{\partial \phi_p}{\partial t} = \frac{\partial}{\partial z}\left(\phi_p\left(u - q_0(t)\right)\right) \tag{5.13}$$

Where ϕ_p is the polymer fraction and u is the Darcy's flux

In their model some simplifying assumptions were made to ease in the derivation. Building of this previous work, in Chapter 6 this model is generalized to address some of these assumptions. The model will be generalized for unequal densities between water and polymer as this assumption holds for only a few polymer-water systems. Additionally, by explicitly capturing the boundary condition the model can be made more general rather than incorporating a boundary condition directly in the governing equation. A consequence of this is the removal of the divergence free phase-averaged material flux ($q(t)$) from the model. Through experimentation, the model parameters will be explicitly determined without the need for multi parameter fitting. This will allow the model to be applied to the hydrogel system like the hPBR system previously designed.

5.4 Model Parameters

Key Parameter for the model defined in Chapter 6 are defined in the following section. Many of such parameters are in common with the model proposed by Etzold et al. (equation 5.13).

5.4.1 Darcy's Law

When the flow of water through a hydrogel is treated hydrodynamically, the polymer matrix can be thought of as a porous media. Using this paradigm, porous media equations for pressure driven flow can be applied. One such equation is Darcy's law; initially proposed to describe the flow of water through sand, this equation was determined experimentally. However, it has since been derived from the Naiver-Stokes equations. Starting with creeping incompressible flow, Stokes equation is used to derive Darcy's law assuming the viscous resisting force is linear [135]. The model has found applications in hydrology, and reservoir engineering in the petrochemical industry. It can be expressed in the following form:

$$q = -\frac{k}{\mu}\nabla p \tag{5.14}$$

Where k is the permeability of the porous media, μ is the dynamic viscosity, ∇p is the pressure drop across the media, and q is the superficial velocity of the fluid relative to the porous media.

With the creeping flow assumption, Darcy's law is only valid for slow, viscous flow which corresponds to a low Reynolds number ($Re < 1$). At higher Reynolds number inertial effects increasingly become important. Inertial effects can be accounted for with an additional term known as the Forchheimer terms [136]. Scaling analysis will show however, that with the anticipated flow rate in the hydrogel such terms will not be needed. In addition to having steady state laminar flow, Darcy's law, as defined, is only valid for single phase flow, however extensions have been proposed for multi-phase flow (not relevant to the present work). Since the polymer acts as the porous media however, only the single phase formulation is needed. Another requirement of this model is that both the porous media and fluid must be incompressible.

5.4.2 Permeability

Permeability is a measure of a fluids ability to move relative to the porous media [131]. It is related to the porosity (void fraction), and tortuosity (twisting shape of the pore structure). The permeability tensor will be symmetric and positive definite, and for isotropic porous media takes the form $K\mathbf{I}$. We will consider hydrogels to be isotropic. As a hydrogel changes volume, the polymer concentration will vary with time and position. It has been observed that in porous media, pore size has a significant effect on permeability. The hydrogel hydration will influence the effective pore size of the media. As such there is a relationship between polymer volume fraction and permeability. The Kozeny-Carman equation relates pressure drop across a packed bed to its porosity. This type of relationship may also be applicable to other forms of porous media, such as hydrogels. Generally, the Kozeny-Carman equation describes a relationship of the form $K(\phi_p) \propto (1-\phi_p)^3/\phi_p^\beta$. In the literature, $\beta = 2/3$ has been proposed based off the polymer network being a cubic lattice [128]. Assuming $\phi_p << 1$, this relation can be approximated through the following where K_0 is the permeability of the fully swollen gel.

$$K(\phi_p) = K_0 \left(\frac{\phi_{p0}}{\phi_p}\right)^\beta \tag{5.15}$$

5.4.3 Pervadic Pressure (Pore Pressure)

Typically in hydrodynamic problems, an applied pressure gradient is required for flow. However, it has been observed that in hydrogel systems, even without an applied pressure drop, there is still a net flow of water. This would suggest that internal to the gel, there is a gradient of pore pressure driving the flow of water. Gradients in polymer fraction contribute to this pressure gradient through an osmotic process. Conceptually, the pervadic pressure (p) is defined as the pressure measured in a pure solvent connected to some medium (such as a hydrogel) via a semi-permeable membrane [137]. At equilibrium, the relation between ambient and pervadic pressure would be:

$$\mu_w - \mu_{wa} = \nu_w(p - P_a) \tag{5.16}$$

With a one-dimensional model only isotropic stresses will be considered. Within the gel, the total pressure is equal to:

$$P = \pi(\phi) + p_e(\phi) + p \tag{5.17}$$

Where $\pi(\phi)$ is the osmotic pressure due to polymer-water mixing, and $p_e(\phi)$ is the pressure from the polymer elasticity, or the effective pressure of the porous medium. Flory-Huggins theory is commonly used to determine the former with the later based off a polymer chain model. For example, by starting with the isotropic stress balance in the gel, the osmotic pressure, π can be estimated using Flory-Huggins theory in the limit of small polymer volume fractions (van't Hoff's law) [128]:

$$\pi(\phi_p) = \mathscr{A}\phi_p \tag{5.18}$$

Where $\mathscr{A}$ represents some parameter related to the thermodynamics of the system. Similarly, the effective pressure of the porous media, p_e, can be estimated as [128]:

$$p_e(\phi_p) = -k/\phi_p^{2/3} \tag{5.19}$$

In the fully swollen state, no volume fraction gradients exist, as such there is no pressure gradient either. The osmotic pressure will balance the pressure from elasticity. Therefore, it can be shown that at equilibrium the pervadic pressure within the gel pores is equal to the ambient pressure applied to the gel, $P = p$.

5.4.4 Osmotic Modulus

As a hydrogel swells, the polymer chains will stretch leading to mechanical stresses. The pressure within the hydrogel must balance the tension from these polymer chains in order to maintain mechanical stability. The osmotic modulus, π_0, is a measure of the restoring force needed for a change in volume of a gel through swelling deformation. It is similar to elastic modulus; however the deformation is the result of isotropic stresses (osmotic pressure), rather then applied mechanical force to the gel. It is dependent on elastic properties, composition, and interactions with the environment [138, 139]. The reference state is a fully swollen network that is at equilibrium with the solvent environment, and is equal to:

$$\pi_0 = \phi_p \left(\frac{\partial \left(\pi + p_e \right)|_{\phi_p = \phi_{p0}}}{\partial \phi_p} \right) \tag{5.20}$$

Starting with a fully swollen gel, the difference between ambient pressure and the pervadic pressure ($P - p$) can be determined using the osmotic modulus and change in polymer fraction. Thus the water pore pressure can be determined from the polymer volume fraction. This allows for a gradient in pervadic pressure to be measured using the gradient in polymer volume fraction, which is the driving force for water flow inside a hydrogel. Using the expressions for $\pi(\phi_p)$ and $p_e(\phi_p)$ the following relationship is proposed by Etzold et al. [128].

$$P - p = \pi_0 \frac{\phi_p - \phi_{p0}}{\phi_{p0}} \tag{5.21}$$

Chapter 6

Methods: Model Development

To better model the swelling behaviour of the hydrogel substrate with varying humidity conditions a continuum model is proposed to address the deficiencies highlighted in previous works. For our model we consider one-dimensional flow through a hydrogel sheet of thickness $L(t)$. At the $z = 0$ boundary the gel is in contact with a pure liquid water boundary ($z < 0$). As such the left boundary of the domain will be in thermodynamic equilibrium representing a saturated boundary condition. While at $z = L(t)$ the hydrogel will be in contact with air at some humidity RH_{room}. At this boundary it is expected that water will leave the domain by evaporation by way of convective mass transfer into the vapour phase. The continuum consists of two phases, a liquid phase and polymer phase. These phases are assumed to be immiscible and are pure components. In our system PVA is used but this model can be extended to other polymeric hydrogels with suitable modification to the governing equations such as the inclusion of electrostatic interactions for charged polymeric materials. This model aims to capture the spatial and temporal changes in polymer volume fraction $\phi_p(z, t)$ as well as the change in domain size $L(t)$ that results from water entering (swelling) or leaving (shrinking) the domain.

The one-dimensional assumption is used to simplify the model formulation such that stresses tangential to the direction of flow can be omitted. In a three-dimensional setting the hPBR system would expect unidirectional flow due to the frame boundary (zero flux). In reality a nonuniform velocity profile would be expected in a rectangular duct due to a no slip conditions at the boundaries. This would not be captured in a one-dimensional model. However, it is worth noting that fully developed flow would not be expected due to the length of the frame being significantly less than the duct size. This would suggest

that a uniform velocity profile may well approximate flow through the hydrogel slab. The frame would also constrain the movement of the hydrogel as it swells/shrinks in response to environmental changes. By constraining the gel movement, mechanical stresses will be introduced as the hydrogel interacts with the frame, which has not been accounted for in this model. If the volume change is not too great, the mechanical stresses would have minimal impact on the system and therefore can be omitted in the derivation.

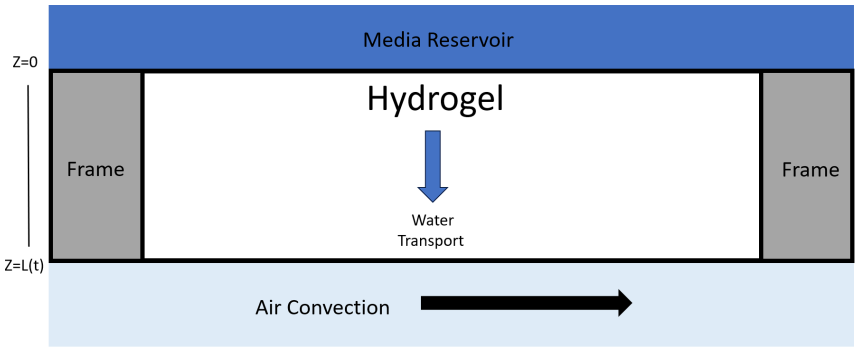

Figure 6.1: Hydrogel Domain Diagram

The main consideration when posing this model is formulating one that will be more general. A more general model would require less parameter tuning, and thus more applicable to real world problems. Developing this model will help garner a deeper understand on how water and nutrient transport may vary with time within the hPBR. This can allow for informed design choices in further prototyping, scale up, or process intensification.

6.1 Governing Equations

Mechanical Energy Balance

Given that water transport through the system is very slow, it can be shown through scaling analysis that viscous forces are negligible in the momentum balance. Given the viscosity of water is $10^{-3} Pa\ s$ and that the expected water flowrate is in the order of $10^{-4}\ m \cdot s^{-1}$ or less, the scaling analysis can be shown using Navier–Stokes equations at steady state in two dimension as:

$$\frac{\partial P}{\partial z} = \mu \frac{\partial^2 v}{\partial x^2} + \rho g$$

$$\frac{P_s}{z_s}\frac{\partial \tilde{P}}{\partial \tilde{z}} = \frac{\mu v_s}{z_s^2}\frac{\partial^2 \tilde{v}}{\partial \tilde{x}^2} + \rho g_s \tilde{g}$$

$$\frac{\partial \tilde{P}}{\partial \tilde{z}} = \frac{\mu v_s}{z_s P_s}\frac{\partial^2 \tilde{v}}{\partial \tilde{x}^2} + \frac{z_s \rho g_s}{P_s}\tilde{g}$$

$$\frac{z_s \rho g_s}{P_s} = 1$$

$$P_s = z_s \rho g_s$$

$$\frac{\partial \tilde{P}}{\partial \tilde{z}} = \frac{\mu v_s}{z_s^2 \rho g_s}\frac{\partial^2 \tilde{v}}{\partial \tilde{x}^2} + \tilde{g}$$

$$\frac{\mu v_s}{z_s^2 \rho g_s} = \frac{(10^{-3} Pa\ s) \cdot (10^{-4} m\ s^{-1})}{(10^{-3} m)^2 \cdot (1000 kg\ m^{-3}) \cdot (9.81 m\ s^{-2})} << 1$$

As such the mechanical energy balance can be simplified to:

$$\frac{\partial P}{\partial z} = \rho g$$

Additionally, if gravity is assumed to be tangential to the direction of flow, the energy balance can be further reduced to the following conservation equation. It will be shown later that the influence of gravity is negligible in our system regardless.

$$\frac{\partial P}{\partial z} = 0$$

Darcy's Flux

As previously defined, Darcy's flux is the volumetric flux of water relative to the motion of the porous media it flows through, in our case the hydrogel. As seen in the mechanical energy balance, we have no external pressure gradient through our system. However, a gradient in pervadic pressure will contribute to flow. Recall that pervadic pressure is the pressure within the gel as measured through a semipermeable membrane, related to the overall system pressure in the following expression.

$$P = \pi(\phi) + p_e(\phi) + p$$

The pervadic pressure is generated through gradients of osmotic pressure within the gel which are caused by spatial variations in concentration as shown in the following equation:

$$\pi_0 = \phi_p \left(\frac{\partial \left(\pi + p_e \right)|_{\phi_p = \phi_{p0}}}{\partial \phi_p} \right)$$

This can thus be applied to Darcy's law to relate water flow to polymer volume fraction:

$$u = \phi_w \left(u_w - u_p \right) = \frac{K}{\eta} \left(\frac{\pi_o}{\phi_{p_0}} \frac{\partial \phi_p}{\partial z} \right) \tag{6.1}$$

$$u_w = \frac{u}{\phi_w} + u_p \tag{6.2}$$

Mass Balance

As the two phases within the domain are perfectly immiscible and there is no mass exchange between phases, the volume within the domain can be divided between the occupying phases; volume fraction of water ϕ_w and volume fraction of polymer ϕ_p.

$$\phi_w + \phi_p = 1 \tag{6.3}$$

In light of this, the differential mass balance for the domain can be represented by the following equations, where the control volume is divided between the two phases, each with their own respective mass conservation equation. The conservation equations are pure advection as the phases are pure components. As the phase do not exchange mass diffusion does not play a role in mass transport according to our formulation.

$$\frac{\partial \rho_p \phi_p}{\partial t} + \frac{\partial}{\partial z}\left(\rho_p \phi_p u_p\right) = 0$$
$$\frac{\partial \rho_w \phi_w}{\partial t} + \frac{\partial}{\partial z}\left(\rho_w \phi_w u_w\right) = 0$$

Where u_p and u_w are the mass average velocities of the polymer and water phases respectively. ρ_p and ρ_w are the phase densities, and t is time. Adding the mass balances of the respective phases leads to the multi-phases mass conservation equation:

$$\frac{\partial \rho_p \phi_p}{\partial t} + \frac{\partial}{\partial z}\left(\rho_p \phi_p u_p\right) + \frac{\partial \rho_w \phi_w}{\partial t} + \frac{\partial}{\partial z}\left(\rho_w \phi_w u_w\right) = 0$$
$$\frac{\partial}{\partial t}\left(\rho_p \phi_p + \rho_w \phi_w\right) = -\frac{\partial}{\partial z}\left(\rho_p \phi_p u_p + \rho_w \phi_w u_w\right)$$

Taking an overall mass balance of the domain, the rate of change of mass within the domain should equal to the rate of accumulation (mass entering and leaving). It can be shown that the change in mass of the whole domain is equal to the flux at the system boundaries, where n is convective mass transfer with the surroundings to the system.

$$\frac{d}{dt}\left(\int_0^{L(t)} \rho_p \phi_p + \rho_w \phi_w \; dz\right) = n|_0 - n|_{L(t)}$$

As highlighted in the overall mass balance of the domain, the integral is dependent on the length of the domain. This will change with time due to the conservation of polymer within the domain, since water is the only mobile species present. This dependence represents a moving boundary in the problem. This boundary change can be dealt with by applying Leibniz rule to capture the changing boundary analytically. Leibniz rule is expressed as:

$$\frac{d}{dt}\left(\int_{a(t)}^{b(t)} f(t,x)dx\right) = f(t,b(t)) \cdot \frac{d}{dt}\big(b(t)\big) - f(t,a(t)) \cdot \frac{d}{dt}\big(a(t)\big) + \int_{a(t)}^{b(t)} \frac{\partial}{\partial t} f(x,t)dt$$

In the domain only the right boundary is moving, and the left one fixed (L=0). The right boundary is fixed since it is in thermodynamic equilibrium and thus always fully saturated $\phi_p|_{z=0} = \phi_{p0}$. Without a change in water concentration at the boundary the polymer fraction cannot change. As such $u_p(t, z = 0) = 0$. Applying Leibniz rule to the left-hand side of the overall mass balance yields.

$$\int_0^{L(t)} \frac{d}{dt}(\ \rho_p\phi_p + \rho_w\phi_w)\ dz + (\rho_p\phi_p + \rho_w\phi_w)\,\frac{dL}{dt} = n|_0 - n|_{L(t)}$$

Substituting in the expression previously found for the temporal change of mass in the control volume (multi-phase mass conservation equation) and applying divergence theorem in one dimension ($\int \nabla \cdot f dz = \int n \cdot f dz$) yields:

$$\int_0^{L(t)} -\frac{\partial}{\partial z}\left(\rho_p\phi_{_p}u_p + \rho_w\phi_w u_w\right) dz + (\rho_p\phi_p + \rho_w\phi_w)\,\frac{dL}{dt} = n|_0 - n|_{L(t)}$$

$$\left(\rho_p\phi_{_p}u_p + \rho_w\phi_w u_w\right)\Big|_0 - \left(\rho_p\phi_{_p}u_p + \rho_w\phi_w u_w\right)\Big|_{L(t)} + (\rho_p\phi_p + \rho_w\phi_w)|_{L(t)}\,\frac{dL}{dt} = n|_0 - n|_{L(t)}$$

Noting that $u_p(z = 0) = 0$ as previously mentioned, and that the saturated boundary condition also requires that the flux into the boundary from outside the domain is equal to the flux away from the boundary within the domain $n|_0 = \rho_{_w}\phi_w u_w$. The change in length of the hydrogel can be determined as:

$$\frac{dL}{dt} = \frac{1}{\rho}\left(\rho_p\phi_p u_p + \rho_w\phi_w u_w - n_w\right)\Big|_{L(t)}$$

$$\rho = \rho_w\phi_w + \rho_p\phi_p \tag{6.4}$$

Where $\rho = \rho_w\phi_w + \rho_p\phi_p$ (the multi-phase mixture density) as evaluated at L(t). Taking into account the relationship between the mass average velocity of water and the volumetric flux determined through Darcy's law. This expression can be further simplified to:

$$\frac{dL}{dt} = \left(u_p + \frac{1}{\rho}\left(\rho_w u - n_w\right)\right)\Big|_{L(t)}$$

The flux out of the domain is the convective mass flux (n_w) which can be determined empirically or experimentally. Unlike the left boundary, which is at thermodynamic equilibrium where the flux on either size of the boundary are equal, the flux within the domain to the boundary at $z = L$ is not balanced with the flux out of the domain, which leads to the moving boundary. The flux of water to the boundary from within the domain is $\rho_w u_w$. At the boundary the Darcy's flux, which is the relative motion of water to the polymer matrix, is equal to the convective mass transfer out of the domain, $u = \frac{n_w}{\rho_w}$. The Darcy's flux relates the water velocity to the motion of the polymer as the domain changes size. As such:

$$\frac{dL}{dt} = u_p|_{L(t)} \tag{6.5}$$

This equation implies that the domain changes size at the same rate as the polymer velocity at the gels' surface. As such, any change in concentration within the domain will directly lead to a change in domain size, and there cannot be independent translation of the boundary without a composition change within the hydrogel. Additionally this implies that the rate of change within the domain is monotonic from the left boundary towards the moving boundary, with the moving boundary having the greatest relative velocity.

Differential Mass Balance

Next a relationship is needed that can relate the Darcy's flux to the component fluxes within the domain. Starting with the multi-phase mass conservation equation, the Darcy's flux can be introduced in place of the water flux. Simplifying leads to:

$$\frac{\partial \rho}{\partial t} + \frac{\partial}{\partial z}\left(\rho_p \phi_p u_p + \rho_w \phi_w \left(\frac{u}{\phi_w} + u_p\right)\right) = 0$$

$$\frac{\partial \rho}{\partial t} + \frac{\partial}{\partial z}\left(\rho u_p + \rho_w u\right) = 0 \tag{6.6}$$

Polymer Mass Balance

The problem formulation has one degree of freedom remaining. The variable that still requires a constraint is the volume fraction of one of the phases present in the domain. The mass balance of the polymer phases was selected for convenience as the Darcy's flux is in

terms of polymer concentration. As the polymer does not leave the domain, this equation tells us the direction the polymer moves relative to the temporal change in polymer fraction. If the polymer fraction is increasing, the direction of the polymer velocity must be opposite of that of the water meaning the domain is shrinking. Similarly, if the polymer fraction is decreasing, the polymer velocity must be in the same direction as the water velocity and the domain is expanding.

$$\frac{\partial \phi_p}{\partial t} + \frac{\partial}{\partial z}\left(\phi_p u_p\right) = 0 \tag{6.7}$$

Convective Boundary Condition

The last remaining boundary condition is the convective flux out of the domain at $z = L$. As previously stated, the convective flux is related to the Darcy's flux at the edge of the domain (Node N). The driving force for a convective mass transfer boundary is a concentration gradient from a boundary layer close to the interface to a bulk concentration far from it, RH_{room}. The water within the boundary layer can be assumed to be at thermodynamic equilibrium with the interface. Unlike a free surface where the mole fraction can be determined, in a hydrogel the mole fraction of water is undefined since the polymer has infinite molecular weight. As such phase equilibrium relations like Raoult's law are not applicable. However, chemical equilibrium can be used to form an expression in terms of intrinsic and extensive properties of the system. The chemical potential of an ideal water vapour is given by.

$$\mu_w - \mu_w^0 = RT \ln \frac{P_w}{P_w^0} = RT \ln(RH_s)$$

where P_w is the pressure of the water vapour, and P_w^0 is the vapour pressure of the pure component. In the liquid phase, the relationship between pressure and chemical potential is related to the molar volume, ν_w, of the pure component.

$$\mu_w - \mu_{wa} = \nu_w (p - P_a)$$

Where p is the pervadic pressure and P_a is the ambient pressure to the system. Equating these chemical potentials leads to an expression for the difference between pervadic pressure within the hydrogel and the ambient pressure on the system.

$$p - P_a = \frac{RT}{\nu_w} \ln(RH_s)$$

Recall that the total mechanical pressure within the hydrogel can be broken into constitutive components $P = \pi + p_e + p$. As previously defined, the difference in pervadic and ambient pressure can be determined through the osmotic modulus of the material. As such the humidity at the surface of the interface can be determined as:

$$RH_s = \exp\left(-\frac{\nu_w \pi_0}{RT}\left(\frac{\phi_p - \phi_{p0}}{\phi_{p0}}\right)\right) \tag{6.8}$$

And thus the convective flux can be determined to be.

$$u_L = \left.\frac{n_w}{\rho_w}\right|_{z=L} = \frac{h}{\rho_w} c_s \left(RH_s - RH_{room}\right) \tag{6.9}$$

6.2 Problem Formulation

Now that the system has been fully defined, equations 6.1 to 6.7 can be solved simultaneously subject to appropriate boundary conditions. Since there are two partial differential equations with respect to time and one total derivative, three initial conditions must be specified. Three boundary conditions are also required to fully specify the problem. Given the saturated boundary, the left side of the domain has a specified polymer volume fraction that is fixed with time. similarly due to the fixed boundary the polymer velocity must also be 0. On the other size of the domain a convective mass transfer condition constrains the flux out the right side of the domain.

BC1:

$$\left.\phi_p\right|_{z=0} = \phi_{p0}$$

BC2:

$$\left.u_p\right|_{z=0} = 0$$

BC3:

$$u|_{z=L} = \frac{n_w}{\rho_w A} = \frac{h}{\rho_w} c_s \left(\exp\left(-\frac{\pi_0 v_w}{\phi_{p0} RT} (\phi_{pL} - \phi_{p0}) \right) - RH\% \right)$$

IC1:

$$\phi_p|_{t=0} = \phi_{p0}$$

IC2:

$$\rho|_{t=0} = \rho_0$$

IC3:

$$L|_{t=0} = L_0$$

6.3 Simplification for Equal Densities

The general model proposed can be simplified be assuming equivalent densities for the polymer and water phases. This assumption can simplify the numerics of the problem by eliminating the need for Equation 6.4, and removing the temporal derivative from Equation 6.6, thus reducing the size of the problem. With certain hydrogel formulations this assumption is reasonable as some hydrogels have specific gravity close to 1. For example methacrylic acid (MA) has a density of 1.0153 $g\ cm^{-2}$ making gels with essentially neutral buoyancy [140]. For systems that are buoyant, or close to it, it may be appropriate to assume the density is constant in the system. Floating hydrogels are of interest in micro-devices, water purification, tissue engineering and drug delivery application [141, 142, 143]. The new system of equation is:

$$
\begin{aligned}
\phi_w + \phi_p &= 1 \\
\frac{dL}{dt} &= u_p|_{L(t)} \\
u = \phi_w \left(u_w - u_p\right) &= \frac{K}{\eta}\left(\frac{\pi_o}{\phi_{p_0}}\frac{d\phi_p}{dz}\right) \\
u_w &= \frac{u}{\phi_w} + u_p \\
\frac{d}{dz}\left(u_p + u\right) &= 0 \\
\frac{\partial \phi_p}{\partial t} + \frac{\partial}{\partial z}\left(\phi_p u_p\right) &= 0
\end{aligned}
\tag{6.10}
$$

6.4 Model Comparison

Now that the model has been derived for both equal and varying densities between phases, the model can be compared to the formulation proposed in Etzold et al. Unlike their model, the one we propose can be generalized to varying densities between the liquid and polymer phases, this generality can make the model more applicable to a greater variety of polymeric systems. Additionally, using the differential overall mass balance and the polymer mass balance, a divergence free phase-average flux term is no longer required. Without the phase-averaged flux the model is no longer limited to having a saturated boundary, and can explicitly capture both boundary conditions.

6.5 Differential Algebraic Equations

As can be seen in both the general derivation, and the special case for equal densities, the final formulation of the model is a differential-algebraic system of equations (DAE). DAE systems are equations where the derivatives of one or more dependent variables are not contained within the system (algebraic variables) preventing the rewriting as a system of explicit ordinary differential equations (ODE). Having $\mathbf{u}$ be a vector containing all dependent variables. The general fully implicit form for a DAE is [144, Ch7]:

$$
F(\mathbf{u}', \mathbf{u}) = 0 \tag{6.11}
$$

When $\partial F/\partial \mathbf{u}'$ is invertible, a system of ODEs for $\mathbf{u}'$ can be found [144, Ch7]. ODEs have the general form:

$$\mathbf{u}' = F(\mathbf{u}, t) \tag{6.12}$$

However, if $\partial F/\partial \mathbf{u}'$ is singular solving DAEs becomes nontrivial. Having algebraic variables leads to a singular Jacobin matrix as is the case with our problem. In the general derivation ϕ_w, u_p, u_w and u are algebraic variables, however through substitution and the fact that $\phi_p + \phi_w = 1$ allows the problem to be formulated to having only one algebraic variable u_p.

Written semi-explicitly, the general form of a DAE is more clearly shown in the following where 6.13a is the differential equations with differential variables $\mathbf{y}$, and equation 6.13b is the algebraic equations with algebraic variables $\mathbf{z}$.

$$\mathbf{y}' = f(\mathbf{y}, \mathbf{z}, t) \tag{6.13a}$$
$$0 = g(\mathbf{y}, \mathbf{z}, t) \tag{6.13b}$$

Should $\partial g/\partial \mathbf{z}$ be invertible, The algebraic equation 6.13b has a solution $\mathbf{z} = G(\mathbf{y}, t)$ which when inserted into equation 6.13a yields an ODE of the form [144, Ch6].

$$\mathbf{y}' = f(\mathbf{y}, G(\mathbf{y}, t), t) \tag{6.14}$$

As the algebraic equation when differentiated once yielded an system of ODEs, the original DAE problem is said to have a differential index of 1. Should $\partial g/\partial \mathbf{z}$ be singular, the problem has a higher differential index. An index 2 system requires 2 differentiations to obtain an ODE system. Here the algebraic variables ($\mathbf{z}$) is missing from the algebraic equation, and has the general form:

$$\mathbf{y}' = f(\mathbf{y}, \mathbf{z}, t) \tag{6.15a}$$
$$0 = g(\mathbf{y}, t) \tag{6.15b}$$

The classical example for DAE index reduction is a simple pendulum in Cartesian coordinates as shown in Figure 6.2. For a pendulum of unit mass and length, the following system of equations describe the pendulum movement with time:

$$x' = u \tag{6.16a}$$
$$y' = v \tag{6.16b}$$
$$u' = -\lambda x \tag{6.16c}$$
$$v' = -\lambda y - g \tag{6.16d}$$
$$0 = x^2 + y^2 - 1 \tag{6.16e}$$

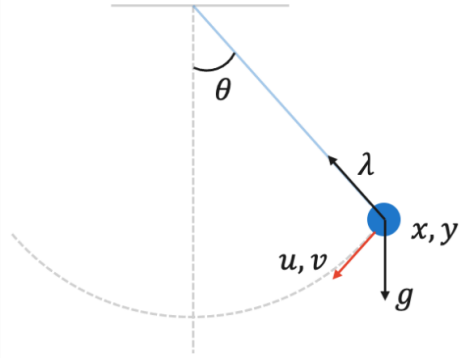

Figure 6.2: Pendulum System [145]

There are 5 variables in this problem $\{x, y, u, v, \lambda\}$, and seemingly 4 degrees of freedom given the constraint 6.16e. However, through index reduction there are two additional hidden constraints that need to be satisfied by the initial conditions. The algebraic constraint (6.16e) is differentiated until the algebraic constraint (λ) has an explicit derivative. As λ is not in the algebraic equation the system is at least index 2. This problem is found to be index 3 as three differentiations are required.

$$0^{th}: \quad 0 = x^2 + y^2 - 1 \qquad [index\ 3] \tag{6.17a}$$
$$1^{st}: \quad 0 = 2xx' + 2yy' \rightarrow 0 = xu + yv \qquad [index\ 2] \tag{6.17b}$$
$$2^{nd}: \quad 0 = u^2 + v^2 - \lambda(x^2 + y^2) - gy \qquad [index\ 1] \tag{6.17c}$$
$$3^{rd}: \quad \lambda' = -3gv \qquad [index\ 0] \tag{6.17d}$$

It can be shown that both formulations presented in this work are index 2 problems. With posing DAE problems it is essential that initial conditions satisfy the algebraic equation, as well as any hidden constraints found through differentiating the algebraic equation. If initial conditions are ill-posed, a solution cannot be found for the problem as the equations are inconsistent [144, Ch7].

As DAE problems can be resolved to ODEs through index reduction, it is natural to think the way to handle such problems would be to differentiate until the system is of index 0, i.e. an ODE system, and solving it numerically with standard ODE methods. However, it is important to note that differentiation may lead to implicit odes that can be challenging to solve. Additionally, numerical solutions from index reduced DAEs tend to be susceptible to numerical drift-off. As the numerical solution advances, the local error measured will depend on the differentiated algebraic restriction. However, the true error will be an integral of the local error since the algebraic equation has been differentiated. As such, the solution will move away from the solution manifold (the topological space defined by the algebraic equation) defined by the original algebraic equation [146].

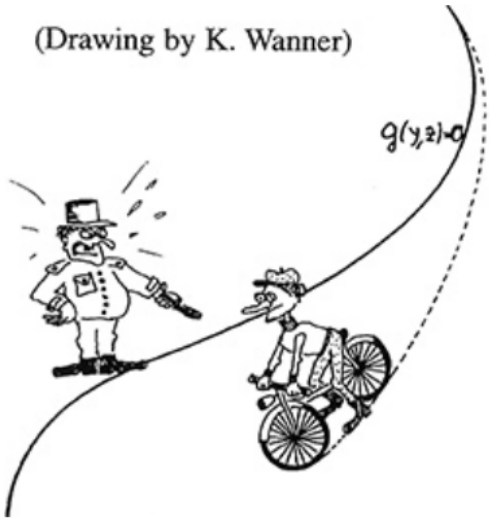

Figure 6.3: Solution manifold of DAE problem [145]

6.6 Non-dimensional Form

A non-dimensional form of the governing equations was formed using the following scaling factors.

$$\tilde{z} = \frac{z}{L_0} \qquad \tilde{\rho} = \frac{\rho}{\rho_p} \qquad \tilde{u} = \frac{\rho_w \tau}{L_0 \rho_p} u \qquad \tilde{t} = \frac{t}{\tau} \qquad \tau = \frac{L_0^2 \rho_p \eta \phi_{p0}^{1/3}}{\rho_w K_0 \pi_0} \qquad \tilde{u_p} = \frac{\tau}{L_0} u_p \qquad \tilde{L} = \frac{L}{L_0}$$

$$\tilde{u} = \phi_p^{-2/3} \left(\frac{\partial \phi}{\partial \tilde{z}} - \alpha \tilde{\rho} \right) \tag{6.18}$$

$$\alpha = \frac{\phi_{p0} \rho_p g L_0}{\pi_0}$$

$$\tilde{\rho} = \frac{\rho_p - \rho_w}{\rho_p} \phi_p + \frac{\rho_w}{\rho_p} \tag{6.19}$$

$$\frac{\partial \tilde{\rho}}{\partial \tilde{t}} = -\frac{\partial}{\partial \tilde{z}} \left(\tilde{\rho} \tilde{u_p} + \tilde{u} \right) \tag{6.20}$$

$$\frac{\partial \phi_p}{\partial \tilde{t}} = -\frac{\partial}{\partial \tilde{z}} \left(\phi_p \tilde{u_p} \right) \tag{6.21}$$

$$\frac{d\tilde{L}}{d\tilde{t}} = \tilde{u_p}|_{\tilde{L}(\tilde{t})} \tag{6.22}$$

The α dimensionless group tells us the relative contribution static pressure has on our system compared to the osmotic pressure. As $\pi_0 \approx 10^3$ and $L_0 \approx 10^{-3}$, $\alpha << 1$ suggesting that the static pressure contribution is negligible in our system.

6.7 Finite Volume Formulation

To solve the model, a discretization scheme is necessary to solve the formulation numerically, as it would be challenging to pose an analytical solution. Finite Volume Method (FVM) is a natural choice to approach this problem, due to the dominant advection term

present in Equation 6.7. In finite volume, the domain is subdivided into cells which can either form a uniform or unstructured mesh. In each cell, volume integrals are applied to the partial differential equation. Using divergence theorem, these volume integrals are converted to surface integrals over the cell, where the fluxes through the cell's surface is evaluated. As these fluxes are defined identically on either side of a surface between adjacent cells, with only the direction of the normal being opposite, this method is inherently conservative helping with numerical stability. Disadvantages of this method however include the difficulty using higher-order methods as compared to other methods such as Finite Element (FEM). Using lower order approximations means that a finer mesh would be required to reach the same level or accuracy as a higher order method, which can potential be more computationally expense to solve. For our approach, a cell centred FVM formulation was used. This places the degrees of freedom at the centre of the cells. In the domain the end nodes are half the width as internal cells allowing the boundary conditions to be expressed in terms of cell centred values. Alternative approaches include not having the boundaries as degrees of freedom, or using a face centred approach to finite volume. The domain's moving boundary complicates the discretization procedure. Our formulation using a uniform mesh. In order to account for the moving boundary, the size of the cells must be adjusted with each time step. As before, Leibniz rule is used to account for the change in size with respect to time. The discretization of the governing equations will be presented in the following section.

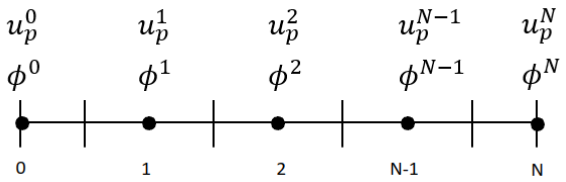

Figure 6.4: Domain Discretization

The step size in the z-direction is equal to $\Delta z = \frac{L}{N}$. Where there is N+1 nodes located at [0, N]. The first node is labelled 0 at the left boundary. The cell boundaries are located at half indices $z_{i\pm1/2} = \left(i \pm \frac{1}{2}\right) \Delta z$. Since the boundary is changing in the problem so does the spatial step size Δz.

$$\frac{d\Delta z}{dt} = \frac{1}{N}\frac{dL}{dt} = \frac{\Delta z}{L}\frac{dL}{dt}$$

$$\frac{dz_{i\pm1/2}}{dt} = \left(i \pm \frac{1}{2}\right)\frac{d\Delta z}{dt} = \frac{z_{i\pm\frac{1}{2}}}{L}\frac{dL}{dt}$$

Conservation of polymer mass

$$\int_v \frac{\partial \phi_p}{\partial t} dV + \int_V \frac{\partial}{\partial z} \left(\phi_p u_p\right) dV = \int_v 0 dV$$

The mass balance is first integrated over the volume of the cell, and divergence theorem applied. Since the problem is taken to be one dimensional, $f_z \equiv \boldsymbol{\nabla} \cdot f$. Therefore:

$$\int_{z_{i-\frac{1}{2}}}^{z_{i+\frac{1}{2}}} \frac{\partial \phi_p}{\partial t} dz = \phi_p u_p \Big|_{z_{i-\frac{1}{2}}}^{z_{i+\frac{1}{2}}}$$

However since the domain is changing size with time, the left side of this equation must be expanded using Leibniz Rule to show the temporal effect not only on the polymer concentration, but also on the volume of the cell.

$$\frac{d}{dt} \int_{z_{i-\frac{1}{2}}}^{z_{i+\frac{1}{2}}} \phi_p dz = \int_{z_{i-\frac{1}{2}}}^{z_{i+\frac{1}{2}}} \frac{\partial \phi_p}{\partial t} dz + \phi_p^{z_{i+\frac{1}{2}}} \frac{dz_{i+\frac{1}{2}}}{dt} - \phi_p^{z_{i-\frac{1}{2}}} \frac{dz_{i-\frac{1}{2}}}{dt}$$

Using these two expressions it can be shown that the change in polymer volume fraction with time as determined by the cell centred value is equal to:

$$\frac{d\phi_p^i}{dt} = -\frac{\phi_p^i}{L}\frac{dL}{dt} + \left(\frac{1}{\Delta z}\left(\phi_p \frac{z}{L}\frac{dL}{dt} - \phi_p u_p\right)\right)\Bigg|_{i-\frac{1}{2}}^{i+\frac{1}{2}} \tag{6.23}$$

Since the left boundary is fully saturated there is no temporal change for Node 0. The polymer concentration will remain at ϕ_0 for all time. It is worth noting that defining the node as such is still consistent with the size change of the cell due to the re-scaling of the domain.

$$\frac{d\phi_{p_0}}{dt} = 0 \tag{6.24}$$

At the other size of the domain (z=L(t)) the equation is modified to the following (node N) since the cell length is half of the other cells, and the degree of freedom is located on the cell boundary.

$$\frac{d\phi_p^N}{dt} = -\frac{\phi_p^N}{L}\frac{dL}{dt} + \left(\frac{2}{\Delta z}\left(\phi_p \frac{z}{L}\frac{dL}{dt} - \phi_p u_p\right)\right)\Bigg|_{N-\frac{1}{2}}^{N} \tag{6.25}$$

Differential Mass Balance

$$\frac{\partial \rho}{\partial t} + \frac{\partial}{\partial z}\left(\rho u_p + \rho_w u\right) = 0$$

Similar to the previous temporal derivative, when discretizing this equation the change in domain size must also be accounted for. The finite volume formulation for this equation is as follows:

At node 0:

$$\frac{d\rho_0}{dt} = 0 \tag{6.26}$$

For internal nodes:

$$\frac{d\rho^i}{dt} = -\frac{\rho^i}{L}\frac{dL}{dt} + \left(\frac{1}{\Delta z}\left(\rho \frac{z}{L}\frac{dL}{dt} - \left(\rho u_p + \rho_w u\right)\right)\right)\Bigg|_{i-\frac{1}{2}}^{i+\frac{1}{2}} \tag{6.27}$$

At z=L the equation is modified to the following (node N) since the cell length is half of the other cells:

$$\frac{d\rho^N}{dt} = -\frac{\rho^N}{L}\frac{dL}{dt} + \left(\frac{2}{\Delta z}\left(\rho \frac{z}{L}\frac{dL}{dt} - \left(\rho u_p + \rho_w u\right)\right)\right)\Bigg|_{N-\frac{1}{2}}^{N} \tag{6.28}$$

The advection term and Darcy's flux are dealt with as follows.

$$(\rho u_p)^{i+\frac{1}{2}} - (\rho u_p)^{i-\frac{1}{2}} = \frac{(\rho u_p)^{i+1} + (\rho u_p)^{i-1}}{2} \tag{6.29}$$

$$u^{1\pm\frac{1}{2}} = \frac{K\left(\phi_p^{i\pm\frac{1}{2}}\right)}{\eta} \frac{\pi_o}{\phi_{p_0}} \frac{d\phi_p^{i\pm\frac{1}{2}}}{dz} \tag{6.30}$$

At node 0 the polymer velocity is fixed.

$$u_p^0 = 0 \tag{6.31}$$

Algebraic Constraints

This system of equation has an algebraic constraint that relates the polymer concentration to the mass concentration spatially in the domain.

$$\rho = \rho_w \phi_w + \rho_p \phi_p \tag{6.32}$$

6.8 Determining Model Parameters

There are three key parameters that need to be determined for this model. The first two are material properties intrinsic to the hydrogel system of interest: permeability (K_0) in the fully swollen state and osmotic modulus (π_0). These two parameters can be estimated using independent experiments separate from the transport experiment. As these parameters are not fitted to the model, should the model be in good agreement with experimental transport results the model can be said to be generalizable. The third parameter relevant to the model is the convective mass transfer coefficient (h) at the gel-air boundary. This parameter is dependent on many characteristics of the system including intensive properties like air flowrate, and surface geometry, and material properties.

6.8.1 Permeability

The permeability in the fully swollen state was estimated experimentally by employing the use of an ultra filtration cell and Darcy's law. By using a fully swollen gel, there will be no pressure gradient generated from gradients in volume fraction. As such the applied pressure in the ultra filtration cell can be used to calculate the permeability according to Darcy's law given the gel thickness (L_0). To prevent mechanical failure of the gel, stainless steel mesh was placed under the hydrogel in the ultra filtration cell.

$$Q = \frac{K_0 A}{\eta L}\Delta P \rightarrow K_0 = \frac{Q\eta L}{A\Delta P}$$

6.8.2 Osmotic Modulus

The osmotic modulus (π_0) relates the volume of a polymeric gel to the osmotic pressure within the material. As such, the osmotic modulus was estimated using an osmotic agent and dialysis tubing (MW cut-off 14,000) [147, 138]. By equilibrating a hydrogel sample with different concentrations of an osmotic agent, the plot of osmotic pressure and logarithmic polymer volume fraction can be used to estimate the hydrogel's osmotic modulus (Equation 5.20). Poly(vinyl) pyrrolidone (M_w 40,000, Sigma-Aldrich, USA) was the osmotic agent of choice due to its high molecular weight and solubility. As no equipment was available to analytically determine the number average molecular weight, the polydispersity reported by others was used to estimate M_n. The polydispersity of the polymer has been shown to be around 2.2 [148]. This value is consistent with the polydispersity expected for batch free radical polymerisation [149]. Using M_n, the osmotic pressure was estimated using the first viral coefficient in the colligative relationship shown in Equation 6.33. The hydrogel was placed inside the dialysis tubing and submerged into the PVP solution.

$$\frac{\pi}{c} = RT\left(\frac{1}{M_n} + \dots\right) \tag{6.33}$$

6.8.3 Convective Mass Transfer Coefficient

The convective mass transfer coefficient can be determined with geometry dependent empirical formulas or multi-physic simulations. However, in this work it was found experimentally using the water transport cell described previously, however without a hydrogel across the liquid surface (Figure 6.5). The rate of mass loss from the device was measured

using an analytical balance from which the transport rate was determined. By testing pure water without a hydrogel, the transfer coefficient from a free surface can be estimated. Assuming the boundary layer over the free surface and the hydrogel are similar, the convective mass transfer coefficient from this experiment may be applied to the hydrogel system.

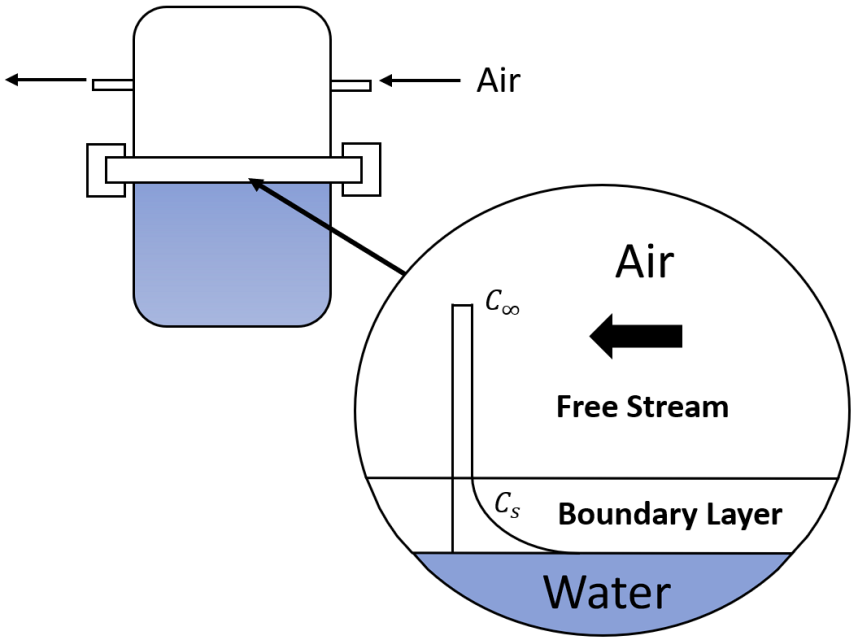

Figure 6.5: Convective mass transfer experiment

Chapter 7

Results: Continuum Model

7.1 Experimental Parameters

Using the procedure described in Section 6.8, the osmotic modulus was determined to be 89.9 kPa. Etzold et al. found $\pi_0 \approx 10^2 Pa$ following parameter tuning, which is 2 orders of magnitude lower than our experimental value [128]. However, our measured value is in agreement with those reported for hyaluronan-based composite hydrogels [147].

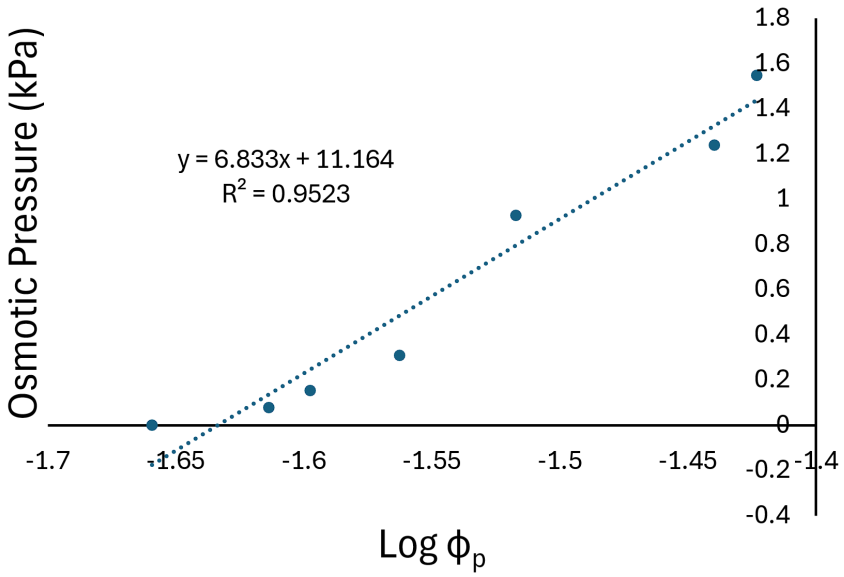

Figure 7.1: Experimental osmotic modulus (π_0)

The permeability in the fully swollen state was experimentally determined to be 9.1×10^{-19} m^2 using the ultra filtration cell. This result was difficult to determine do the mechanical failure of the gel at the high pressures required to achieve flow. The ultra filtration cell had a surface area of $1.53 \times 10^{-3} m^2$. With an applied pressure of 45 psi (310.2 kPa), the volumetric flowrate from a 2 mm thick hydrogel was only $\approx 8mL\ h^{-1}$. Recall that the tensile strength of cPVA was found in literature to be only 563 kPa. As the applied pressure approached this limit, any defects within the hydrogel were increasingly likely to failing. A hydrogel with greater mechanical strength would most likely be less susceptible to tearing compared to the cPVA used in the experiment.

The last parameter experimentally determined was the convective mass transfer coefficient. This value was approximated using the same water transport cell (Figure 3.2) used in the mass transfer experiments. However, instead of placing a hydrogel membrane in the device, the laminar flow was exposed directly to the water's free surface. Analysing the scale data, the convective mass transfer coefficient (h) was found to be 0.0027 $m\ s^{-1}$.

7.2 Water Transport Experimental Data

To validate the results of the model, experimental mass transfer data was collected using the mass transport cell shown in Figure 3.2. Using saturated salt solutions to control humidity (Table 7.1), steady-state transport rates were calculated from the recorded scale data. Due to the high noise to signal ratio with respect to the first derivative of the data, smoothing was performed using a Savitzky-Golay filter (implemented in SciPy) on the first derivative of order 2 using a window size of 13 minutes. This significantly reduced the impact of disturbances on the measured flux rates. The gel thickness was also measured for each trail to determine the dimensionless steady-state thickness for each relative humidity.

Salt Solution	$g/100\ mL$	RH%
KNO_3	300	94
$NaCl$	360	75
$Mg(NO_3)_2$	71	53
$MgCl_2$	54.3	33
KOH	121	9

Table 7.1: Saturated Salt Relative Humidity [150]

7.3 Steady-State Solution

A steady state solution was determined by setting the temporal derivatives to 0 in the DAE system that defines our model. From the polymer conservation equation, it is clear that with no temporal change, the polymer velocity must be 0 everywhere as the saturated boundary condition requires $u_p^0 = 0$. From the phase average mass conservation equation and the fact $u_p = 0$, the Darcy's flux through the material must be constant as $\nabla \cdot u = 0$.

$$\frac{\partial \tilde{u}}{\partial \tilde{z}} = \frac{\partial}{\partial \tilde{z}} \left(\phi_p^{-2/3} \left(\frac{\partial \phi_p}{\partial \tilde{z}} - \alpha \tilde{\rho} \right) \right) \tag{7.1}$$

As $\alpha \approx 0$, expanding the right hand side leads to:

$$\frac{\partial}{\partial \tilde{z}} \left(\phi_p^{-2/3} \frac{\partial \phi}{\partial \tilde{z}} \right) = -\frac{2}{3} \phi_p^{-5/3} \left(\frac{\partial \phi_p}{\partial \tilde{z}} \right)^2 + \phi_p^{-2/3} \frac{\partial^2 \phi_p}{\partial \tilde{z}^2} = 0 \tag{7.2}$$

This is a autonomous differential equation with an analytical solution for ϕ_p

$$\phi_p = \frac{c_1^3 \tilde{z}^3}{27 c_2^2} + \frac{c_1^2 \tilde{z}^2}{3 c_2} + c_1 \tilde{z} + c_2 \tag{7.3}$$

Applying the saturated boundary condition leads to $c_2 = \phi_{p0}$ and c_1 the solution to the second boundary condition solved simultaneously with total polymer conservation. This also allows the steady state thickness of the gel to be determined.

Convective boundary condition:

$$\tilde{u}|_{\tilde{z}=\tilde{L}} = \frac{1}{u_s} \frac{n_w}{\rho_w} = \frac{\rho_w \tau}{L_0 \rho_p} \frac{h}{\rho_w} \left(\exp \left(-\frac{\pi_0 v_w}{RT} \left(\frac{\phi_p - \phi_{p0}}{\phi_{p0}} \right) \right) - RH\% \right) \tag{7.4}$$

Polymer conservation:

$$\int_0^{\tilde{L}} \phi_p d\tilde{z} = \phi_{p0} \tag{7.5}$$

where:

$$\tilde{u}|_{\tilde{z}=\tilde{L}} = \phi_p^{-2/3} \frac{\partial \phi_p}{\partial \tilde{z}} \bigg|_{\tilde{z}=\tilde{L}} \quad ; \quad \frac{\partial \phi_p}{\partial \tilde{z}} = \frac{c_1^3 \tilde{z}^2}{9 \phi_{p0}^2} + \frac{2 c_1^2 \tilde{z}}{3 \phi_{p0}} + c_1$$

7.3.1 Fit to Experimental Data

As model parameters were determined through independent experiments or taken from literature (such as $\beta = 2/3$ and the permeability relationship ($K(\phi_p)$) there was no parameter fitting to the experimental mass transfer data. The steady-state solution presented in this section was solved using SciPy. The polymer conservation integral was evaluated using a QUADPACK routine, while a Least Squares nonlinear optimization was employed to solve the simultaneous equations in residual form. The performance of the model is shown in Figure 7.2. The model had good agreement with experimental results, with most data points close to the model prediction. The dimensionless length of the domain decreases nonlinearly with increasing mass transfer rate out of the hydrogel.

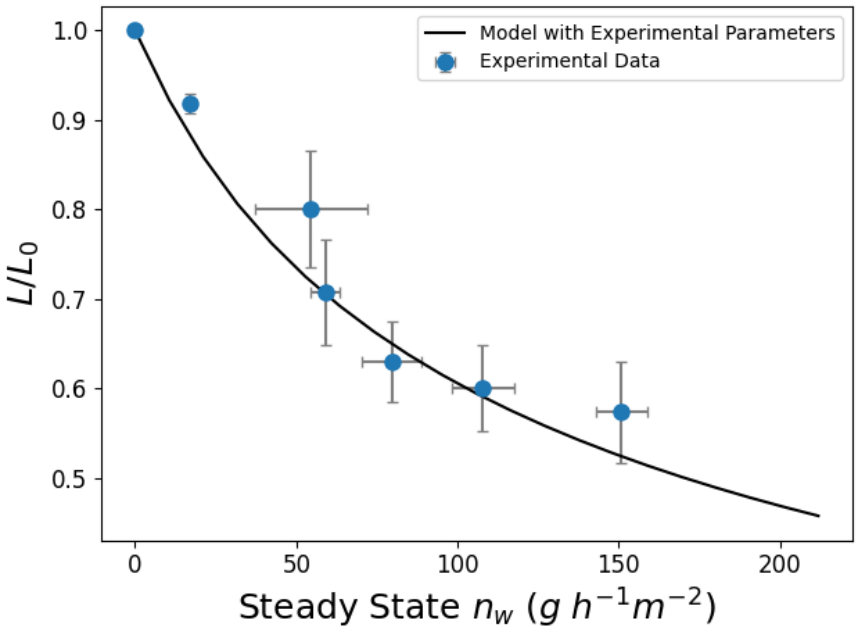

Figure 7.2: Dimensionless thickness vs steady state flux

Figure 7.3 shows the same results, but with respect to the independent variable that was controlled (relative humidity). It is clear that the the model does not closely follow the experimental results. However, this discrepancy can be explained by uncertainty in the relative humidity values. The relative humidity was not directly measure, but was inferred from the saturated salt solution's relative humidities reported in the literature. As such it is unknown if the air leaving the saturated salt solutions were at equilibrium. The gas

steam was first bubbled through distilled water before bubbling through the salt solution. This would explain why the high relative humidity conditions more closely matched the model results, while the low humidity trails were more inaccurate. There may have not been enough contact time with the salt solutions to reduce the humidity to equilibrium.

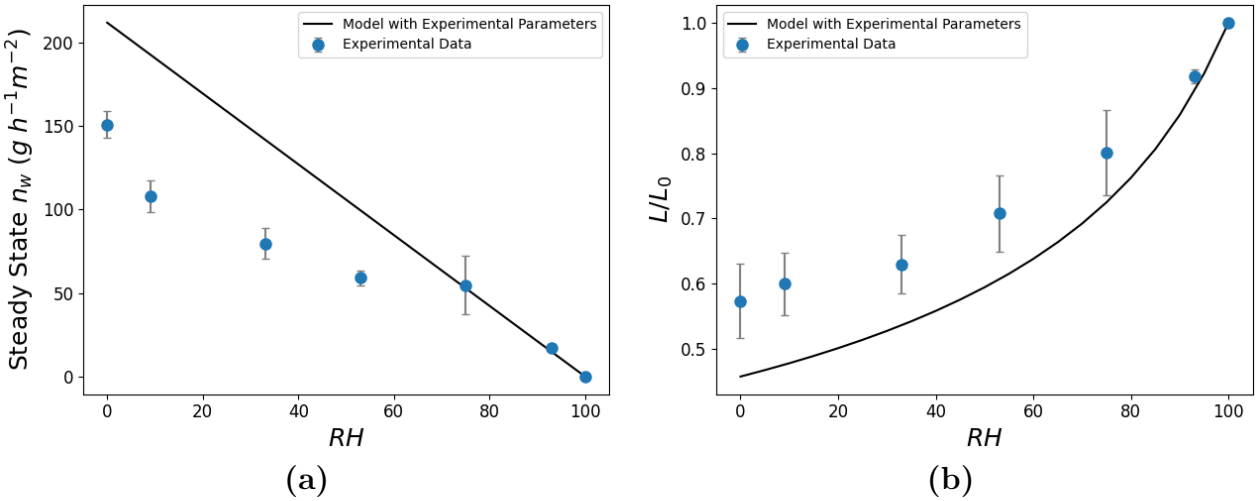

Figure 7.3: **(a)** Steady State flux and **(b)** dimensionless thickness with changing humidity

By adjusting the mass transfer data, the actual humidity of the salt solutions can be estimated given that the mass transport vs thickness plot (Figure 7.2) closely matches the experimental results (which is independent of the actual relative humidity). The model predicts a linear relationship between steady state evaporation and relative humidity. The equation for this line was calculated and used to adjust the humidity values for each data point based off the measured flux. Following this all mass data points will lay on the model line. However, looking at the resulting dimensionless length data vs adjusted relative humidity we can get an idea on the consistency of the model with the experimental data. As seen in Figure 7.4, The dimensionless lengths at the adjusted humidity levels are in close agreement to the model predictions. To verify this result, it would be beneficial to repeat this experiment but with quantitative measures of the air humidity flowing over the hydrogel.

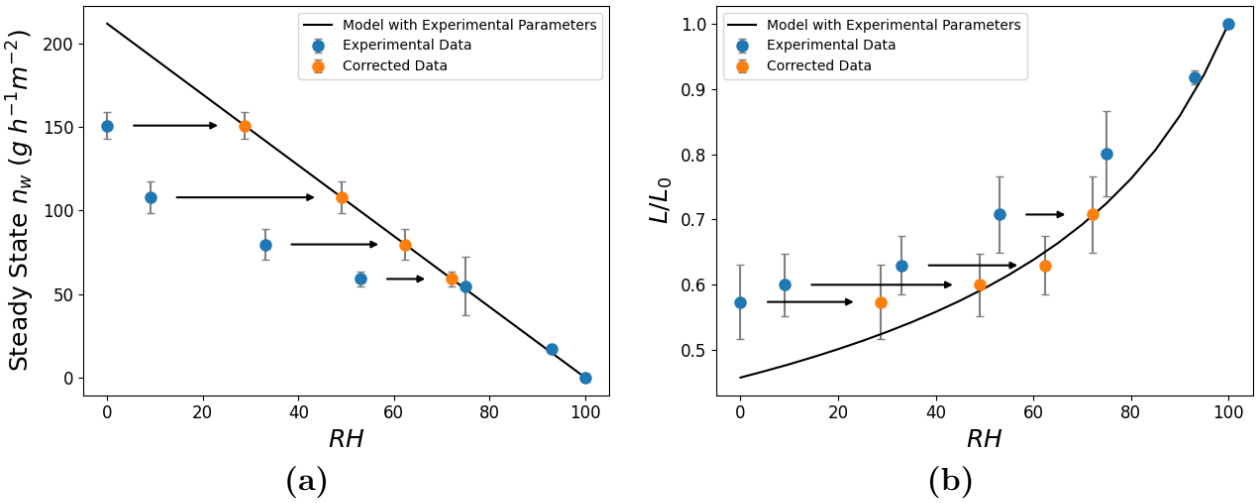

Figure 7.4: **(a)** Steady State flux and **(b)** dimensionless thickness with adjusted humidity

7.4 Transient Solution

As described in Section 6.5, our problem formulation is an index 2 DAE problem. As such, the transient solution was obtained using the Sundial's DAE solver package, and the python wrapper ODES [151, 152, 153]. Within Sundials the IDA (Implicit Differential-Algebraic) solver was selected to solve the IVP DAE problem formulated. The IDA package is a variable-order, variable-coefficient backward differentiation formula (BDF) that solves using a form of newton iteration [154] . When solving semi-explicit index 1 problems, the solver can estimate consistent initial conditions, however, as our problem is higher order consistent initial conditions must be specified to get a converged solution. This posed a challenge with respect to applying the convective boundary condition to the problem. The initial condition on ϕ_p was a uniform profile representing a fully swollen gel. In turn this meant that u_p and u were both zero. However, at the boundary the convective boundary condition makes u_N non-zero showing an inconsistency in the initial conditions. To get the solver to converge at the first time step, the convective boundary was gradually applied instead of being specified at time $t = 0$. This helped to overcome the numerical issues that were previously experienced. Over the first half second, the relative humidity was adjusted from 100% (No flux) to the desired boundary condition using a sinusoidal response. Any relative humidity changes at $t > 0$ were also implemented with a sinusoidal change in condition.

7.4.1 Time Response

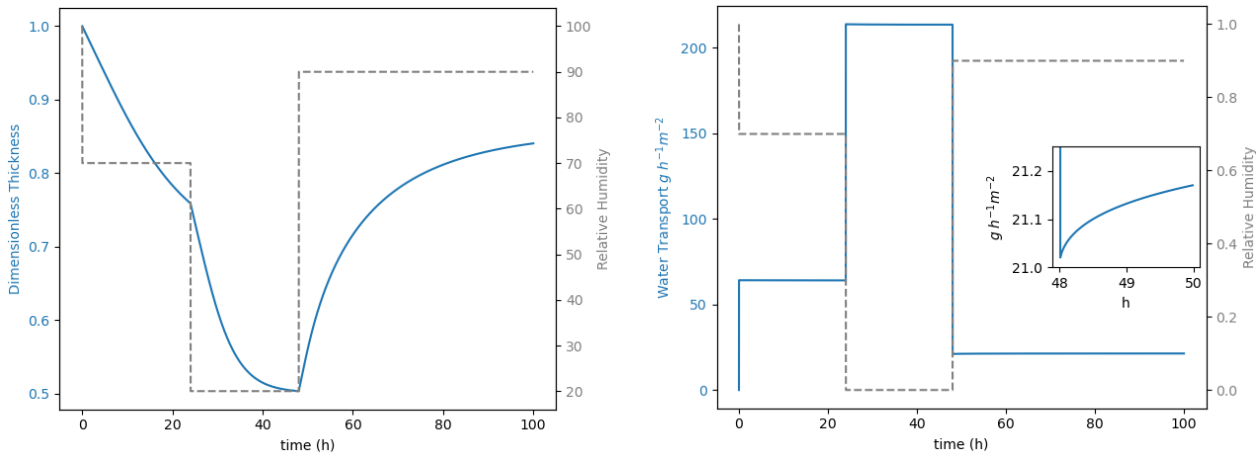

Figure 7.5: **(a)** Dimensionless thickness & **(b)** water transport with changing humidity.

Using the experimentally determined parameters used in the steady-state analysis, the transients response on the hydrogel model was investigated. Figure 7.5a shows how the dimensionless length of the domain changes over time with step changes in relative humidity from 70% to 20% and then to 90% occurring at 24 and 48 hours respectively. As expected, the domain changes size in response to changes in relative humidity. Additionally, the rate of change is related to the magnitude of the flux (relative humidity gradient) the hydrogel is exposed to. An interesting model result is that the convective transport out of the hydrogel is predominantly controlled by the relative humidity of convecting air (driving force for convection) rather then the domain length. The inset in Figure 7.5b shows how the domain change impacts the transport rate. Though the transport rate increases as the gel swells, the step change in relative humidity had a greater impact on the rate of water transport overall.

The most difficult experimental parameter to measure was the permeability in the fully swollen state (K_0). Repeated mechanical failure of the gel lead to high variability in experimental values, and a number of failed trials. As such there was low confidence in the accuracy of this measurement. To understand the model's sensitivity to this parameter,

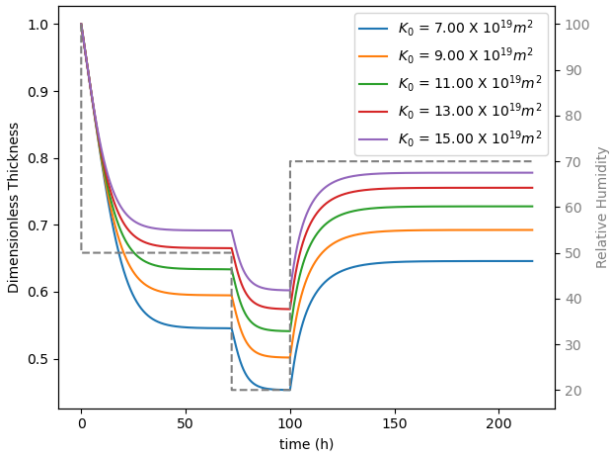

Figure 7.6: Transient response with changing Permeability K_0

Figure 7.6 plots the model results with varying permeability values. Recall that the experimentally determined value was $K_0 = 9 \times 10^{-19}$. As can be seen in the plot, as the permeability increases the steady-state thickness of the gel increase. The time scale of the transient response (τ) also decreases at the permeability of the material increases. This result suggests that the hydrogel's thickness is highly dependent on the permeability of the material. As a one order of magnitude change results in the hydrogel being 40% thicker when the relative humidity is 20%.

7.4.2 Model Comparison

Figure 7.7 shows how the model developed in this paper (both for equal, and unequal densities) compare to the work by Etzold et al. [128]. As can be seen, the results are nearly identical. This suggests that the two models, though derived in different ways, are identical, and that the model presented in this work should simplify to that described in this earlier work. Recall that the work presented by Etzold et al. (Equation 5.13) included a divergence free phase-averaged material flux ($q_0(t)$). It was understood that this value was dependent on the equal density assumption between polymer and water phases. This divergence free term can be expressed as:

$$\frac{\partial}{\partial z}\left(q_0(t)\right) = \frac{\partial}{\partial z}\left(u_p + u\right) = 0 \tag{7.6}$$

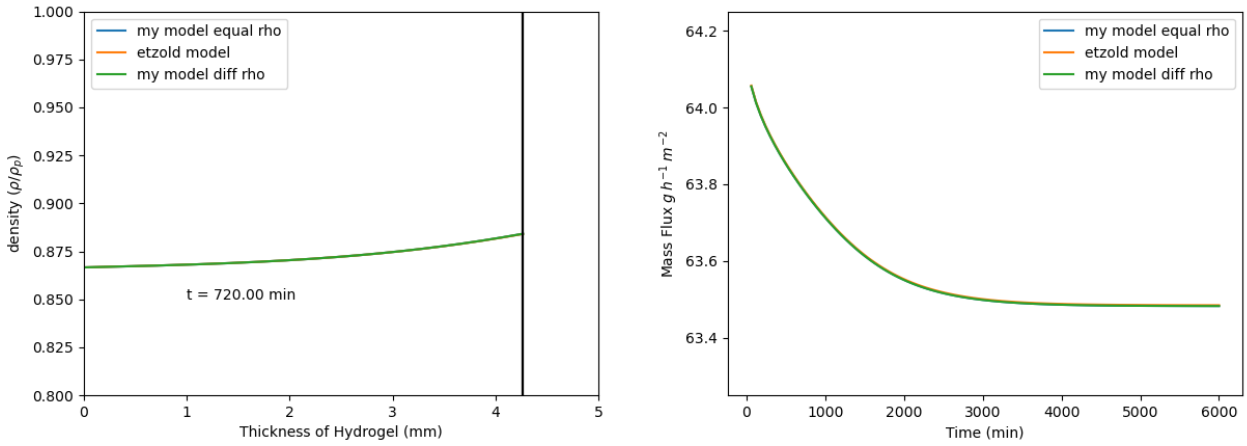

(a) **(b)**

Figure 7.7: **(a)** Spatial variation in density **(b)** transient flux at boundary ($HR = 70\%$)

To qualitatively evaluate the similarity of the models, this divergence term was plotted with time over the length of the domain as well as the Darcy flux (u) and polymer velocity (u_p). As seen in Figure 7.8, the velocity profiles are nearly identical. Additionally, the divergence term was essentially zero for all models over the length of the domain. Near the convective flux boundary, models presented in this thesis had a divergence on the order of 10^{-12}. The velocities however are 5 orders of magnitude greater suggesting this divergence may be a consequence of the numerically scheme and is still essentially zero.

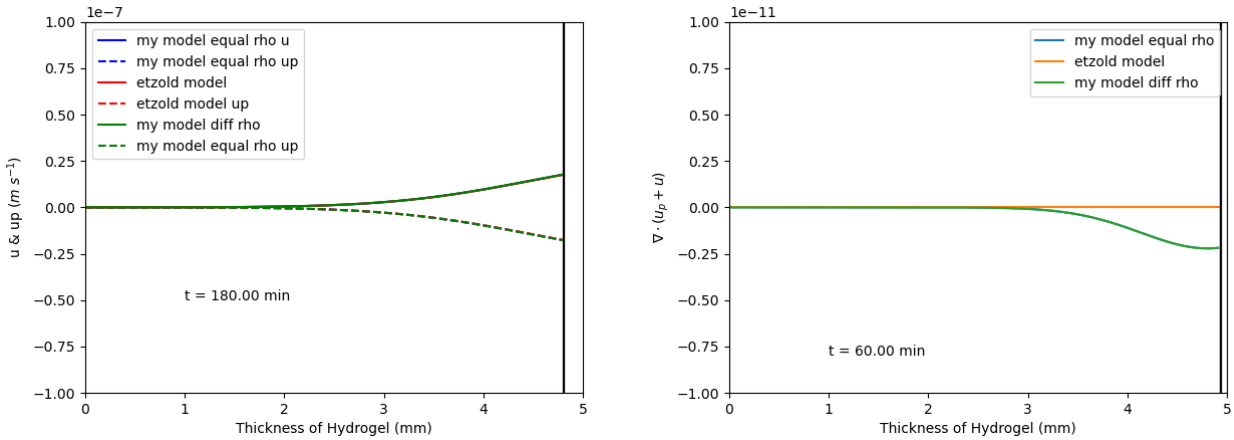

Figure 7.8: **(a)** u_P & u **(b)** divergence term $\nabla \cdot (u + u_p)$

7.4.3 Mathematical Similarity

To investigate further the similarities between these models, it was seen if the divergence free term could be derived from the equations presented in this work. Staring with the differential mass balance (Equation 6.6) it was shown that the equations presented in this work do in fact satisfy the same divergence free phase-average material flux as presented by Etzold et al.

$$\frac{\partial \rho}{\partial t} + \frac{\partial}{\partial z}\left(\rho u_p + \rho_w u\right) = 0$$

Using the fact that the hydrogel consists of binary immersible phases (ie. $\phi_p + \phi_w = 1$), this equation can be rewritten as:

$$(\rho_p - \rho_w)\frac{\partial \phi_p}{\partial t} = -\frac{\partial}{\partial z}\left(\rho_w u + \rho u_p\right)$$

The phase-average density can also be expressed as $\rho = (\rho_p - \rho_w)\phi_p + \rho_w$, which leads to

$$\frac{\partial \phi_p}{\partial t} = -\frac{1}{\rho_p - \rho_w}\frac{\partial}{\partial z}\left(\rho_w u + \left[(\rho_p - \rho_w)\phi_p + \rho_w\right] u_p\right)$$

$$\frac{\partial \phi_p}{\partial t} = -\frac{\partial}{\partial z}\left(\frac{\rho_w}{\rho_p - \rho_w}(u + u_p) + \phi_p u_p\right)$$

Using conservation of polymer mass (Equation 6.7) this expression can then be simplified to:

$$\frac{\partial}{\partial z}(u_p + u) = 0$$

This result shows that the two models are in fact the same, formulated in slightly different ways. The divergence free phase-average material flux ($q_0(t)$) is true even with different densities between polymer and water phases.

7.4.4 Numerical Drift off

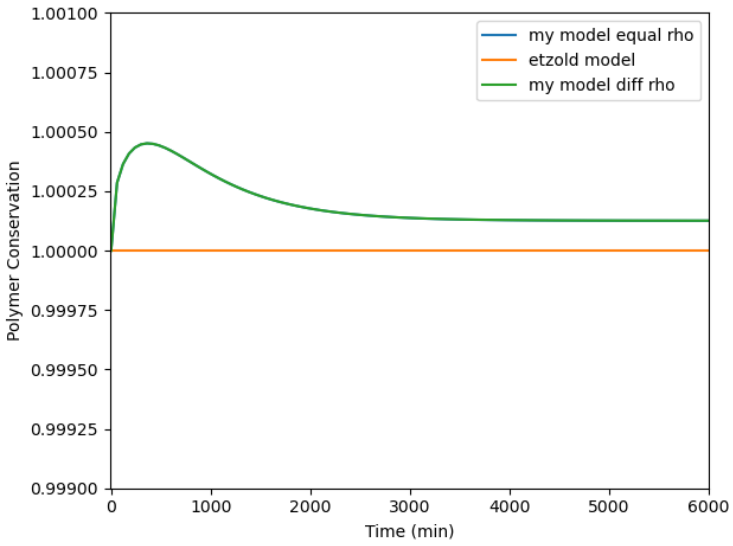

Figure 7.9: Polymer Conservation

As discussed in Section 6.5, numerical drift-off occurs with differentiated algebraic constraints as the true error will be an integral of the local error since the constraint has been differentiated. Invariants may also arise from conserved quantities such as mass, energy,

or momentum if not directly constrained [155]. In the model specified previously, polymer mass conservation is an integral of the local polymer fraction. As such numerical drift-off was experienced in the formulated model as seen in Figure 7.9. However, the amount of drift was less than 0.05% of the hydrogel polymer mass suggesting that it was not very significant. Numerical drift-off is impact by the time-stepping scheme (tolerances on absolute and relative error), as well as the resolution of the mesh used with finer meshes having less drift-off. The ODE model proposed by Etzold et al, solved the polymer conservation directly, as such does not suffer from numerical drift-off as seen in the model proposed here.

7.5 Discussion

The goal of the modelling section was to formulate a more general model as compared to Etzold et al. The deficiencies identified with their model included lack of generality to unequal densities between phases, not explicitly capturing the saturated boundary condition by incorporating it into the governing equation, and the need for multi-parameter fitting. In this modelling section it was shown how independent experimental investigations can be used to estimate model parameters. The resulting model had good agreement with experimental water mass transfer rates through a hydrogel. However, it was also shown that the model formulated here for unequal densities was equivalent to the Etzold model. This was seen through recovering the divergence free phase-average material flux term from the proposed equations. The last modelling objective was to explicitly capture the boundary condition. As compared to Etzold's model, The model presented here allows for a boundary condition on $u_p(z = 0)$ instead of implicitly defining it at zero.

In formulating the model presented in this chapter, there are a number of assumptions that still persist. The thermodynamic relationships that govern the polymer-water mixture were formulated in the limit of small polymer fractions limiting which hydrogel/conditions the model could be applied to. As a hydrogel shrinks, ϕ_p will increase and this condition may not be satisfied. The initial polymer fraction used in the example problem of $\phi_{p0} = 0.2$ may also not satisfy this assumption. Further investigation may be required to verify if the thermodynamic model still holds at higher polymer fractions, or to reformulate the thermodynamic relationship if needed. Ionic effects were also not considered here as PVA is not charged; however they may be relevant for different hydrogel systems and may need to be accounted for in the thermodynamic model.

Part III

Conclusion

Chapter 8

Conclusions

In Part I of this thesis, a new solid-state cultivation system was designed to grow algae using a hydrogel substrate. The design maintained complete phase separation between the liquid media and the gas phase that supplies the CO_2 to the algae growing on the gel's surface. This makes the design gravity independent and thus suitable for extraterrestrial applications such as in regenerative life-support systems to produce food and a breathable environment. Using *C. vulgaris*, the performance of the bioreactor was quantified to investigate the feasibility of the design and to enable design iteration. Over 23 days of growth, a cell density of 71 $g\ m^{-2}$ was achieved using chemically crosslinked poly(vinyl) alcohol as the hydrogel substrate. This was an average productivity of 3.2 $g\ m^{-2}d^{-1}$. Biomass quality analysis suggested that there may be nutrient limited growth as seen in lipid accumulation, which increased from 13.8% to 43.2 % in 8 days, and the decrease in chlorophyll content over the same time period. This finding was supported by nutrient supply analysis as low phosphate and nitrate content was found in the algae paste, though the measurements were below the limit of quantification of the assays.

Part II of this work proposes a hydrogel model to better understand the transport phenomena taking place in the bioreactor. The transport of water is of particular interest as preliminary experimental results of the bioreactor suggested that the hydrogel was susceptible to drying out leading to algal death. The difficulty of modelling water transport through the hydrogel stems from the inherent interdependence between domain size and transport. The swell/shrink behaviour of the hydrogel in response to environmental conditions will change the thickness of the gel as well as the rate of transport though it. Building on the previous work by Etzold et al. [128], a new hydrogel model was proposed for the

transient response of a hydrogel. The modelling results suggest the proposed model simplifies to that of Etzold. However, a difference in the modelling approaches includes the use of experimentally determined parameters in this work. It was shown that three separate experiments can be used to determine system parameters and that the resulting model was in good agreement with experimental transport results. From the transient model, a steady-state solution was also found analytically.

8.1 Modelling Algal Growth

As can be seen in Figure 7.5, the relative humidity had a greater impact on the water transport rate than the change in domain size with time. As such, to simplify the growth model the steady-state solution was used to predict the water transport through the bioreactor. It is expected that algal growth on the hydrogel should add additional resistance for water transport through the system. However, an order of magnitude comparison shows that the additional transport resistance from the algae paste is negligible compared to the resistance through the hydrogel. It has been shown for *C. vulgaris* that the cake resistance (R_c) during filtration is $4.2 \times 10^{12}\ m^{-1}$ [156]. It is expected that a non-compressed algal paste should have an even lower resistance than found during filtration. The estimated filtration resistance for the hydrogel was $4.39 \times 10^{14}\ m^{-1}$ using $R = L/K_0$ where $L = 0.4 \times 10^{-4}\ m$ and $K_0 = 9.1 \times 10^{-19}\ m^2$. As such the biofilm resistance will only be $< 1\%$ of the total resistance to flow, so ignoring the biofilm is a reasonable assumption in terms of water convection through the system.

Using the experimentally determined growth rates in Part I, the water consumption rate was estimated for the biofilm as well. Using cPVA, the biomass density and specific growth rate at 19 days was $43.53\ g\ m^{-2}$ and $1.574 \times 10^{-6}\ s^{-1}$ respectively. With wet biomass being 80% water, the algae paste's water consumption rate is estimated to be $0.986\ g\ m^{-2}h^{-1}$. Therefore the water consumption rate is $< 3\%$ of that of water evaporation from the system (estimated to be between 30 and 50 $g\ m^{-2}h^{-1}$). This also supports the assumption that the impact of the biofilm on water transport can be omitted. As such water consumption can be approximated with the hydrogel's steady-state solution.

$$\phi_p = \frac{c_1^3 \tilde{z}^3}{27\phi_{p0}^2} + \frac{c_1^2 \tilde{z}^2}{3\phi_{p0}} + c_1 \tilde{z} + \phi_{p0} \tag{8.1}$$

Where c_1 is found by solving

$$\tilde{u}|_{\tilde{z}=\tilde{L}} = \frac{1}{u_s}\frac{n_w}{\rho_w} = \frac{\rho_w \tau}{L_0 \rho_p}\frac{h}{\rho_w}\left(\exp\left(-\frac{\pi_0 v_w}{RT}\left(\frac{\phi_p - \phi_{p0}}{\phi_{p0}}\right)\right) - RH\%\right) \tag{8.2}$$

$$\int_0^{\tilde{L}} \phi_p d\tilde{z} = \phi_{p0} \tag{8.3}$$

The importance of this result is that it allows the water content of the hydrogel surface to be estimated and in turn the water activity (a_w). Water activity is a measure of the availability of water for biological reaction [157]. High enough water activity is essential for microorganisms growth. For example, most molds require $a_w > 0.8$. Insight from experimentation and modelling suggests that the relative humidity in the bioreactor needs to be set high enough such that the water activity of the surface is high enough to maintain algal growth. For this reason, the experimental results suggest the relative humidity should be maintained above 80%.

$$a_w = \frac{P}{P_0} = RH_s$$

As seen in the experimental quantification of the hPBR design, solute transport through the hydrogel was a concern. It was suspected that not enough nutrients were being supplied to the algae paste leading to lipid accumulation and chlorophyll degradation in the cells. An alternative explanation for the biomass quality results was photo-inhibition or mechanical stresses from the solid-state cultivation. To better understand the impact nutrient transport has on the system the following model is proposed. Using a continuum framework (Figure 8.1), the hPBR can be broken into two domains, the hydrogel and algae layer. The two domains are coupled through an inlet-outlet boundary condition ($z = L$) where the combined mass flux (n_{s1}) out of the hydrogel enters the algae layer (n_{s2}). On the hydrogel the other boundary ($z = 0$) will be a dirichlet boundary condition at the media reservoir solute concentration (ω_{s0}). The algae surface in contact with the air ($z = L + \delta$, where δ is the gel thickness) will be a no flux boundary condition as the solutes are assumed to be non-volatile. The mass conservation equations for the two domains are:

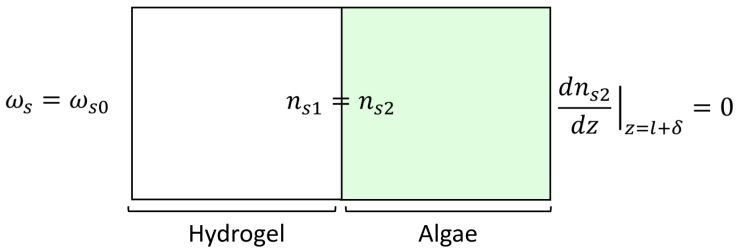

Figure 8.1: Solute model domain

Hydrogel

$$\nabla \cdot n_{s1} = 0$$

$$-\rho(\nabla \cdot \omega_s \mathbf{v}) + \rho \mathscr{D} \nabla^2 \omega_s = 0$$

$$-\mathbf{v}\frac{d\omega_s}{dz} + \mathscr{D}\frac{d^2\omega_s}{dz^2} = 0 \tag{8.4}$$

$$\omega_s(z=0) = \omega_s \quad ; \quad n_{s1}|_{z=L} = n_{s2}|_{z=L}$$

Algae

$$\nabla \cdot n_{2s} - r_s = 0$$

$$-\rho(\nabla \cdot \omega_s \mathbf{v}) + \rho \mathscr{D} \nabla^2 \omega_s - r_s = 0$$

$$-\rho\mathbf{v}\frac{d\omega_s}{dz} + \rho\mathscr{D}\frac{d^2\omega_s}{dz^2} - \frac{\mu_m X}{Y_{X/s}} = 0 \tag{8.5}$$

$$n_{s1}|_{z=L} = n_{s2}|_{z=L} \quad ; \quad \left.\frac{dn_{s2}}{dz}\right|_{z=L+\delta} = 0$$

Applying this model to our experimental data will allow us to gain insight into nutrient availability. The water transport rate previously determined is the mass-average velocity ($\mathbf{v} = 1 \times 10^{-8}\ m\ s^{-1}$). The diffusivity of nitrate is estimated to be $1.5 \times 10^{-9} m^2\ s^{-1}$ in a PVA hydrogel [158]. For simplicity this value is assumed to be constant throughout the material even though it should vary with polymer fraction. The experimental growth rate and biomass density from the growth trials were used. The biomass yield ratio was assumed to be 33 $g\ g_N^{-1}$ though this value depends on a number of factors including nitrate concentration, and photon flux [159]. With these values, the concentration profile of nitrate was estimated throughout the domain. The transport equations were solved using SciPy solve_bvp, and Heaviside functions to apply the reaction term way through the domain. As seen in Figure 8.2, the solute profile inside the hydrogel and algae paste is predicted to be higher then the concentration in the media.

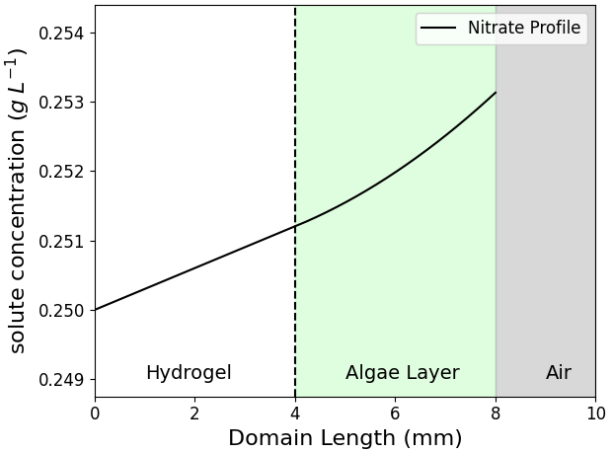

Figure 8.2: Solute concentration profile

Though this is only an estimate, this result suggests there should be sufficient nutrient supply to the microalgae for growth. During the design phase, it was thought that there would be insufficient nutrient supply due to the low diffusivity of the hydrogel. However, the advective transport of nutrients to the boundary and low biomass consumption rate mitigated this issue. This result could be experimentally verified through a tracer experiment to look at the movement of solute in the system. Using a solution of methyl orange, or similar dye, as the 'media' the solute penetration through the hydrogel can be visually inspected. This could help verify the finds of the model or identify issues in its derivation should the colour not permeate the hydrogel fully.

This nutrient model suggests the biomass quality effects are most likely from photo-inhibition effects or mechanical stresses on the algae. As the algae are not in suspension the algae on the reactor's surface are exposed to a much higher photon flux as compared to a liquid culture using the same lighting source. This is due to the shading effect present in liquid cultures. Future trials using varying light intensities may help identify the cause of the biomass quality decrease with time. Shear stresses in liquid cultures have been shown to impact biomass quality and viability [160]. Future work may want to see if a similar effect is observed in solid-state cultivations.

References

[1] Hermann Noordung. *The problem of space travel: The rocket motor*, volume 4026. National Aeronautics and Space Administration, NASA History Office, 1995.

[2] RD MacElroy and James Bredt. Current concepts and future directions of CELSS. *Advances in Space Research*, 4(12):221–229, 1984. Publisher: Elsevier.

[3] James G Goll and BJ Woods. Teaching chemistry using the movie Apollo 13. *Journal of Chemical Education*, 76(4):506, 1999. Publisher: ACS Publications.

[4] Yujia Qiu, Yan Zhou, Yanfen Chang, Xinyue Liang, Hui Zhang, Xiaorui Lin, Ke Qing, Xiaojie Zhou, and Ziqiang Luo. The Effects of Ventilation, Humidity, and Temperature on Bacterial Growth and Bacterial Genera Distribution. *International Journal of Environmental Research and Public Health*, 19(22):15345, 2022. Publisher: Multidisciplinary Digital Publishing Institute.

[5] ECLSS, September 2017. Publication Title: NASA.

[6] Willigert Raatschen and Helmut Preiss. Potential and benefits of closed loop ECLS systems on the ISS. *Acta Astronautica*, 48(5-12):411–419, 2001.

[7] Maya Cooper, Michele Perchonok, and Grace L Douglas. Initial assessment of the nutritional quality of the space food system over three years of ambient storage. *npj Microgravity*, 3(1):17, 2017. Publisher: Nature Publishing Group UK London.

[8] Adeline. How do astronauts eat in space?, October 2021. Publication Title: How Do Astronauts Eat in Space?

[9] Jana Fahrion, Felice Mastroleo, Claude-Gilles Dussap, and Natalie Leys. Use of photobioreactors in regenerative life support systems for human space exploration. *Frontiers in microbiology*, 12:699525, 2021. Publisher: Frontiers Media SA.

[10] Britta Ganzer and Ernst Messerschmid. Integration of an algal photobioreactor into an environmental control and life support system of a space station. *Acta Astronautica*, 65(1-2):248–261, 2009. Publisher: Elsevier.

[11] Christine Escobar and James Nabity. Past, present, and future of closed human life support ecosystems-a review. 47th International Conference on Environmental Systems, 2017.

[12] F Godia, J Albiol, JL Montesinos, J Pérez, N Creus, F Cabello, X Mengual, A Montras, and Ch Lasseur. MELISSA: a loop of interconnected bioreactors to develop life support in space. *Journal of biotechnology*, 99(3):319–330, 2002. Publisher: Elsevier.

[13] Laura Alemany, Enrique Peiro, Carolina Arnau, David Garcia, Laurent Poughon, Jean-François Cornet, Claude-Gilles Dussap, Olivier Gerbi, Brigitte Lamaze, Christophe Lasseur, and others. Continuous controlled long-term operation and modeling of a closed loop connecting an air-lift photobioreactor and an animal compartment for the development of a life support system. *Biochemical Engineering Journal*, 151:107323, 2019. Publisher: Elsevier.

[14] Laurent Poughon, Céline Laroche, Catherine Creuly, Claude-Gilles Dussap, Christel Paille, Christophe Lasseur, Pieter Monsieurs, Wietse Heylen, Ilse Coninx, Felice Mastroleo, and others. Limnospira indica PCC8005 growth in photobioreactor: model and simulation of the ISS and ground experiments. *Life sciences in space research*, 25:53–65, 2020. Publisher: Elsevier.

[15] Jochen Keppler, Stefan Belz, Gisela Detrell, Harald Helisch, Johannes Martin, Norbert Henn, Stefanos Fasoulas, Reinhold Ewald, Oliver Angerer, and Heinz Hartstein. The final configuration of the algae-based ISS experiment PBR@ LSR. 48th International Conference on Environmental Systems, 2018.

[16] Yunhua Zhu, Susanne B Jones, and Daniel B Anderson. Algae farm cost model: Considerations for photobioreactors. Technical report, Pacific Northwest National Lab.(PNNL), Richland, WA (United States), 2018.

[17] Ward Blanken, Maria Cuaresma, René H Wijffels, and Marcel Janssen. Cultivation of microalgae on artificial light comes at a cost. *Algal Research*, 2(4):333–340, 2013. Publisher: Elsevier.

[18] Ryan Davis, Andy Aden, and Philip T Pienkos. Techno-economic analysis of autotrophic microalgae for fuel production. *Applied Energy*, 88(10):3524–3531, 2011. Publisher: Elsevier.

[19] Gisela Detrell. Chlorella vulgaris photobioreactor for oxygen and food production on a moon base—Potential and challenges. *Frontiers in Astronomy and Space Sciences*, 8:700579, 2021. Publisher: Frontiers Media SA.

[20] Mutah Musa, Amar Doshi, Richard Brown, and Thomas J Rainey. Microalgae dewatering for biofuels: A comparative techno-economic assessment using single and two-stage technologies. *Journal of Cleaner Production*, 229:325–336, 2019. Publisher: Elsevier.

[21] Altan Ozkan, Kerry Kinney, Lynn Katz, and Halil Berberoglu. Reduction of water and energy requirement of algae cultivation using an algae biofilm photobioreactor. *Bioresource technology*, 114:542–548, 2012. Publisher: Elsevier.

[22] Weida Zeng, Yun Huang, Ao Xia, Qiang Liao, Keming Chen, Xun Zhu, and Xianqing Zhu. Thermoresponsive surfaces grafted by shrinkable hydrogel poly (N-isopropylacrylamide) for controlling microalgae cells adhesion during biofilm cultivation. *Environmental Science & Technology*, 55(2):1178–1189, 2021. Publisher: ACS Publications.

[23] Tianzhong Liu, Junfeng Wang, Qiang Hu, Pengfei Cheng, Bei Ji, Jinli Liu, Yu Chen, Wei Zhang, Xiaoling Chen, Lin Chen, and others. Attached cultivation technology of microalgae for efficient biomass feedstock production. *Bioresource technology*, 127:216–222, 2013. Publisher: Elsevier.

[24] Zhenyu Zhao, Koenraad Muylaert, and Ivo FJ Vankelecom. Applying membrane technology in microalgae industry: A comprehensive review. *Renewable and Sustainable Energy Reviews*, 172:113041, 2023. Publisher: Elsevier.

[25] Toyoichi Tanaka, Shao-Tang Sun, Yoshitsugu Hirokawa, Seiji Katayama, John Kucera, Yoshiharu Hirose, and Takayuki Amiya. Mechanical instability of gels at the phase transition. *Nature*, 325(6107):796–798, 1987. Publisher: Nature Publishing Group UK London.

[26] Lesley A James, Marios A Ioannidis, and Ioannis Chatzis. Experimentally validated model for the determination of concentration-dependent diffusion of a light hydrocarbon in bitumen. *Energy & fuels*, 26(10):6200–6209, 2012. Publisher: ACS Publications.

[27] Gavin Hoch, Anuj Chauhan, and CJ Radke. Permeability and diffusivity for water transport through hydrogel membranes. *Journal of Membrane Science*, 214(2):199–209, 2003. Publisher: Elsevier.

[28] Libretexts. 2.18: Autotrophs and Heterotrophs, March 2021. Publication Title: Biology LibreTexts.

[29] Mayur M Phukan, Rahul S Chutia, BK Konwar, and R Kataki. Microalgae Chlorella as a potential bio-energy feedstock. *Applied Energy*, 88(10):3307–3312, 2011. Publisher: Elsevier.

[30] Alan Buis. The atmosphere: Getting a handle on carbon dioxide – climate change: Vital signs of the planet, November 2022. Publication Title: NASA.

[31] Kira Schediwy, Andreas Trautmann, Christian Steinweg, and Clemens Posten. Microalgal kinetics—a guideline for photobioreactor design and process development. *Engineering in Life Sciences*, 19(12):830–843, 2019. Publisher: Wiley Online Library.

[32] Alfredo J Garcia III and Jan-Marino Ramirez. Keeping carbon dioxide in check. *Elife*, 6:e27563, 2017. Publisher: eLife Sciences Publications, Ltd.

[33] Xin Wang, Chunbo Hao, Feng Zhang, Chuanping Feng, and Yingnan Yang. Inhibition of the growth of two blue-green algae species (Microsystis aruginosa and Anabaena spiroides) by acidification treatments using carbon dioxide. *Bioresource Technology*, 102(10):5742–5748, 2011. Publisher: Elsevier.

[34] M. N. Editors. Photo bioreactor definition, types, application, advantages, December 2022. Publication Title: Microbiology Note – Online Biology Notes.

[35] Maria del Mar Morales-Amaral, Cintia Gómez-Serrano, F Gabriel Acién, José M Fernández-Sevilla, and E Molina-Grima. Outdoor production of Scenedesmus sp. in thin-layer and raceway reactors using centrate from anaerobic digestion as the sole nutrient source. *Algal Research*, 12:99–108, 2015. Publisher: Elsevier.

[36] Jiří Masojídek and Giuseppe Torzillo. Mass Cultivation of Freshwater Microalgae. In *Encyclopedia of Ecology*, pages 2226–2235. December 2008.

[37] Frederick Frost Blackman. Optima and limiting factors. *Annals of botany*, 19(74):281–295, 1905. Publisher: JSTOR.

[38] Andreas Nikolaou. *Multi-scale modeling of light-limited growth in microalgae production systems*. PhD Thesis, Imperial College London, 2015.

[39] Justus Liebig. Chemistry in its application to agriculture and physiology. 1843. Publisher: Philadelphia: James M. Campbell & Co.

[40] AE Rabe and RJ Benoit. Mean light intensity—a useful concept in correlating growth rates of dense cultures of microalgae. *Biotechnology and Bioengineering*, 4(4):377–390, 1962. Publisher: Wiley Online Library.

[41] Hosni Takache, Jérémy Pruvost, and Jean-François Cornet. Kinetic modeling of the photosynthetic growth of Chlamydomonas reinhardtii in a photobioreactor. *Biotechnology progress*, 28(3):681–692, 2012. Publisher: Wiley Online Library.

[42] Theresa Quaas, Silvia Berteotti, Matteo Ballottari, Kerstin Flieger, Roberto Bassi, Christian Wilhelm, and Reimund Goss. Non-photochemical quenching and xanthophyll cycle activities in six green algal species suggest mechanistic differences in the process of excess energy dissipation. *Journal of plant physiology*, 172:92–103, 2015. Publisher: Elsevier.

[43] Bo-Ping Han. Photosynthesis–irradiance response at physiological level: a mechanistic model. *Journal of theoretical biology*, 213(2):121–127, 2001. Publisher: Elsevier.

[44] RO Megard, DW Tonkyn, and WH Senft. Kinetics of oxygenic photosynthesis in planktonic algae. *Journal of Plankton Research*, 6(2):325–337, 1984. Publisher: Oxford University Press.

[45] Xiaoxi Wu and Jose C Merchuk. A model integrating fluid dynamics in photosynthesis and photoinhibition processes. *Chemical engineering science*, 56(11):3527–3538, 2001. Publisher: Elsevier.

[46] Andrea Bernardi, Giorgio Perin, Eleonora Sforza, Federico Galvanin, Tomas Morosinotto, and Fabrizio Bezzo. An identifiable state model to describe light intensity influence on microalgae growth. *Industrial & engineering chemistry research*, 53(16):6738–6749, 2014. Publisher: ACS Publications.

[47] Joel C Goldman and James J McCarthy. Steady state growth and ammonium uptake of a fast-growing marine diatom 1. *Limnology and oceanography*, 23(4):695–703, 1978. Publisher: Wiley Online Library.

[48] Yinon M Bar-On and Ron Milo. The global mass and average rate of rubisco. *Proceedings of the National Academy of Sciences*, 116(10):4738–4743, 2019. Publisher: National Acad Sciences.

[49] Murray R Badger, T John Andrews, SM Whitney, Martha Ludwig, David C Yellowlees, W Leggat, and G Dean Price. The diversity and coevolution of Rubisco, plastids, pyrenoids, and chloroplast-based CO2-concentrating mechanisms in algae.

Canadian Journal of Botany, 76(6):1052–1071, 1998. Publisher: NRC Research Press Ottawa, Canada.

[50] Anna MJ Kliphuis, Marcel Janssen, Evert J van den End, Dirk E Martens, and René H Wijffels. Light respiration in Chlorella sorokiniana. *Journal of applied phycology*, 23:935–947, 2011. Publisher: Springer.

[51] James Welty, Gregory L Rorrer, and David G Foster. *Fundamentals of momentum, heat, and mass transfer*. John Wiley & Sons, 2020.

[52] Said Abu-Ghosh, Dror Fixler, Zvy Dubinsky, and David Iluz. Flashing light in microalgae biotechnology. *Bioresource technology*, 203:357–363, 2016. Publisher: Elsevier.

[53] Eliane Dalva Godoy Danesi, C de O Rangel-Yagui, JCM De Carvalho, and Sunao Sato. An investigation of effect of replacing nitrate by urea in the growth and production of chlorophyll by Spirulina platensis. *Biomass and Bioenergy*, 23(4):261–269, 2002. Publisher: Elsevier.

[54] Robert W Sterner and James P Grover. Algal growth in warm temperate reservoirs: kinetic examination of nitrogen, temperature, light, and other nutrients. *Water Research*, 32(12):3539–3548, 1998. Publisher: Elsevier.

[55] Pei Sean Goh, Nor Akalili Ahmad, Jun Wei Lim, Yong Yeow Liang, Hooi Siang Kang, Ahmad Fauzi Ismail, and Gangasalam Arthanareeswaran. Microalgae-Enabled Wastewater Remediation and Nutrient Recovery through Membrane Photobioreactors: Recent Achievements and Future Perspective. *Membranes*, 12(11):1094, 2022. Publisher: MDPI.

[56] Shi-Kai Wang, Amanda R Stiles, Chen Guo, and Chun-Zhao Liu. Microalgae cultivation in photobioreactors: An overview of light characteristics. *Engineering in Life Sciences*, 14(6):550–559, 2014. Publisher: Wiley Online Library.

[57] Melinda J Griffiths, Robert P van Hille, and Susan TL Harrison. The effect of nitrogen limitation on lipid productivity and cell composition in Chlorella vulgaris. *Applied microbiology and biotechnology*, 98:2345–2356, 2014. Publisher: Springer.

[58] D Cheng and Q He. Assessment of environmental stresses for enhanced microalgal biofuel production–an overview. Front Energy Res 2: 26, 2014.

[59] Maizatul Azrina Yaakob, Radin Maya Saphira Radin Mohamed, Adel Al-Gheethi, Ravishankar Aswathnarayana Gokare, and Ranga Rao Ambati. Influence of nitrogen and phosphorus on microalgal growth, biomass, lipid, and fatty acid production: an overview. *Cells*, 10(2):393, 2021. Publisher: MDPI.

[60] Yun-Ming Zhang, Hui Chen, Chen-Liu He, and Qiang Wang. Nitrogen starvation induced oxidative stress in an oil-producing green alga Chlorella sorokiniana C3. *PloS one*, 8(7):e69225, 2013. Publisher: Public Library of Science San Francisco, USA.

[61] C. K. Madhubalaji, Sandeep N. Mudaliar, Vikas Singh Chauhan, and R. Sarada. Evaluation of drying methods on nutritional constituents and antioxidant activities of Chlorella vulgaris cultivated in an outdoor open raceway pond. *Journal of Applied Phycology*, 33(3):1419–1434, June 2021.

[62] Ryan Davis, Jennifer Markham, Christopher Kinchin, Nicholas Grundl, Eric C.D. Tan, and David Humbird. Process Design and Economics for the Production of Algal Biomass: Algal Biomass Production in Open Pond Systems and Processing Through Dewatering for Downstream Conversion. Technical Report NREL/TP–5100-64772, 1239893, February 2016.

[63] Prabuddha L. Gupta, Seung-Mok Lee, and Hee-Jeong Choi. A mini review: photobioreactors for large scale algal cultivation. *World Journal of Microbiology and Biotechnology*, 31(9):1409–1417, September 2015.

[64] Bei Wang, Christopher Q. Lan, and Mark Horsman. Closed photobioreactors for production of microalgal biomasses. *Biotechnology Advances*, 30(4):904–912, July 2012.

[65] Tong Li, Marc Strous, and Michael Melkonian. Biofilm-based photobioreactors: their design and improving productivity through efficient supply of dissolved inorganic carbon. *FEMS Microbiology Letters*, 364(24):fnx218, December 2017.

[66] Letícia Rodrigues de Assis, Maria Lúcia Calijuri, Paula Peixoto Assemany, Elisa Couto Berg, Laís Veloso Febroni, and Tereza Angélica Bartolomeu. Evaluation of the performance of different materials to support the attached growth of algal biomass. *Algal Research*, 39:101440, May 2019.

[67] Junfeng Wang, Wentao Cheng, Wen Liu, Hui Wang, Dongcun Zhang, Zhanshan Qiao, Guiyong Jin, and Tianzhong Liu. Field study on attached cultivation of *Arthrospira* (*Spirulina*) with carbon dioxide as carbon source. *Bioresource Technology*, 283:270–276, July 2019.

[68] Hoang-Dung Tran, Thanh-Tri Do, Tuan-Loc Le, Minh-Ly Tran Nguyen, Cong-Hoat Pham, and Michael Melkonian. Cultivation of Haematococcus pluvialis for astaxanthin production on angled bench-scale and large-scale biofilm-based photobioreactors. *Vietnam Journal of Science, Technology and Engineering*, 61(3):61–70, September 2019. Number: 3.

[69] Weida Zeng, Keming Chen, Yun Huang, Ao Xia, Xianqing Zhu, Xun Zhu, and Qiang Liao. Three-dimensional porous biofilm photobioreactor with light-conducting frameworks for high-efficiency microalgal growth. *Algal Research*, 69:102942, January 2023.

[70] Hans C. Bernstein, Maureen Kesaano, Karen Moll, Terence Smith, Robin Gerlach, Ross P. Carlson, Charles D. Miller, Brent M. Peyton, Keith E. Cooksey, Robert D. Gardner, and Ronald C. Sims. Direct measurement and characterization of active photosynthesis zones inside wastewater remediating and biofuel producing microalgal biofilms. *Bioresource Technology*, 156:206–215, March 2014.

[71] Dora Allegra Carbone, Giuseppe Olivieri, Antonino Pollio, Gabriele, and Michael Melkonian. Growth and biomass productivity of Scenedesmus vacuolatus on a twin layer system and a comparison with other types of cultivations. *Applied Microbiology and Biotechnology*, 101(23-24):8321–8329, December 2017. Num Pages: 8321-8329 Place: Heidelberg, Netherlands Publisher: Springer Nature B.V.

[72] Inmaculada González, Natalia Herrero, José Ángel Siles, Arturo F. Chica, M. Ángeles Martín, Carlos García Izquierdo, and José María Gómez. Wastewater nutrient recovery using twin-layer microalgae technology for biofertilizer production. *Water Science and Technology*, 82(6):1044–1061, September 2020. Num Pages: 1044-1061 Place: London, United Kingdom Publisher: IWA Publishing Section: Research Article.

[73] Sahar Saleem, Zeshan Sheikh, Rashid Iftikhar, and Mazhar Iqbal Zafar. Eco-friendly cultivation of microalgae using a horizontal twin layer system for treatment of real solid waste leachate. *Journal of Environmental Management*, 351:119847, February 2024.

[74] Yingying Meng, An Li, Huan Li, Zhensheng Shen, Tian Ma, Jiuyi Liu, Zhongze Zhou, Qian Feng, and Yingqiang Sun. Effect of membrane blocking on attached cultivation of microalgae. *Journal of Cleaner Production*, 284:124695, February 2021.

[75] Thanh-Tri Do, Bich-Huy Tran-Thi, Binh-Nguyen Ong, Tuan-Loc Le, Thanh-Cong Nguyen, Quoc-Dang Quan, Thuong-Chi Le, Dai-Long Tran, Michael Melkonian, and

Hoang-Dung Tran. Effects of red and blue light emitting diodes on biomass and astaxanthin of Haematococcus pluvialis in pilot scale angled twin-layer porous substrate photobioreactors. *Vietnam Journal of Science, Technology and Engineering*, 63(2):81–88, June 2021. Number: 2.

[76] Thanh-Tri Do, Binh-Nguyen Ong, Tuan-Loc Le, Thanh-Cong Nguyen, Bich-Huy Tran-Thi, Bui Thi Thu Hien, Michael Melkonian, and Hoang-Dung Tran. Growth of Haematococcus pluvialis on a Small-Scale Angled Porous Substrate Photobioreactor for Green Stage Biomass. *Applied Sciences*, 11(4):1788, January 2021. Number: 4 Publisher: Multidisciplinary Digital Publishing Institute.

[77] Seung-Hoon Lee, Hee-Mock Oh, Beom-Ho Jo, Sang-A Lee, Sang-Yoon Shin, Hee-Sik Kim, Sang-Ah Lee, and Chi-Yong Ahn. Higher Biomass Productivity of Microalgae in an Attached Growth System, Using Wastewater. *Journal of microbiology and biotechnology*, 24, August 2014.

[78] Lei Zhang, Yong-Zhong Wang, Shengwei Wang, and Ke Ding. Effect of carbon dioxide on biomass and lipid production of *Chlorella pyrenoidosa* in a membrane bioreactor with gas-liquid separation. *Algal Research*, 31:70–76, April 2018.

[79] Junfeng Wang, Wen Liu, and Tianzhong Liu. Biofilm based attached cultivation technology for microalgal biorefineries—A review. *Bioresource Technology*, 244:1245–1253, November 2017.

[80] Shuchao Yin, Junfeng Wang, Lin Chen, and Tianzhong Liu. The water footprint of biofilm cultivation of Haematococcus pluvialis is greatly decreased by using sealed narrow chambers combined with slow aeration rate. *Biotechnology Letters*, 37(9):1819–1827, September 2015.

[81] Code of Federal Regulations Title 21: Food and Drugs, 1984. Published: Electronic Code of Federal Regulations.

[82] Hannah Czech. Algae Cultivation on Hydrogels for Use iin Novel Bioreactor. 2020.

[83] Marie Francene A Cutiongco, Royden KT Choo, Nathaniel JX Shen, Bryan MX Chua, Ervi Sju, Amanda WL Choo, Catherine Le Visage, and Evelyn KF Yim. Composite scaffold of poly (vinyl alcohol) and interfacial polyelectrolyte complexation fibers for controlled biomolecule delivery. *Frontiers in bioengineering and biotechnology*, 3:3, 2015. Publisher: Frontiers Media SA.

[84] Cristina Castro, Robin Zuluaga, Catalina Álvarez, Jean-Luc Putaux, Gloria Caro, Orlando J. Rojas, Iñaki Mondragon, and Piedad Gañán. Bacterial cellulose produced by a new acid-resistant strain of Gluconacetobacter genus. *Carbohydrate Polymers*, 89(4):1033–1037, August 2012.

[85] D S Gorman and R P Levine. Cytochrome f and plastocyanin: their sequence in the photosynthetic electron transport chain of Chlamydomonas reinhardi. *Proceedings of the National Academy of Sciences of the United States of America*, 54(6):1665–1669, December 1965.

[86] H. WAYNE NICHOLS and HAROLD C. BOLD. Trichosarcina polymorpha Gen. et Sp. Nov. *Journal of Phycology*, 1(1):34–38, 1965. Publisher: Blackwell Publishing Ltd.

[87] John F Kopp. *Methods for chemical analysis of water and wastes*. Environmental Monitoring and Support Laboratory, Office of Research and ..., 1979.

[88] G. Bradski. The OpenCV Library. *Dr. Dobb's Journal of Software Tools*, 2000.

[89] Elizabeth J Arar. Method 446.0 In Vitro Determination of Chlorophylls a, b, c+ c and Pheopigments in. 1997.

[90] RJ Porra, WAA Thompson, and PE Kriedemann. Determination of accurate extinction coefficients and simultaneous equations for assaying chlorophylls a and b extracted with four different solvents: verification of the concentration of chlorophyll standards by atomic absorption spectroscopy. *Biochimica et Biophysica Acta (BBA)-Bioenergetics*, 975(3):384–394, 1989. Publisher: Elsevier.

[91] S Van Wychen and LML Laurens. Determination of total lipids as fatty acid methyl esters (FAME) by in situ transesterification. *Contract*, 303(December):275–3000, 2013. Publisher: Citeseer.

[92] Yoshihiro Mori, Hitoshi Tokura, and Masanori Yoshikawa. Properties of hydrogels synthesized by freezing and thawing aqueous polyvinyl alcohol solutions and their applications. *Journal of materials science*, 32:491–496, 1997. Publisher: Springer.

[93] Ana PC Almeida, Joao N Saraiva, Gonçalo Cavaco, Raquel P Portela, Catarina R Leal, Rita G Sobral, and Pedro L Almeida. Crosslinked bacterial cellulose hydrogels for biomedical applications. *European Polymer Journal*, 177:111438, 2022. Publisher: Elsevier.

[94] Manuela Lamberti and Felix Escher. Aluminium foil as a food packaging material in comparison with other materials. *Food Reviews International*, 23(4):407–433, 2007. Publisher: Taylor & Francis.

[95] Lin Liang, Zhongjie Wang, Yi Ding, Yeguang Li, and Xiaobin Wen. Protein reserves elucidate the growth of microalgae under nitrogen deficiency. *Algal Research*, 75:103269, September 2023.

[96] Yangli Ye, Yun Huang, Ao Xia, Qian Fu, Qiang Liao, Weida Zeng, Yaping Zheng, and Xun Zhu. Optimizing culture conditions for heterotrophic-assisted photoautotrophic biofilm growth of *Chlorella vulgaris* to simultaneously improve microalgae biomass and lipid productivity. *Bioresource Technology*, 270:80–87, December 2018.

[97] Cynthia Folsom Murphy and David T. Allen. Energy-Water Nexus for Mass Cultivation of Algae. *Environmental Science & Technology*, 45(13):5861–5868, July 2011. Publisher: American Chemical Society.

[98] Jia Yang, Ming Xu, Xuezhi Zhang, Qiang Hu, Milton Sommerfeld, and Yongsheng Chen. Life-cycle analysis on biodiesel production from microalgae: Water footprint and nutrients balance. *Bioresource Technology*, 102(1):159–165, January 2011.

[99] Wenduo Zhang, Junfeng Wang, Jialin Wang, and Tianzhong Liu. Attached cultivation of *Haematococcus pluvialis* for astaxanthin production. *Bioresource Technology*, 158:329–335, April 2014.

[100] Yun Huang, Wei Xiong, Qiang Liao, Qian Fu, Ao Xia, Xun Zhu, and Yahui Sun. Comparison of *Chlorella vulgaris* biomass productivity cultivated in biofilm and suspension from the aspect of light transmission and microalgae affinity to carbon dioxide. *Bioresource Technology*, 222:367–373, December 2016.

[101] Myung Kwon Cho and Hwa Sung Shin. Mechanotransduction-induced lipid production system with high robustness and controllability for microalgae. *Scientific Reports*, 6(1):32860, 2016. Publisher: Nature Publishing Group UK London.

[102] Qiaoning He, Haijian Yang, and Chunxiang Hu. Effects of temperature and its combination with high light intensity on lipid production of *Monoraphidium dybowskii* Y2 from semi-arid desert areas. *Bioresource Technology*, 265:407–414, October 2018.

[103] Carl Safi, Bachar Zebib, Othmane Merah, Pierre-Yves Pontalier, and Carlos Vaca-Garcia. Morphology, composition, production, processing and applications of

Chlorella vulgaris: A review. *Renewable and Sustainable Energy Reviews*, 35:265–278, 2014. Publisher: Elsevier.

[104] Tan Liu, Zhihui Chen, Yunhua Xiao, Mingmin Yuan, Chenkai Zhou, Gang Liu, Jun Fang, and Bo Yang. Biochemical and morphological changes triggered by nitrogen stress in the oleaginous microalga Chlorella vulgaris. *Microorganisms*, 10(3):566, 2022. Publisher: MDPI.

[105] Veronica da Silva Ferreira and Celso Sant'Anna. Impact of culture conditions on the chlorophyll content of microalgae for biotechnological applications. *World Journal of Microbiology and Biotechnology*, 33(1):20, 2017. Publisher: Springer.

[106] Joseph J Webber and M Grae Worster. A linear-elastic-nonlinear-swelling theory for hydrogels. Part 1. Modelling of super-absorbent gels. *Journal of Fluid Mechanics*, 960:A37, 2023. Publisher: Cambridge University Press.

[107] I Fatt and Thomas K Goldstick. Dynamics of water transport in swelling membranes. *Journal of Colloid Science*, 20(9):962–989, 1965. Publisher: Elsevier.

[108] Enas M Ahmed. Hydrogel: Preparation, characterization, and applications: A review. *Journal of advanced research*, 6(2):105–121, 2015. Publisher: Elsevier.

[109] Yong Qiu and Kinam Park. Environment-sensitive hydrogels for drug delivery. *Advanced drug delivery reviews*, 53(3):321–339, 2001. Publisher: Elsevier.

[110] Maria Bercea, Luiza-Madalina Gradinaru, Simona Morariu, Ioana-Alexandra Plugariu, and Robert Vasile Gradinaru. Tailoring the properties of PVA/HPC/BSA hydrogels for wound dressing applications. *Reactive and Functional Polymers*, 170:105094, 2022. Publisher: Elsevier.

[111] Kang Liu, Ying-Ying Chen, Xue-Qiang Zha, Qiang-Ming Li, Li-Hua Pan, and Jian-Ping Luo. Research progress on polysaccharide/protein hydrogels: Preparation method, functional property and application as delivery systems for bioactive ingredients. *Food Research International*, 147:110542, 2021. Publisher: Elsevier.

[112] Stéphane Lack, Virginie Dulong, Luc Picton, Didier Le Cerf, and Eric Condamine. High-resolution nuclear magnetic resonance spectroscopy studies of polysaccharides crosslinked by sodium trimetaphosphate: a proposal for the reaction mechanism. *Carbohydrate Research*, 342(7):943–953, 2007. Publisher: Elsevier.

[113] Maribel I. Baker, Steven P. Walsh, Zvi Schwartz, and Barbara D. Boyan. A review of polyvinyl alcohol and its uses in cartilage and orthopedic applications. *Journal of Biomedical Materials Research Part B: Applied Biomaterials*, 100B(5):1451–1457, 2012. _eprint: https://onlinelibrary.wiley.com/doi/pdf/10.1002/jbm.b.32694.

[114] Yongping Liang, Jiahui He, and Baolin Guo. Functional Hydrogels as Wound Dressing to Enhance Wound Healing. *ACS Nano*, 15(8):12687–12722, August 2021. Publisher: American Chemical Society.

[115] Jeanie L. Drury and David J. Mooney. Hydrogels for tissue engineering: scaffold design variables and applications. *Biomaterials*, 24(24):4337–4351, November 2003.

[116] Francesco Fornasiero, John M Prausnitz, and Clayton J Radke. Multicomponent Diffusion in Highly Asymmetric Systems. An Extended Maxwell- Stefan Model for Starkly Different-Sized, Segment-Accessible Chain Molecules. *Macromolecules*, 38(4):1364–1370, 2005. Publisher: ACS Publications.

[117] Ali Boushehri, Darren Tang, K. J. Shieh, John Prausnitz, and C. J. Radke. Water transport through soft contact lenses determined in a fan-evaporation cell. *Journal of Membrane Science*, 362(1):529–534, October 2010.

[118] M. P. Lutolf and J. A. Hubbell. Synthetic biomaterials as instructive extracellular microenvironments for morphogenesis in tissue engineering. *Nature Biotechnology*, 23(1):47–55, January 2005. Publisher: Nature Publishing Group.

[119] Philip L Ritger and Nikolaos A Peppas. A simple equation for description of solute release II. Fickian and anomalous release from swellable devices. *Journal of controlled release*, 5(1):37–42, 1987. Publisher: Elsevier.

[120] Pinku Chandra Nath, Shubhankar Debnath, Kandi Sridhar, Baskaran Stephen Inbaraj, Prakash Kumar Nayak, and Minaxi Sharma. A Comprehensive Review of Food Hydrogels: Principles, Formation Mechanisms, Microstructure, and Its Applications. *Gels*, 9(1):1, December 2022.

[121] Ziqian Li, Zishun Liu, Teng Yong Ng, and Pradeep Sharma. The effect of water content on the elastic modulus and fracture energy of hydrogel. *Extreme Mechanics Letters*, 35:100617, 2020. Publisher: Elsevier.

[122] Chad D Markert, Xinyi Guo, Aleksander Skardal, Zhan Wang, Shantaram Bharadwaj, Yuanyuan Zhang, Keith Bonin, and Martin Guthold. Characterizing the microscale elastic modulus of hydrogels for use in regenerative medicine. *Journal of the mechanical behavior of biomedical materials*, 27:115–127, 2013. Publisher: Elsevier.

[123] Yoshihito Osada and Atsushi Matsuda. Shape memory in hydrogels. *Nature*, 376(6537):219–219, 1995. Publisher: Nature Publishing Group UK London.

[124] Alfred Rudin and Phillip Choi. The elements of polymer science and engineering. pages 454–460. Academic press, 2012.

[125] Tizazu Mekonnen. ChE 541 Chapter 2: Thermodynamics of Polymer Solutions and Blends, 2020.

[126] Gang Chen. Thermodynamics of hydrogels for applications in atmospheric water harvesting, evaporation, and desalination. *Physical Chemistry Chemical Physics*, 24(20):12329–12345, 2022. Publisher: Royal Society of Chemistry.

[127] Francesco Fornasiero, Florian Krull, John M. Prausnitz, and Clayton J. Radke. Steady-state diffusion of water through soft-contact-lens materials. *Biomaterials*, 26(28):5704–5716, October 2005.

[128] Merlin A. Etzold, P.F. Linden, and M. Grae Worster. Transpiration through hydrogels. *Journal of Fluid Mechanics*, 925:A8, October 2021.

[129] Gary N Orsborn and Steve G Zantos. Corneal desiccation staining with thin high water content contact lenses. *Eye & Contact Lens*, 14(2):81–85, 1988. Publisher: LWW.

[130] Diego Caccavo. An overview on the mathematical modeling of hydrogels' behavior for drug delivery systems. *International journal of pharmaceutics*, 560:175–190, 2019. Publisher: Elsevier.

[131] R Byron Bird. Transport phenomena. *Appl. Mech. Rev.*, 55(1):R1–R4, 2002.

[132] Maurice A. Biot. General Theory of Three-Dimensional Consolidation. *Journal of Applied Physics*, 12(2):155–164, February 1941.

[133] Jinhwan Yoon, Shengqiang Cai, Zhigang Suo, and Ryan C. Hayward. Poroelastic swelling kinetics of thin hydrogel layers: comparison of theory and experiment. *Soft Matter*, 6(23):6004–6012, November 2010. Publisher: The Royal Society of Chemistry.

[134] Shawn A. Chester and Lallit Anand. A coupled theory of fluid permeation and large deformations for elastomeric materials. *Journal of the Mechanics and Physics of Solids*, 58(11):1879–1906, November 2010.

[135] Stephen Whitaker. Flow in porous media I: A theoretical derivation of Darcy's law. *Transport in porous media*, 1:3–25, 1986. Publisher: Springer.

[136] Debayan Das, Pratibha Biswal, Monisha Roy, and Tanmay Basak. Role of the importance of 'Forchheimer term'for visualization of natural convection in porous enclosures of various shapes. *International Journal of Heat and Mass Transfer*, 97:1044–1068, 2016. Publisher: Elsevier.

[137] Stephen SL Peppin, JAW Elliott, and M Grae Worster. Pressure and relative motion in colloidal suspensions. *Physics of Fluids*, 17(5), 2005. Publisher: AIP Publishing.

[138] Ferenc Horkay and David C Lin. Mapping the local osmotic modulus of polymer gels. *Langmuir*, 25(15):8735–8741, 2009. Publisher: ACS Publications.

[139] Masao Doi. Gel dynamics. *Journal of the Physical Society of Japan*, 78(5):052001, 2009. Publisher: The Physical Society of Japan.

[140] Lei Wang, Yang Liu, Yao Cheng, Xiuguo Cui, Huiqin Lian, Yongri Liang, Fei Chen, Hao Wang, Wenli Guo, Hangquan Li, and others. A bioinspired swimming and walking hydrogel driven by light-controlled local density. *Advanced Science*, 2(6), 2015. Publisher: Wiley-Blackwell.

[141] Nuno M Oliveira, Yu Shrike Zhang, Jie Ju, Ai-Zheng Chen, Yu Chen, Sameer R Sonkusale, Mehmet Remzi Dokmeci, Rui L Reis, Joao F Mano, and Ali Khademhosseini. Hydrophobic hydrogels: toward construction of floating (Bio) microdevices. *Chemistry of Materials*, 28(11):3641–3648, 2016. Publisher: ACS Publications.

[142] Ting Xu, Yuxia Xu, Jiaying Wang, Huijie Lu, Weiping Liu, and Juan Wang. Sustainable self-cleaning evaporator for long-term solar desalination using gradient structure tailored hydrogel. *Chemical Engineering Journal*, 415:128893, 2021. Publisher: Elsevier.

[143] Xing Huang, Linbo Liu, Jie-Li Wang, Mingcheng Bi, Cong Liu, Wenya Liao, Pengfei Wang, Junfeng Liu, Zhanglin Hou, Zhongbin Xu, and others. Designing Self-floating Anisotropic Macroporous Hydrogel by Step Emulsification and Buoyancy-assisted Microfluidics. *Chemical Engineering Journal*, 446:137348, 2022. Publisher: Elsevier.

[144] Gerhard Wanner and Ernst Hairer. *Solving ordinary differential equations II*, volume 375. Springer Berlin Heidelberg New York, 1996.

[145] Jovana Andrejevic and Catherine Ding. Solving differential-algebraic systems of equations (DAEs) - AM 205, 2020.

[146] Per Grove Thomsen and Claus Bendtsen. Numerical solution of differential algebraic equations. *Technical University of Denmark DK-2800 Lyngby Denmark May*, 6, 1999.

[147] Ferenc Horkay, Jules Magda, Mataz Alcoutlabi, Sarah Atzet, and Thomas Zarembinski. Structural, mechanical and osmotic properties of injectable hyaluronan-based composite hydrogels. *Polymer*, 51(19):4424–4430, September 2010.

[148] Rafi Rashid, Natalie Sheng Jie Lim, Stella Min Ling Chee, Si Ning Png, Thorsten Wohland, and Michael Raghunath. Novel Use for Polyvinylpyrrolidone as a Macromolecular Crowder for Enhanced Extracellular Matrix Deposition and Cell Proliferation. *Tissue Engineering Part C: Methods*, 20(12):994–1002, December 2014. Publisher: Mary Ann Liebert, Inc., publishers.

[149] Atsushi Goto and Takeshi Fukuda. Effects of Radical Initiator on Polymerization Rate and Polydispersity in Nitroxide-Controlled Free Radical Polymerization. *Macromolecules*, 30(15):4272–4277, July 1997. Publisher: American Chemical Society.

[150] Engineering ToolBox. Saturated Salt Solutions - Controlling Air Humidity, 2014.

[151] Alan C Hindmarsh, Peter N Brown, Keith E Grant, Steven L Lee, Radu Serban, Dan E Shumaker, and Carol S Woodward. SUNDIALS: Suite of nonlinear and differential/algebraic equation solvers. *ACM Transactions on Mathematical Software (TOMS)*, 31(3):363–396, 2005. Publisher: ACM.

[152] David J Gardner, Daniel R Reynolds, Carol S Woodward, and Cody J Balos. Enabling new flexibility in the SUNDIALS suite of nonlinear and differential/algebraic equation solvers. *ACM Transactions on Mathematical Software (TOMS)*, 2022. Publisher: ACM.

[153] Benny Malengier, Pavol Kišon, James Tocknell, Claas Abert, Florian Bruckner, and Marc-Antonio Bisotti. ODES: a high level interface to ODE and DAE solvers. *Journal of Open Source Software*, 3(22):165, February 2018.

[154] Alan C. Hindmarsh, Radu Serban, Cody J. Balos, David J. Gardner, Daniel R. Reynolds, and Carol S. Woodward. User Documentation for IDA, 2024. Published: urlhttps://sundials.readthedocs.io/en/latest/ida.

[155] Raymond J. Spiteri. Numerical Analysis III (MATH 314), 2013.

[156] Duu-Jong Lee, Gwan-Yu Chen, Yin-Ru Chang, and Kueir-Rarn Lee. Harvesting of chitosan coagulated *Chlorella vulgari*s using cyclic membrane filtration-cleaning. *Journal of the Taiwan Institute of Chemical Engineers*, 43(6):948–952, November 2012.

[157] Province of Manitoba . Water Content and Water Activity: Two Factors That Affect Food Safety.

[158] Matthieu Landreau, HeeJun You, David A. Stahl, and Mari K. H. Winkler. Immobilization of active ammonia-oxidizing archaea in hydrogel beads. *npj Clean Water*, 4(1):1–8, September 2021. Publisher: Nature Publishing Group.

[159] Bingcong Zhang and Kimberly Ogden. Nitrogen balances and impacts on the algae cultivation-extraction-digestion-cultivation process. *Algal Research*, 39:101434, May 2019.

[160] Chinchin Wang and Christopher Q. Lan. Effects of shear stress on microalgae – A review. *Biotechnology Advances*, 36(4):986–1002, July 2018.

APPENDICES

Appendix 1 - hPBR Drawings

CAD drawings for the hPBR system are shown in this section. Drawings for both Design A and B are provided. This repository also contains all files used in the project. For Design A only one component is shown as all modular components had the same basic design. The difference with the spacer was that it was CNC'd from a thicker piece of acrylic then the alumium used to make framing components. Additionally, the Diffusion cell design used in the water transport experiments are given below. The size of the diffusion cell was dictated by the allowable mass on the analytical balance used (100 g).

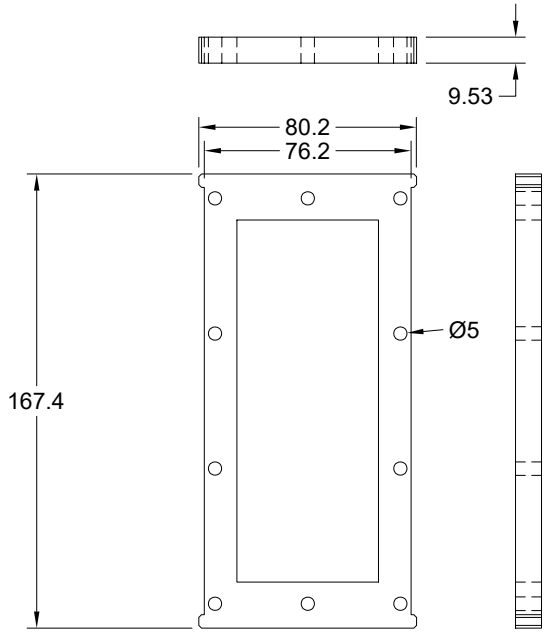

	PROJECT Space Algae Bioreactor				
	TITLE Metal Frame Design A				
APPROVED	SIZE	CODE	DWG NO		REV
CHECKED	A				
DRAWN Nicholas Rasmussen 2024-05-15	SCALE 1:2	WEIGHT		SHEET 1/1	

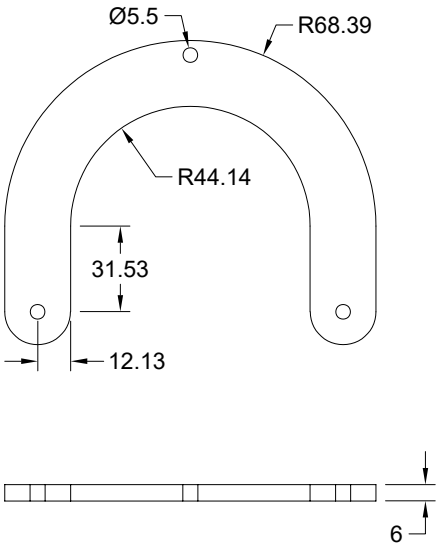

	PROJECT Space Algae Bioreactor				
	TITLE Clamp Reactor B				
APPROVED	SIZE	CODE	DWG NO		REV
CHECKED	A				
DRAWN Nicholas Rasmussen 2024-05-15	SCALE 1:2		WEIGHT	SHEET 1/1	

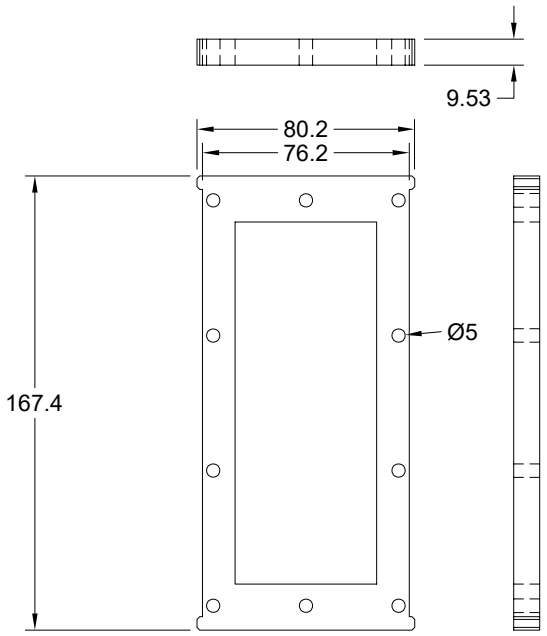

	PROJECT Space Algae Bioreactor				
	TITLE Metal Frame Design A				
APPROVED	SIZE	CODE	DWG NO		REV
CHECKED	A				
DRAWN Nicholas Rasmussen 2024-05-15	SCALE 1:2	WEIGHT		SHEET 1/1	

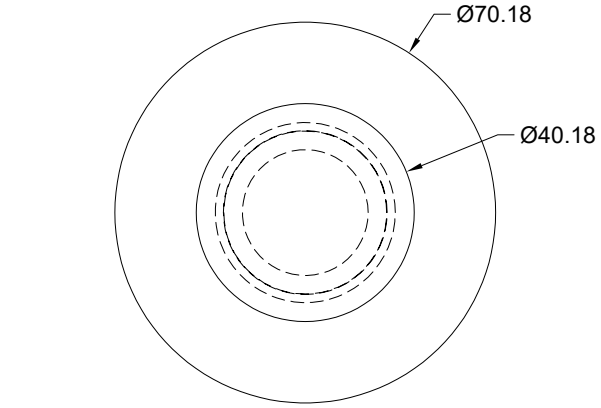

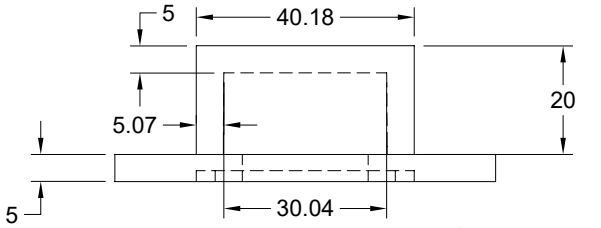

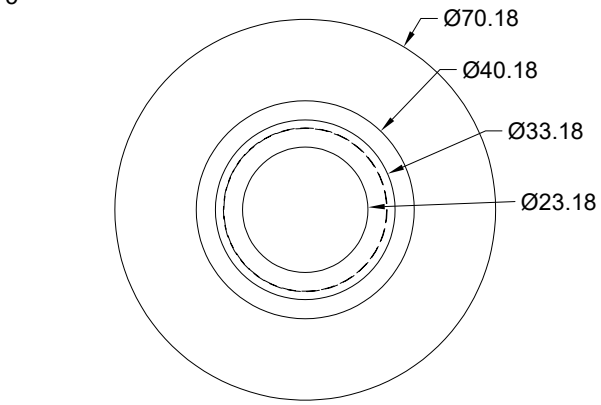

	PROJECT: Space Algae Bioreactor			
	TITLE: Diffusion Cell			
APPROVED	SIZE	CODE	DWG NO	REV
CHECKED	A			
DRAWN Nicholas Rasmussen 2024-05-15	SCALE 1:1	WEIGHT		SHEET 1/1

Appendix 2 - Experimental Results

Date	Trial ID	Day	Mass (g)	Density ($g\ m^{-2}$)
2023-07-28	P-3-1	3	0.0014	0.6113
2023-07-28	P-3-2	3	0.0203	8.8646
2023-07-28	P-6-1	6	0.0469	20.4803
2023-07-28	P-6-2	6	0.0341	14.8908
2024-06-03	P-6-3	6	0.0519	22.6637
2024-06-03	P-6-4	6	0.0508	22.1834
2023-07-28	P-9-1	9	0.0527	23.0131
2023-07-28	P-9-2	9	0.0562	24.5414
2023-07-28	P-12-1	12	0.0729	31.8340
2023-09-11	P-12-2	12	0.0638	27.8602
2023-09-11	P-12-3	12	0.072	31.4410
2024-06-03	P-12-4	12	0.0591	25.8078
2024-06-03	P-12-5	12	0.0929	40.5676
2023-09-11	P-16-1	16	0.1042	45.5021
2023-07-28	P-16-2	16	0.0688	30.0436
2024-02-07	P-16-2	16	0.0733	32.0087
2024-02-07	P-16-3	16	0.0997	43.5371
2023-07-28	P-19-1	19	0.0675	29.4759
2024-02-07	P-19-2	19	0.1052	45.9388
2024-02-07	P-19-3	19	0.1062	46.3755
2024-02-07	P-22-1	22	0.1425	62.2270
2024-02-07	P-22-2	22	0.1013	44.2358
2024-02-07	P-25-1	25	0.0826	36.0698
2024-02-07	P-25-2	25	0.088	38.4279

Table A.1: Growth Study Results cPVA

Day	$g\ m^{-2}$	σ	SE	μ	add error	add value	error prop
0	0.21834061	-	-	-	-	-	-
4	7.1441048	3.922919	1.754383	1.786026	0.43859569	0	0.43859
8	17.6419214	7.132356	4.117868	0.367359	4.47601306	10.4978	0.18075
12	22.8034934	8.991838	4.021272	0.073144	5.75564626	5.1615	0.08332
16	30.8879185	7.487566	4.322948	0.088631	5.90410957	8.0844	0.06658
19	43.5371179	10.99509	6.348019	0.136506	7.68018424	12.6491	0.08505
22	63.1441048	12.47472	8.820961	0.150117	10.8676905	19.6069	0.0860

Table A.2: cPVA Analysis

Date	Trial ID	Day	Mass (g)	Density ($g\ m^{-2}$)
2023-07-28	P-3-1	3	0.0014	0.6113
2023-07-28	P-3-2	3	0.0203	8.8646
2023-07-28	P-6-1	6	0.0469	20.4803
2023-07-28	P-6-2	6	0.0341	14.8908
2024-06-03	P-6-3	6	0.0519	22.6637
2024-06-03	P-6-4	6	0.0508	22.1834
2023-07-28	P-9-1	9	0.0527	23.0131
2023-07-28	P-9-2	9	0.0562	24.5414
2023-07-28	P-12-1	12	0.0729	31.8340
2023-09-11	P-12-2	12	0.0638	27.8602
2023-09-11	P-12-3	12	0.072	31.4410
2024-06-03	P-12-4	12	0.0591	25.8078
2024-06-03	P-12-5	12	0.0929	40.5676
2023-09-11	P-16-1	16	0.1042	45.5021
2023-07-28	P-16-2	16	0.0688	30.0436
2024-02-07	P-16-2	16	0.0733	32.0087
2024-02-07	P-16-3	16	0.0997	43.5371
2023-07-28	P-19-1	19	0.0675	29.4759
2024-02-07	P-19-2	19	0.1052	45.9388
2024-02-07	P-19-3	19	0.1062	46.3755
2024-02-07	P-22-1	22	0.1425	62.2270
2024-02-07	P-22-2	22	0.1013	44.2358
2024-02-07	P-25-1	25	0.0826	36.0698
2024-02-07	P-25-2	25	0.088	38.4279

Table A.3: Growth Study Results pPVA

Day	$g\ m^{-2}$	σ	SE	μ	add error	add value	error prop
3	4.73799	5.8359	4.1266	1.5793	1.3755	0	1.37554
6	20.0545	3.5676	1.7838	1.0775	4.4956	15.3165	0.99039
9	23.7772	1.0807	0.7641	0.0618	1.9406	3.7227	0.03272
12	31.5021	5.6565	2.5296	0.1082	2.6425	7.7248	0.037209
16	37.7729	10.9308	5.4654	0.0663	6.02245	6.27074	0.0639
19	40.5967	9.6333	5.5618	0.02492	7.7977	2.82387	0.0689
22	53.2314	12.7217	8.9956	0.1037	10.5761	12.63464	0.0879
25	37.2489	1.6674	1.1790	0.1000	9.07257	-15.98253	0.05927

Table A.4: pPVA Analysis

day	growth (g)	μ	error	err from add	add value	error propogation
4	0.0006	0.01	0.0006			0.01
8	0.0012	0.25	0.0004	0.000721	0.0006	0.39086798
12	0.00165	0.09375	5E-05	0.000403	0.00045	0.089607555
16	0.00295	0.19697	0.00245	0.002451	0.0013	0.37133739
24	0.0043	0.114407	0.0007	0.002548	0.00135	0.235915507

Table A.5: Flask Culture Analysis

	absorption (wavelength in nm)						mg/L			mg of chlorphyll			mg/g biomass			Average Results			
sample	mg	664	647	630	750	665	Ca	Cb	Cc	ma	mb	mc	ma	mb	mc	Sample	a	b	c
T2-1 4 cPVA	10.3	2.044	0.942	0.562	0.173	2.013	22.32112	7.21642	3.20756	0.033482	0.010825	0.00481134	3.250649	1.050935	0.46712			b	c
T2-2 4 cPVA	6.1	1.255	0.565	0.275	0.01	1.228	13.78165	4.3358	0.35315	0.020672	0.006504	0.000529725	3.38893	1.06618	0.08684				
T2-2 4 cPVA	10	2.36	1.122	0.544	0.049	2.313	25.80292	9.33382	0.87048	0.038704	0.014001	0.00130572	3.870438	1.400073	0.130572	4 cPVA	3.503339	1.172396	0.228178
T2-1 8 cPVA	6.1	1.121	0.489	0.258	0.043	1.101	12.32439	3.51036	0.73769	0.018487	0.005266	0.001106535	3.030588	0.863203	0.181399				
T2-2 8 cPVA	10	0.266	0.205	0.178	0.152	0.266	2.694	2.39329	2.36234	0.004041	0.00359	0.00354351	0.4041	0.358994	0.354351				
T2-3 8 cPVA	10	0.368	0.236	0.189	0.141	0.365	3.84616	2.4621	2.22612	0.005769	0.003693	0.00333918	0.576924	0.369315	0.333918	8 cPVA	1.337204	0.530504	0.289889
T2-2 12 cPVA	10	0.591	0.246	0.124	0.007	0.577	6.52531	1.63441	0.18391	0.009788	0.002452	0.000275865	0.978797	0.245162	0.027587				
T2-1 12 cPVA	10.2	0.401	0.175	0.089	0.015	0.397	4.41115	1.26608	0.18261	0.006617	0.001899	0.000273915	0.648699	0.186188	0.026854				
T2-3 12 cPVA	10.7	0.648	0.299	0.161	0.038	0.635	7.08954	2.34107	0.59316	0.010634	0.003512	0.00088974	0.993861	0.328187	0.083153				
T2-4 12 cPVA	5.5	0.419	0.209	0.119	0.041	0.413	4.54809	1.80356	0.62975	0.006822	0.002705	0.000944625	1.240388	0.49188	0.17175	12 cPVA	0.965436	0.312854	0.077336
T2-1 16 cPVA	9.9	0.424	0.203	0.112	0.043	0.422	4.62218	1.66885	0.49536	0.006933	0.002503	0.00074304	0.70033	0.252856	0.075055				
T2-2 16 cPVA	10.2	0.264	0.135	0.084	0.037	0.26	2.8533	1.18209	0.5928	0.00428	0.001773	0.0008892	0.419603	0.173837	0.087176	16 cPVA	0.559967	0.213346	0.081116
T2-1 19 cPVA	10.3	0.397	0.195	0.113	0.04	0.391	4.31375	1.64456	0.62577	0.006471	0.002467	0.000938655	0.628216	0.239499	0.091132	19 cPVA	0.628216	0.239499	0.091132
T2-1 21 cPVA	10	1.125	0.507	0.256	0.036	1.111	12.34567	3.8725	0.54517	0.018519	0.005809	0.000817755	1.851851	0.580875	0.081776	21 cPVA	1.851851	0.580875	0.081776
T1-2 6 pPVA	10.5	1.51	0.658	0.312	0.005	1.479	16.63058	4.80852	0.12774	0.024946	0.007213	0.00019161	2.375797	0.686931	0.018249				
T1-1 6 pPVA	9.8	1.001	0.45	0.216	0.008	0.98	10.99605	3.45351	0.20465	0.016494	0.00518	0.000306975	1.683069	0.528598	0.031324	6 pPVA	2.029433	0.607765	0.024786
T1-2 12 pPVA	10.6	0.319	0.134	0.069	0.004	0.312	3.51859	0.90231	0.14075	0.005278	0.001353	0.000211125	0.497914	0.127685	0.019917				
T1-1 12 pPVA	10.2	0.762	0.36	0.171	0.006	0.748	8.3385	2.97828	0.18438	0.012508	0.004467	0.00027657	1.22625	0.437982	0.027115	12 pPVA	0.862082	0.282834	0.023516
T1-1 16 pPVA	9.9	0.048	0.02	0.009	-0.002	0.046	0.5308	0.13602	-0.01148	0.000796	0.000204	-0.00001722	0.080424	0.020609	-0.00174				
T1-3 16 pPVA	10.5	0.27	0.118	0.06	0.001	0.267	2.96978	0.85584	0.1235	0.004455	0.001284	0.00018525	0.424254	0.122263	0.017643	15 pPVA	0.252339	0.071436	0.007952

Table A.6: Chlorophyll Analysis

	Date	Trial	reactor	day	g (biomass)	OD	OD corrected	ppm (Nitrate)	mean (pm)	mg(NO3) in sample	mg/g-biomass
	2023-08-23	P-3-1	1	3	0.0014	0.138	0.061	13.93164363		0.020897465	14.92676
	2023-08-23	P-6-1	2	6	0.0469	0.149	0.072	17.1235023		0.025685253	0.54766
	2023-08-23	P-9-1	3	9	0.0527	0.218	0.141	37.14516129	28.29501	0.055717742	1.057263
	2023-08-23	P-12-1	4	12	0.0929	0.245	0.168	44.9797235		0.067469585	0.72626
	2023-08-23		1	12	media	0.3	0.223	60.9390169			
	2023-08-23		2	12	media	0.261	0.184	49.62242704			
	2023-08-23		3	12	media	0.209	0.132	34.53364055			
pPVA	2023-08-23		4	12	media	0.187	0.11	28.1499232			
	2023-08-23	P-3-2	4	3	0.0203	0.193	0.116	29.89093702		0.044836406	2.20869
	2023-08-23	P-6-2	3	6	0.0341	0.148	0.071	16.83333333	17.34113	0.02525	0.740469
	2023-08-23	P-9-2	2	9	0.0562	0.117	0.04	7.838095238		0.011757143	0.209202
	2023-08-23	P-12-2	1	12	0.0938	0.141	0.064	14.80215054		0.022203226	0.236708
	2023-08-23	P-12-4	1	12	0.0191	0.259	0.182	49.04208909		0.073563134	3.851473
	2023-08-23	P-16-2	2	16	0.0288	0.153	0.076	18.28417819	23.79739	0.027426267	0.952301
	2023-08-23	P-18-1	3	18	0.0675	0.104	0.027	4.065898618		0.006098848	0.090353
	2023-08-23	C-4-1	1	4	0.0191	0.099	0.022	2.615053763		0.003922581	0.205371
	2023-08-23	C-8-1	2	8	0.0485	0.191	0.114	29.31059908		0.043965899	0.906513
cPVA	2023-08-23	C-12-1	3	12	0.0584	0.121	0.044	8.998771121		0.013498157	0.231133
	2023-08-23	C-4-2	1	4	0.0298	0.105	0.028	4.356067588		0.006534101	0.219265
	2023-08-23	C-8-2	2	8	0.0511	0.223	0.146	38.59600614		0.057894009	1.132955
	2023-08-23	C-12-2	3	12	0.0622	0.996	0.919	262.8966206		0.394344931	6.339951

Table A.7: Nitrate Analysis

	Date	Trial	reactor	day	g (biomass)	OD	OD corrected	ppm (phosphate)	mean (pm)	mg(PO4) in sample	mg/g-biomass
	2023-07-28	P-3-1	1	3	0.0014	0.126	0.083	1.589415524		0.002384123	1.702945204
	2023-07-28	P-6-1	2	6	0.0469	0.052	0.009	0.134003255		0.000201005	0.004285818
	2023-07-28	P-9-1	3	9	0.0527	0.205	0.162	3.14316646	1.35832	0.00471475	0.089463941
	2023-07-28	P-12-1	4	12	0.0929	0.074	0.031	0.566693389		0.00085004	0.009150055
	2023-07-28		1	12	media	3.776	3.733	73.37664229			
	2023-07-28		2	12	media	3.602	3.559	69.95445669			
	2023-07-28		3	12	media	3.508	3.465	68.10568975			
pPVA	2023-07-28		4	12	media	3.751	3.708	72.88494896			
	2023-07-28	P-3-2	4	3	0.0203	0.067	0.024	0.429019256		0.000643529	0.03170093
	2023-07-28	P-6-2	3	6	0.0341	0.101	0.058	1.09772219	0.596195	0.001646583	0.0482869
	2023-07-28	P-9-2	2	9	0.0562	0.072	0.029	0.527357923		0.000791037	0.014075389
	2023-07-28	P-12-2	1	12	0.0938	0.062	0.019	0.330680589		0.000496021	0.005288069
	2023-07-28	P-12-4	1	12	0.0191	0.079	0.036	0.665032056		0.000997548	0.052227648
	2023-07-28	P-16-2	2	15	0.0288	0.092	0.049	0.92071259	2.212227	0.001381069	0.047953781
	2023-07-28	P-18-1	3	18	0.0675	0.302	0.259	5.050936596		0.007576405	0.112243035
	2023-08-21	C-4-1	1	4	0.0191	0.165	0.122	2.356457125		0.003534686	0.185062078
	2023-08-21	C-8-1	2	8	0.0485	0.12	0.077	1.471409124		0.002207114	0.045507499
cPVA	2023-08-21	C-12-1	3	12	0.0584	0.172	0.129	2.494131259		0.003741197	0.064061591
	2023-08-21	C-4-2	1	4	0.0298	0.099	0.056	1.058386723		0.00158758	0.053274499
	2023-08-21	C-8-2	2	8	0.0511	0.109	0.066	1.255064057		0.001882596	0.036841411
	2023-08-21	C-12-2	3	12	0.0622	0.18	0.137	2.651473126		0.00397721	0.063942278

Table A.8: Phosphate Analysis

Appendix 3 - Code

Listing 1: Hydrogel Model Script

```
import numpy as np
from scikits.odes import dae
import matplotlib.pyplot as plt
import matplotlib.animation as an
from line_profiler_pycharm import profile
from numba import njit

"""
Transient model resposne - different densities model
saves results as rho_ .npy
"""

# System Parameters
# Values determined from hydrogel Transpiration Paper
pi_0 = (89.9*1000)  # [Pa] osmotic modulus
phi_0 = 0.2  # [] initial polymer volume fraction
eta = 1e-3  # [Pa s] dynamic viscosity of water
v_w = 1.8e-5  # [m3/mol] molar volume of water
rho_w = 1000  # [kg/m3] density of water
rho_p = 1200  # [kg/m3] density of polymer
h = 0.0027  # [m/s] convective mass transfer
Cs = 0.022  # [kg/m3] mass concentration of saturated water vapour (25C)
K_0 = 9e-19  # [m2] permeability of swollen gel
beta = 2 / 3  # [] KozenyCarman equation like parameter for permeability
L_0 = 5e-3  # [m] initial thickness of the gel (5 mm)
R = 8.314  # [m3Pa/K/mol] Ideal Gas Constant
T = 298  # [K] system temperature
e = pi_0*v_w/(phi_0*R*T)
N = 200  # [] number of cells in FVM formulation

a = N + 2  # second PDE index
b = 2 * N + 2  # second PDE index
c = 2 * N + 3  # algebraic index
d = 3 * N + 3  # algebraic index

# ramp for RH change
ramp = 0.5 # [s]


# Kozeny-Carman Equation for permeability
# @njit()
```

```
def perm(p):
    return K_0*(phi_0 / p)**beta


# Darcy's Flux based of cell centred differance
# @njit()
def u_fun(p1, p2, dz):
    p = (p1+p2)/2
    v = K_0*(phi_0 / p)**beta / eta * pi_0/phi_0 * (p1-p2)/dz
    return v


# Residual Function for SUNDIALS IDA Solver
# @profile
def residual(t, x, dx, result):
    # Relative humidity values
    if t < ramp:
        rh_room =  1 - (1-0.7) * np.sin(np.pi * t / (ramp*2))
    else:
        rh_room = 0.7

    L = x[0]  # the length of the domain
    dz = L / N  # recalculate the step size in z direction
    phi = x[1:N + 2]  # phi values at cell centres
    m = x[a:b+1]  # density of cell
    up = x[c:d+1]  # polymer velocities at cell centres
    dldt = dx[0]  # Change in domain size
    dphidt = dx[1:N + 2]  # temporal derivative
    dmdt = dx[N+2:2 * N+3]  # total mass derivative
    n_w = h * Cs * (np.exp(-e * (phi[-1] - phi_0) / phi_0) - rh_room)  # convective flux out of domain
    u_L = n_w / rho_w  # Volumetric flux out of boundary (aka the darcy's flux)
    i = np.arange(1, N)  # positional index
    right = (i + 0.5)/L  # right face index
    left = (i - 0.5)/L  # left face index
    # differential equations
    # domain length temporal derivative
    result[0] = up[-1] - dldt
    # implementation of dphidt function
    result[1] = dphidt[0]
    result[2:N + 1] = ((-phi[1:N] / L * dldt
                        + dldt * (((phi[2:N + 1] + phi[1:N]) / 2 * right)
                                  - ((phi[1:N] + phi[0:N - 1]) / 2 * left))
                        + 1 / dz * (phi[0:N - 1] * up[0:N - 1] - phi[2:N + 1] * up[2:N + 1]) / 2)
                       - dphidt[1:N])
    result[N + 1] = (-phi[N] / L * dldt
```

```
                + 2 * dldt * (phi[N]*N/L - (phi[N] + phi[N - 1])/2 * (N - 0.5)/L)
                + 1 / dz * (phi[N - 1] * up[N - 1] - phi[N] * up[N])
                - dphidt[N])
    # second PDE equation - density
    result[a] = dmdt[0]
    result[a+1:b] = (-m[1:N] / L * dldt
                + dldt * ((m[2:N + 1] + m[1:N]) / 2 * right
                                - ((m[1:N] + m[0:N - 1]) / 2 * left))
                - 1 / dz * ((m[2:N + 1]*up[2:N + 1] - m[0:N - 1]*up[0:N - 1])/2
                        + rho_w*(u_fun(phi[2:N+1], phi[1:N], dz) - u_fun(phi[1:N], phi[0:N-1], dz)))
                - dmdt[1:N])
    result[b] = (-m[N] / L * dldt
              + 2 * dldt * (m[N]*N/L - (m[N] + m[N - 1])/2 * (N - 0.5)/L)
              - 1 / dz * ((m[N]*up[N] - m[N-1]*up[N-1])/2 + rho_w * (u_L - u_fun(phi[N], phi[N-1], dz)))
              - dmdt[N])  # I think the issue may be here in the code?
    # implementation of the algebraic constraints
    result[c] = up[0]
    result[c+1:d+1] = phi[1:]*rho_p + (1-phi[1:])*rho_w - m[1:]


# Initial Conditions
dz0 = L_0 / N  # step size in z direction between nodes
z0 = np.linspace(0, L_0, N+1)  # produce a grid with N+1 nodes space by dz
phi_t0 = np.ones(N+1)*0.2  # initial polymer volume fraction in each cell
m = phi_t0*rho_p + (1-phi_t0)*rho_w
up_0 = np.zeros(N+1)  # Initial polymer velocity in each cell


# construct initial condition vectors
x0 = np.concatenate((np.array(L_0), phi_t0, m, up_0), axis=None)  # [L_0, phi_t0, up_0]
dx0 = np.zeros(len(x0))  # list of initial guesses for the derivative of each variable


# time points to evaluate system at
times = np.linspace(0, 3600*100, 100+1)
# constraints for algebraic variables
constraints_type = np.zeros(len(x0))
constraints_type[:N+2] = 1
constraints_type[a:b+1] = -1

#  SUNDIALS DAE SOLVE using ida method
solver = dae('ida', residual,
          first_step_size=1e-18,
          atol=1e-12,
          rtol=1e-12,
```

```
            max_steps=10000,
            algebraic_vars_idx=[i for i in range(c, d+1)],
            #constraints_type=constraints_type,
            # exclude_algvar_from_error=True,
            old_api=False)

num_runs = 1
for _ in range(num_runs):
    # Evaluate the solver
    solution = solver.solve(times, x0, dx0)

# Create animated plot of the system dynamics
y = solution.values.y[:,1:N+2]
y = 1 - y  # water fraction
yp = solution.values.y[:,1:N+2]  # change in polymer fraction
up_result = solution.values.y[:,c:d+1]
l = solution.values.y[:,0]*1000  # domain length in mm
t = solution.values.t
fig, (ax1, ax2) = plt.subplots(1,2)
dzz = l/N

dzz = dzz.reshape(-1,1)
m = solution.values.y[:, a:b+1]
mass_total = np.sum(m*dzz, axis=1)
mass_polymer = np.sum((1-y)*rho_p*dzz, axis=1)/rho_p
dphidt_result = solution.values.ydot[:,1:N+2]

n_w = h * Cs * (np.exp(-e * (1 - y[-1,-1] - phi_0) / phi_0) - 0.7)  # convective flux out of domain
u_L = n_w / rho_w  # Volumetric flux out of boundary (aka the darcy's flux)
print('-'*5)
print(n_w*3600*1000)  # flux in g per hour
print(l[-1]/L_0/1000)  # length of domian in mm

# save value for plotting later
np.save('rho_y.npy', y)
np.save('rho_t.npy', t)
np.save('rho_l.npy', l)
np.save('rho_m.npy', m)
np.save('rho_up.npy', up_result)
np.save('rho_model_dphi.npy', dphidt_result)


# plot of polymer fraction and density with time
def animate(i):
    ax1.clear()
```

```
    z = np.linspace(0, l[i], N + 1)
    ax1.set_xlim(0,5)
    ax1.set_ylim(rho_w*0.9,rho_p*1.1)
    text = "t-={:.2f}-min".format(t[i]/60)
    ax1.text(1,rho_w*1.1, text)
    ax1.set_title("Hydrogel-density")
    ax1.plot(z, m[i, :])
    ax1.axvline(x=z[-1], color='k')
    ax1.set(xlabel='Thickness-of-Hydrogel-(mm)', ylabel="Density-(kg/m3)")

    ax2.clear()
    z = np.linspace(0, l[i], N + 1)
    ax2.set_xlim(0, 5)
    ax2.set_ylim(0, 1)
    text = "t-={:.2f}-h".format(t[i] / 60/60)
    ax2.text(1, 0.21, text)
    ax2.set_title("Hydrogel-Volume-Fraction")
    ax2.plot(z, y[i, :])
    ax2.axvline(x=z[-1], color='k')
    ax2.set(xlabel='Thickness-of-Hydrogel-(mm)', ylabel="Volume-Fraction")


ani = an.FuncAnimation(fig, animate, frames=range(y.shape[0]))
plt.show()
# ani.save("Hydrogel_shrinking_unequal_rho_change_RH_Nov15.mp4")


# plot of final water fraction profile
z = np.linspace(0, l[-1], N + 1)
plt.xlim(0, 5)
plt.ylim(-.1, 1)
text = "t-={:.2f}-h".format(t[-1] / 60/60)
plt.text(1, 0.21, text)
plt.title("Hydrogel-Volume-Fraction-END")
plt.plot(z,y[-1,:])
plt.axvline(x=z[-1], color='k')
plt.xlabel('Thickness-of-Hydrogel-(mm)')
plt.ylabel("Volume-Fraction")
plt.show()
```

Listing 2: Etzold Model

```
import numpy as np
from scikits.odes import dae
from scipy.optimize import fsolve
import matplotlib.pyplot as plt
```

```
import matplotlib.animation as an

"""
Transient model resposne - Etzold model
saves results as etzold_model_ .npy
"""

# System Parameters
# Values determined from hydrogel Transpiration Paper
pi_0 = (89.9*1000)  # [Pa] osmotic modulus
phi_0 = 0.2  # [] initial polymer volume fraction
eta = 1e-3  # [Pa s] dynamic viscosity of water
v_w = 1.8e-5  # [m3/mol] molar volume of water
rho_w = 1000  # [kg/m3] density of water
rho_p = 1200  # [kg/m3] density of polymer
h = 0.0027  # [m/s] convective mass transfer
Cs = 0.022  # [kg/m3] mass concentration of saturated water vapour (25C)
K_0 = 9e-19  # [m2] permeability of swollen gel
beta = 2 / 3  # [] Kozeny-Carman equation like parameter for permeability
L_0 = 5e-3  # [m] initial thickness of the gel (5 mm)
R = 8.314  # [m3Pa/K/mol] Ideal Gas Constant
T = 298  # [K] system temperature
d = pi_0*v_w/(phi_0*R*T)
N = 200  # [] number of cells in FVM formulation


a = N + 2  # first algebraic constraint index
b = 2 * N + 2 # last algebraic constraint index

# ramp for RH value
ramp = 0.5 # [s]


# Kozeny-Carman Equation for permeability
def perm(p):
    return K_0*(phi_0 / p)**beta


# Darcy's Flux based of cell centred differance
def u_fun(p1, p2, dz):
    p = (p1+p2)/2
    v = perm(p) / eta * pi_0/phi_0 * (p1-p2)/dz
    return v
```

```
# Residual Function for SUNDIALS IDA Solver
def residual(t, x, dx, result):
    if t < ramp:
        rh_room = 1 - 0.3 * np.sin(np.pi * t / (ramp*2))
    else:
        rh_room = 0.7

    phi = x[0:N]  # phi values at cell centres
    dphidz_end = x[N]  # derivative at boundary
    dphidt = dx[0:N]  # temporal derivatives for polymer fraction
    dz = (phi_0*L_0/(np.sum(phi)))  # recalculate the step size in z direction
    L = N*dz  # size of domain
    i = np.arange(1,N-1)  # positional index
    q = (perm(phi_0) / eta * pi_0/phi_0 * 2*(phi[0]-phi_0)/dz)  # phase-averaged material flux
    phi_end = phi[N-1] + dz/2 * dphidz_end # estimated boundary volume fraction
    n_w = h * Cs * (np.exp(-d * (phi_end - phi_0) / phi_0) - rh_room)  # convective flux out of domain
    u_L = n_w / rho_w  # Volumetric flux out of boundary (aka the darcy's flux)
    dldt = q - u_L  # change in domain size at boundary
    # differential equations
    # implementation of dphidt function
    result[0] = ((-phi[0] / L * dldt
                    + 1 / dz * dldt * (((phi[1] + phi[0]) / 2*dz/L))
                    + 1 / dz * ( (phi[1] + phi[0])/2 * u_fun(phi[1], phi[0], dz) - phi_0 * q)
                    - q / dz * ((phi[1]+phi[0])/2 -phi_0))
                -dphidt[0])

    result[1:N-1] = ((-phi[1:N-1] / L * dldt
                    + 1 / dz * dldt * (((phi[2:N] + phi[1:N-1]) / 2 * (i + 1)*dz/L)
                                    - ((phi[1:N-1] + phi[0:N - 2]) / 2 * i*dz/L))
                    + 1 / dz * ( (phi[2:N] + phi[1:N-1])/2 * u_fun(phi[2:N], phi[1:N-1], dz) - (phi[1:N-1] +
      phi[0:N-2])/2 * u_fun(phi[1:N-1], phi[0:N-2], dz))
                    - q / dz * ((phi[2:N] - phi[0:N - 2]) / 2))
                   - dphidt[1:N-1])

    result[N-1] = ((-phi[N-1] / L * dldt
                      + 1 / dz * dldt * (phi_end * N * dz / L - (phi[N-1] + phi[N-2]) / 2 * (N-1) * dz / L)
                + 1 / dz * (phi_end * u_L - (phi[N-1] + phi[N-2]) / 2 * u_fun(phi[N-1], phi[N-2], dz)))
                - q / dz * (phi_end - (phi[N-1] + phi[N-2])/2)
                - dphidt[N-1])
    # algebraic constraint
    result[N] = u_fun(phi_end, phi[N-1], dz/2) - u_L  # flux out of domain equals the darcy flux at
      domain boundary


#  construct initial condition vectors
```

```
phi_t0 = phi_0*np.ones(N)
x0 = np.concatenate((phi_t0, np.array([0])))  # [phi_0, initial estimate for dphidz_end ]
dx0 = np.zeros(len(x0))  # list of initial guesses for dphidt


# time points to evaluate system at
times = np.linspace(0, 3600*100, 100+1)

#  SUNDIALS DAE SOLVE using ida method
solver = dae('ida', residual,
             first_step_size=1e-18,
             atol=1e-6,
             rtol=1e-6,
             max_steps=10000,
             algebraic_vars_idx=[N],
             old_api=False)


# Evaluate the solver
solution = solver.solve(times, x0, dx0)


# Create animated plot of the system dynamics
y = solution.values.y[:,:N] # polymer fraction
dzz = (phi_0*L_0/(np.sum(y,axis=1)))  # size of each cell
l = dzz*N*1000  # length of domain in mm
y = 1 - y  # water fraction
t = solution.values.t
dphidt_result = solution.values.ydot[:,:N]
fig, ax = plt.subplots()

# save arrays to plot later
np.save('etzold_model_y.npy', y)
np.save('etzold_model_l.npy', l)
np.save('etzold_model_t.npy', t)
np.save('etzold_model_dphi.npy', dphidt_result)


# animation of gel
def animate(i):
    ax.clear()
    z = np.linspace(0, l[i], N)
    ax.set_xlim(0,5)
    ax.set_ylim(0.15, 1)
    text = "t = {:.2f} min".format(t[i]/60)
```

```
    ax.text(1, 0.21, text)
    ax.set_title("Hydrogel-Visualtizaton")
    ax.plot(z,y[i,:])
    ax.axvline(x=z[-1], color='k')
    plt.xlabel("Thickness-of-Hydrogel-(mm)")
    plt.ylabel("Volume-Fraction-of-Water")


ani = an.FuncAnimation(fig, animate, frames=range(y.shape[0]))
plt.show()
# ani.save("Hydrogel_shrinking_water_profile_Nov_3.mp4")

# array of relative humidity
rhroom = []
for i in t:
    if i < ramp:
        rh = 1 - 0.3 * np.sin(np.pi * i / (ramp * 2))
        rhroom.append(rh)
    else:
        rh = 0.7
rhroom = np.array(rhroom)


# plot flux out of domain with time
n_flux = h * Cs * (np.exp(-v_w * pi_0 / (R * T) * ((1 - y[:, -1])-phi_0) / phi_0) - rhroom)/ 10E-5
plt.plot(t/60, n_flux)
plt.title("mass-flux-of-water-out-of-gel-at-L(t)")
plt.xlabel("time-min")
plt.ylabel("mass-flux-g/s/m^2-10^5")
#plt.ylim(0, 1)
plt.show()
```

Listing 3: Model Comparision Script

```
import numpy as np
import matplotlib.pyplot as plt
import matplotlib.animation as an

"""
Generates the plots to compare the three models
depends on the .npy files of the other models
N must be the same in this file and all model files
"""


# Values determined from hydrogel Transpiration Paper
```

```
pi_0 = (89.9*1000)  # [Pa] osmotic modulus
phi_0 = 0.2  # [] initial polymer volume fraction
eta = 1e-3  # [Pa s] dynamic viscosity of water
v_w = 1.8e-5  # [m3/mol] molar volume of water
rho_w = 1000  # [kg/m3] density of water
rho_p = 1200  # [kg/m3] density of polymer
h = 0.0027  # [m/s] convective mass transfer
Cs = 0.022  # [kg/m3] mass concentration of saturated water vapour (25C)
K_0 = 9e-19  # [m2] permeability of swollen gel
beta = 2 / 3  # [] Kozeny-Carman equation like parameter for permeability
L_0 = 5e-3  # [m] initial thickness of the gel (5 mm)
R = 8.314  # [m3Pa/K/mol] Ideal Gas Constant
T = 298  # [K] system temperature
d = pi_0*v_w/(phi_0*R*T)
N = 200  # [] number of cells in FVM formulation

a = N + 2  # first algebraic constraint index
b = 2 * N + 2 # last algebraic constraint index
rh_room = 0.7
ramp = 0.5 # [s]

# Kozeny-Carman Equation for permeability
def perm(p):
    return K_0*(phi_0 / p)**beta

# Darcy's Flux based of cell centred differance
def u_fun(p1, p2, dz):
    p = (p1+p2)/ 2
    v = perm(p) / eta * pi_0/phi_0 * (p1-p2)/dz
    return v


# y is the water fraction
# load data from saved runs
# load the equal densities model
my_y = np.load('my_model_y.npy')  # water fraction
my_l = np.load('my_model_l.npy')  # length of domain
my_t = np.load('my_model_t.npy')  # time
my_m = (my_y*rho_w + (1-my_y)*rho_p) / rho_p  # mass conservation - scaled by rho_p
my_up = np.load('my_model_up.npy')  # polymer velocity
my_dphi = np.load('my_model_dphi.npy')  # change in polymer fraction
my_dz = (my_l/1000 / (N+1)).reshape(-1,1)  # size of each cell
my_u = u_fun((1-my_y[:, 1:]), (1-my_y[:, :-1]), my_dz)  # darcy flux
my_u_1 = my_u[:,0].reshape(-1,1) # flux in/out of first node are balanced
my_up_face = (my_up[:, :-1] + my_up[:, 1:]) / 2  # face value of the polymer velocity between cells
```

```
rhs = my_u + my_up_face  # right hand side of the divergence equation
my_divergance = rhs[:,:-1] - rhs[:,1:]  # divergence term


#  etzold model
et_y = np.load('etzold_model_y.npy')  # water fraction
et_l = np.load('etzold_model_l.npy')  # length
et_t = np.load('etzold_model_t.npy')  # time
et_dphi = np.load('etzold_model_dphi.npy')  # change in polymer fraction
et_m = (et_y*rho_w + (1-et_y)*rho_p) / rho_p  # mass conservation - scaled by rho_p
et_dz = et_l/1000 / (N)  # cell size
et_dz = et_dz.reshape(-1,1)
et_u = u_fun((1-et_y[:, 1:]), (1-et_y[:, :-1]), my_dz)  # darcy flux
q = (perm(phi_0) / eta * pi_0/phi_0 * 2*((1-et_y[:,0]).reshape(-1,1)-phi_0)/et_dz)  # divergence-free
    phase average flux
et_u = np.concatenate((q, et_u), axis=1)
et_up = q - et_u  # polymer velocity
et_rhs= et_up + et_u  # right hand side of divergence term
et_grad_term = (et_rhs[:, :-1] - et_rhs[:, 1:])/et_dz  # divergence term


#  My model with unequal densities
rho_y = np.load('rho_y.npy')  # water fraction
rho_t = np.load('rho_t.npy')  # time
rho_m = np.load('rho_m.npy')  # mass conservation
rho_l = np.load('rho_l.npy')  # length
rho_m = rho_m / rho_p  # scaled mass conservation
rho_up = np.load('rho_up.npy')  # polymer velocity
rho_dphi = np.load('rho_model_dphi.npy')  # change in polymer fraction
rho_dz = (rho_l/1000 / (N+1)).reshape(-1,1)  # cell size
rho_u = u_fun((1-rho_y[:, 1:]), (1-rho_y[:, :-1]), rho_dz)  # darcy flux
rho_u_1 = rho_u[:,0].reshape(-1,1)
# rho_u = np.concatenate((rho_u_1, rho_u), axis=1)
rho_up_face = (rho_up[:, :-1] + rho_up[:, 1:]) / 2
rhs = rho_u + rho_up_face
rho_divergance = rhs[:,:-1] - rhs[:,1:]  # divergence term
fig, ax = plt.subplots()


# animation of divergence term with time
def animate1(i):
    ax.clear()
    ax.set_xlim(0,5)
    ax.set_ylim(-1e-11,1e-11)
    # ax.set_title("Divergence Term ")
```

```
    plt.xlabel("Thickness of Hydrogel (mm)")
    plt.ylabel(r"$\nabla \cdot (u_p + u)$")
    my_z = np.linspace(0, my_l[i], N + 1)
    text = "t = {:.2f} min".format(my_t[i]/60)
    ax.text(1, -.8e-11, text)
    ax.plot(my_z[1:-1],my_divergance[i,:], label='my model equal rho')
    ax.axvline(x=my_z[-1], color='k')

    et_z = np.linspace(0, et_l[i], N)
    text = "t = {:.2f} min".format(et_t[i] / 60)
    ax.text(1, 0.21, text)
    ax.plot(et_z[1:], et_grad_term[i, :],  label='etzold model')
    ax.axvline(x=et_z[-1], color='k')

    rho_z = np.linspace(0, rho_l[i], N+1)
    text = "t = {:.2f} min".format(rho_t[i] / 60)
    ax.text(1, 0.21, text)
    ax.plot(rho_z[1:-1], rho_divergance[i, :], label='my model diff rho')
    ax.axvline(x=rho_z[-1], color='k')
    ax.legend()


ani = an.FuncAnimation(fig, animate1, frames=range(my_y.shape[0]))
plt.show()
# ani.save("divergence.mp4")


# animation of density with time
def animate2(i):
    ax.clear()
    ax.set_xlim(0,5)
    ax.set_ylim(.8,1)
    # ax.set_title("density")
    plt.xlabel("Thickness of Hydrogel (mm)")
    plt.ylabel(r"density ($\rho/\rho_p$)")
    my_z = np.linspace(0, my_l[i], N + 1)
    text = "t = {:.2f} min".format(my_t[i]/60)
    ax.text(1, 0.85, text)
    ax.plot(my_z,my_m[i,:], label='my model equal rho')
    ax.axvline(x=my_z[-1], color='k')

    et_z = np.linspace(0, et_l[i], N)
    text = "t = {:.2f} min".format(et_t[i] / 60)
    ax.text(1, 0.21, text)
    ax.plot(et_z, et_m[i, :], label='etzold model')
```

```
    ax.axvline(x=et_z[-1], color='k')

    rho_z = np.linspace(0, rho_l[i], N+1)
    text = "t-=-{:.2f}-min".format(rho_t[i] / 60)
    ax.text(1, 0.21, text)
    ax.plot(rho_z, rho_m[i, :], label='my-model-diff-rho')
    ax.axvline(x=rho_z[-1], color='k')
    ax.legend()


fig, ax = plt.subplots()
ani = an.FuncAnimation(fig, animate2, frames=range(my_y.shape[0]))
plt.show()
# ani.save("density.mp4")


# animation of u and up
def animate3(i):
    ax.clear()
    ax.set_xlim(0,5)
    ax.set_ylim(-10e-8,10e-8)
    # ax.set_title("u and up")
    plt.xlabel("Thickness-of-Hydrogel-(mm)")
    plt.ylabel(r"u-&-up-($m-\;-s^{-1}$)")
    my_z = np.linspace(0, my_l[i], N + 1)
    text = "t-=-{:.2f}-min".format(my_t[i]/60)
    ax.text(1, -5e-8, text)
    ax.plot(my_z[1:],my_u[i,:], 'b-', label='my-model-equal-rho-u')
    ax.plot(my_z, my_up[i, :], 'b--', label='my-model-equal-rho-up')
    ax.axvline(x=my_z[-1], color='k')

    et_z = np.linspace(0, et_l[i], N)
    text = "t-=-{:.2f}-min".format(et_t[i] / 60)
    ax.text(1, 0.21, text)
    ax.plot(et_z, et_u[i, :], 'r-', label='etzold-model')
    ax.plot(et_z, et_up[i, :], 'r--', label='etzold-model-up')
    ax.axvline(x=et_z[-1], color='k')

    rho_z = np.linspace(0, rho_l[i], N+1)
    text = "t-=-{:.2f}-min".format(rho_t[i] / 60)
    ax.text(1, 0.21, text)
    ax.plot(rho_z[1:], rho_u[i, :],'g-', label='my-model-diff-rho')
    ax.plot(rho_z, rho_up[i, :], 'g--', label='my-model-equal-rho-up')
    ax.axvline(x=rho_z[-1], color='k')
    ax.legend()
```

```
fig, ax = plt.subplots()
ani = an.FuncAnimation(fig, animate3, frames=range(my_y.shape[0]))
plt.show()
# ani.save("u_up.mp4")

# make relative humidity array
rhroom = []
for i in my_t:
    if i < ramp:
        rh = 1 - 0.3 * np.sin(np.pi * i / (ramp * 2))
        rhroom.append(rh)
    else:
        rh = 0.7
        rhroom.append(rh)

rhroom = np.array(rhroom)



# plot the flux vs time for each model
my_n_flux = h * Cs * (np.exp(-d*((1 - my_y[:, -1])-phi_0) / phi_0) - rhroom)
plt.plot(my_t[1:]/60, my_n_flux[1:]*3600*1000, label='my model equal rho')
et_n_flux = h * Cs * (np.exp(-d* ((1 - et_y[:, -1])-phi_0) / phi_0) - rhroom)
plt.plot(et_t[1:]/60, et_n_flux[1:]*3600*1000, label='etzold model')
rho_n_flux = h * Cs * (np.exp(-d* ((1 - rho_y[:, -1])-phi_0) / phi_0) - rhroom)
plt.plot(rho_t[1:]/60, rho_n_flux[1:]*3600*1000, label='my model diff rho' )
# plt.title("mass flux of water out of gel at L(t)")
plt.xlabel("Time (min)")
plt.ylabel(r"Mass Flux $g \: h^{-1} \; m^{-2}$")
plt.ylim(63.25,64.25)
plt.legend()
# plt.tight_layout()
plt.show()



# plot the polymer mass conservation for each model - should be 1
my_z = my_l/(N+1)
et_z = et_l / N
rho_z = rho_l / (N+1)
my_mb = np.sum((1-my_y), axis=1)*my_z/phi_0/L_0/1000  # saved in mm
et_mb = np.sum((1-et_y), axis=1)*et_z/phi_0/L_0/1000  # saved in mm
rho_mb = np.sum((1-rho_y), axis=1)*rho_z/phi_0/L_0/1000  # saved in mm
print(my_mb[-1])
```

```
plt.plot(my_t/60, my_mb, label='my-model-equal-rho')
plt.plot(et_t/60, et_mb, label='etzold-model')
plt.plot(rho_t/60, rho_mb, label='my-model-diff-rho')
plt.xlim(-10,my_t[-1]/60)
plt.ylim(0.999, 1.001)
plt.legend()
# plt.title('Polymer conservation')
plt.ylabel('Polymer-Conservation')
plt.xlabel('Time-(min)')
# plt.tight_layout()
plt.show()
```

Listing 4: Permeability Sensitivity Script

```
import numpy as np
from scikits.odes import dae
from scipy.optimize import fsolve
import matplotlib.pyplot as plt
import matplotlib.animation as an
from line_profiler_pycharm import profile
from numba import njit

"""
Tests different tau values in the traisnet model - not used in thesis
"""

# System Parameters
# global L_0, phi_t0
# Values determined from hydrogel Transpiration Paper
pi_0 = (89.9*1000)  # [Pa] osmotic modulus
phi_0 = 0.2  # [] initial polymer volume fraction
eta = 1e-3  # [Pa s] dynamic viscosity of water
v_w = 1.8e-5  # [m3/mol] molar volume of water
rho_w = 1000  # [kg/m3] density of water
rho_p = 1200  # [kg/m3] density of polymer
h = 0.0027  # [m/s] convective mass transfer
Cs = 0.022  # [kg/m3] mass concentration of saturated water vapour (25C)
# K_0 = 9e-19  # [m2] permeability of swollen gel
beta = 2 / 3  # [] KozenyCarman equation like parameter for permeability
L_0 = 5e-3  # [m] initial thickness of the gel (5 mm)
R = 8.314  # [m3Pa/K/mol] Ideal Gas Constant
T = 298  # [K] system temperature
e = pi_0*v_w/(phi_0*R*T)
N = 50  # [] number of cells in FVM formulation

a = N + 2  # second PDE index
```

```
b = 2 * N + 2  # second PDE index
c = 2 * N + 3  # algebraic index
d = 3 * N + 3  # algebraic index
RH = .5
ramp = 0.5 # [s]

# Kozeny-Carman Equation for permeability
# @njit()
def perm(p):
    return K_0*(phi_0 / p)**beta


# Darcy's Flux based of cell centred differance
# @njit()
def u_fun(p1, p2, dz):
    p = (p1+p2)/2
    v = K_0*(phi_0 / p)**beta / eta * pi_0/phi_0 * (p1-p2)/dz
    return v


# Residual Function for SUNDIALS IDA Solver
# @profile
def residual(t, x, dx, result):
    if t < ramp:
        rh_room =  1 + (RH-1) * np.sin(np.pi * t / (ramp*2))
    elif t < 3600*72:
        rh_room = RH
    elif t < 3600*72 + ramp:
        rh_room = RH + (0.2-RH) * np.sin(np.pi * (t-3600*72)/(ramp*2))
    elif t < 3600*100:
        rh_room = 0.2
    elif t < 3600*100 + ramp:
        rh_room = 0.2 + (RH+0.2-0.2) * np.sin(np.pi * (t-3600*100)/(ramp*2))
    else:
        rh_room = RH +0.2

    L = x[0]  # the length of the domain
    dz = L / N  # recalculate the step size in z direction
    phi = x[1:N + 2]  # phi values at cell centres
    m = x[a:b+1]
    up = x[c:d+1]  # polymer velocities at cell centres
    dldt = dx[0]  # Change in domain size
    dphidt = dx[1:N + 2]  # temporal derivative
    dmdt = dx[N+2:2 * N+3]  # total mass derivative
    n_w = h * Cs * (np.exp(-e * (phi[-1] - phi_0) / phi_0) - rh_room)  # convective flux out of domain
```

```
    u_L = n_w / rho_w  # Volumetric flux out of boundary (aka the darcy's flux)
    i = np.arange(1, N)  # positional index
    right = (i + 0.5)/L
    left = (i - 0.5)/L
    # differential equations
    # change in domain length
    result[0] = up[-1] - dldt
    # differential equations
    # implementation of dphidt function
    result[1] = dphidt[0]
    result[2:N + 1] = ((-phi[1:N] / L * dldt
                      + dldt * (((phi[2:N + 1] + phi[1:N]) / 2 * right)
                                - ((phi[1:N] + phi[0:N - 1]) / 2 * left))
                      + 1 / dz * (phi[0:N - 1] * up[0:N - 1] - phi[2:N + 1] * up[2:N + 1]) / 2)
                      - dphidt[1:N])
    result[N + 1] = (-phi[N] / L * dldt
                    + 2 * dldt * (phi[N]*N/L - (phi[N] + phi[N - 1])/2 * (N - 0.5)/L)
                    + 1 / dz * (phi[N - 1] * up[N - 1] - phi[N] * up[N])
                    - dphidt[N])
    # second PDE equation
    result[a] = dmdt[0]
    result[a+1:b] = (-m[1:N] / L * dldt
                    + dldt * ((m[2:N + 1] + m[1:N]) / 2 * right
                              - ((m[1:N] + m[0:N - 1]) / 2 * left))
                    - 1 / dz * ((m[2:N + 1]*up[2:N + 1] - m[0:N - 1]*up[0:N - 1])/2
                              + rho_w*(u_fun(phi[2:N+1], phi[1:N], dz) - u_fun(phi[1:N], phi[0:N-1], dz)))
                    - dmdt[1:N])
    result[b] = (-m[N] / L * dldt
                + 2 * dldt * (m[N]*N/L - (m[N] + m[N - 1])/2 * (N - 0.5)/L)
                - 1 / dz * ((m[N]*up[N] - m[N-1]*up[N-1])/2 + rho_w * (u_L - u_fun(phi[N], phi[N-1], dz)))
                - dmdt[N])  # I think the issue may be here in the code?
    # implementation of the algebraic constraints
    result[c] = up[0]
    result[c+1:d+1] = phi[1:]*rho_p + (1-phi[1:])*rho_w - m[1:]


# Initial Conditions
dz0 = L_0 / N  # step size in z direction between nodes
z0 = np.linspace(0, L_0, N+1)  # produce a grid with N+1 nodes space by dz
# phi_t0 = np.linspace(phi_0, sol*L_0+phi_0, N+1)
phi_t0 = np.ones(N+1)*0.2  # initial polymer volume fraction in each cell
m = phi_t0*rho_p + (1-phi_t0)*rho_w
up_0 = np.zeros(N+1)  # Initial polymer velocity in each cell
```

```
# construct initial condition vectors
x0 = np.concatenate((np.array(L_0), phi_t0, m, up_0), axis=None)  # [L_0, phi_t0, up_0]
dx0 = np.zeros(len(x0))  # list of initial guesses for the derivative of each variable


# time points to evaluate system at
times = np.linspace(0, 3600*72*3, 60*72*3+1)
# constraints for algebraic variables
constraints_type = np.zeros(len(x0))
constraints_type[:N+2] = 1
constraints_type[a:b+1] = -1

#  SUNDIALS DAE SOLVE using ida method
solver = dae('ida', residual,
             first_step_size=1e-18,
             atol=1e-12,
             rtol=1e-12,
             max_steps=10000,
             algebraic_vars_idx=[i for i in range(c, d+1)],
             #constraints_type=constraints_type,
             # exclude_algvar_from_error=True,
             old_api=False)

from time import perf_counter_ns

K_values = np.linspace(7e-19, 1.5e-18 , 5)
# tau_value = L_0**2*rho_p*eta*phi_0**(1/3) / (rho_w*K_values*pi_0)
# h_all = h0*tau_value[3]/tau_value
length = []
for i in range(len(K_values)):
    # Evaluate the solver
    K_0 = K_values[i]
    # h = h_all[i]
    solution = solver.solve(times, x0, dx0)

    # Create animated plot of the system dynamics
    y = solution.values.y[:,1:N+2]
    l = solution.values.y[:,0]*1000
    t = solution.values.t
    length.append(l)

    n_w = h * Cs * (np.exp(-e * (1 - y[-1,-1] - phi_0) / phi_0) - RH)  # convective flux out of domain
    u_L = n_w / rho_w  # Volumetric flux out of boundary (aka the darcy's flux)
    print('-'*5)
    print(n_w*3600*1000)  # g per hour
```

```
    print(l[-1]/L_0/1000)  # mm


length = np.array(length).reshape(len(K_values), -1)

RH_list = []
for i in range(len(t)):

    if t[i] < ramp:
        rh_room =  1 - (1-RH) * np.sin(np.pi * t[i] / (ramp*2))
    elif t[i] < 3600*72:
        rh_room = RH
    elif t[i] < 3600*72 + ramp:
        rh_room = RH - (0.2-RH) * np.sin(np.pi * (t[i]-3600*72)/(ramp*2))
    elif  t[i] < 3600*100:
        rh_room = 0.2
    elif t[i] < 3600*100 + ramp:
        rh_room = 0.2 + (RH+0.2-0.2) * np.sin(np.pi * (t[i]-3600*100)/(ramp*2))
    else:
        rh_room = RH + 0.2
    RH_list.append(rh_room)

RH_np = np.array(RH_list)

fig, ax1 = plt.subplots()
ax1.set_xlabel('time (h)')
ax1.set_ylabel("Dimensionless Thickness")
for i in range(len(K_values)):
    ax1.plot(t/60/60, length[i,:]/5, label=r'$K_0 \times 10^{19}$' + f' = {K_values[i]*10**19:.2f}' + r'
      $m^2 s^{-1}$')
ax1.tick_params(axis='y')
ax2 = ax1.twinx()  # instantiate a second axes that shares the same x-axis
ax1.legend()

color = 'gray'
ax2.set_ylabel('Relative Humidity', color=color)  # we already handled the x-label with ax1
ax2.plot(t/60/60, RH_np*100, color=color, linestyle='dashed')
ax2.tick_params(axis='y', labelcolor=color)
fig.tight_layout()  # otherwise the right y-label is slightly clipped
plt.show()
```

Listing 5: RH Transient Response Script

```
import numpy as np
from scikits.odes import dae
from scipy.optimize import fsolve
```

```
import matplotlib.pyplot as plt
import matplotlib.animation as an
from line_profiler_pycharm import profile
from numba import njit
from mpl_toolkits.axes_grid1.inset_locator import inset_axes

"""
Transient response to step changes in relative humidity
plot for flux out of domain
plot for dimensionless length of domain
"""
# System Parameters
# Values determined from hydrogel Transpiration Paper
pi_0 = (89.9*1000)  # [Pa] osmotic modulus
phi_0 = 0.2  # [] initial polymer volume fraction
eta = 1e-3  # [Pa s] dynamic viscosity of water
v_w = 1.8e-5  # [m3/mol] molar volume of water
rho_w = 1000  # [kg/m3] density of water
rho_p = 1200  # [kg/m3] density of polymer
h = 0.0027  # [m/s] convective mass transfer
Cs = 0.022  # [kg/m3] mass concentration of saturated water vapour (25C)
K_0 = 9e-19  # [m2] permeability of swollen gel
beta = 2 / 3  # [] KozenyCarman equation like parameter for permeability
L_0 = 5e-3  # [m] initial thickness of the gel (5 mm)
R = 8.314  # [m3Pa/K/mol] Ideal Gas Constant
T = 298  # [K] system temperature
e = pi_0*v_w/(phi_0*R*T)
N = 50  # [] number of cells in FVM formulation

a = N + 2  # second PDE index
b = 2 * N + 2  # second PDE index
c = 2 * N + 3  # algebraic index
d = 3 * N + 3  # algebraic index
RH = .7
ramp = 0.5 # [s]

# Kozeny-Carman Equation for permeability
# @njit()
def perm(p):
    return K_0*(phi_0 / p)**beta


# Darcy's Flux based of cell centred differance
# @njit()
def u_fun(p1, p2, dz):
```

```
    p = (p1+p2)/2
    v = K_0*(phi_0 / p)**beta / eta * pi_0/phi_0 * (p1-p2)/dz
    return v

# Residual Function for SUNDIALS IDA Solver
# @profile
def residual(t, x, dx, result):
    if t < ramp:
        rh_room =  1 - (1-RH) * np.sin(np.pi * t / (ramp*2))
    elif t < 3600*24:
        rh_room = RH
    elif t < 3600*24 + ramp:
        rh_room = RH - (RH) * np.sin(np.pi * (t-3600*48)/(ramp*2))
    elif t < 3600*48:
        rh_room = 0
    elif t < 3600*48 + ramp:
        rh_room = (RH+0.2) * np.sin(np.pi * (t-3600*24)/(ramp*2))
    else:
        rh_room = RH + 0.2

    L = x[0]  # the length of the domain
    dz = L / N  # recalculate the step size in z direction
    phi = x[1:N + 2]  # phi values at cell centres
    m = x[a:b+1]
    up = x[c:d+1]  # polymer velocities at cell centres
    dldt = dx[0]  # Change in domain size
    dphidt = dx[1:N + 2]  # temporal derivative
    dmdt = dx[N+2:2 * N+3]  # total mass derivative
    n_w = h * Cs * (np.exp(-e * (phi[-1] - phi_0) / phi_0) - rh_room)  # convective flux out of domain
    u_L = n_w / rho_w  # Volumetric flux out of boundary (aka the darcy's flux)
    i = np.arange(1, N)  # positional index
    right = (i + 0.5)/L
    left = (i - 0.5)/L
    #This is the first attempt
    result[0] = up[-1] - dldt
    # differential equations
    # implementation of dphidt function
    result[1] = dphidt[0]
    result[2:N + 1] = ((-phi[1:N] / L * dldt
                        + dldt * (((phi[2:N + 1] + phi[1:N]) / 2 * right)
                                  - ((phi[1:N] + phi[0:N - 1]) / 2 * left))
                        + 1 / dz * (phi[0:N - 1] * up[0:N - 1] - phi[2:N + 1] * up[2:N + 1]) / 2)
                       - dphidt[1:N])
    result[N + 1] = (-phi[N] / L * dldt
                     + 2 * dldt * (phi[N]*N/L - (phi[N] + phi[N - 1])/2 * (N - 0.5)/L)
```

```
                + 1 / dz * (phi[N - 1] * up[N - 1] - phi[N] * up[N])
                - dphidt[N])
    # second PDE equation
    result[a] = dmdt[0]
    result[a+1:b] = (-m[1:N] / L * dldt
                + dldt * ((m[2:N + 1] + m[1:N]) / 2 * right
                                - ((m[1:N] + m[0:N - 1]) / 2 * left))
                - 1 / dz * ((m[2:N + 1]*up[2:N + 1] - m[0:N - 1]*up[0:N - 1])/2
                            + rho_w*(u_fun(phi[2:N+1], phi[1:N], dz) - u_fun(phi[1:N], phi[0:N-1], dz)))
                - dmdt[1:N])
    result[b] = (-m[N] / L * dldt
               + 2 * dldt * (m[N]*N/L - (m[N] + m[N - 1])/2 * (N - 0.5)/L)
               - 1 / dz * ((m[N]*up[N] - m[N-1]*up[N-1])/2 + rho_w * (u_L - u_fun(phi[N], phi[N-1], dz)))
               - dmdt[N])  # I think the issue may be here in the code?
    # implementation of the algebraic constraints
    result[c] = up[0]
    result[c+1:d+1] = phi[1:]*rho_p + (1-phi[1:])*rho_w - m[1:]

# Initial Conditions
dz0 = L_0 / N  # step size in z direction between nodes
z0 = np.linspace(0, L_0, N+1)  # produce a grid with N+1 nodes space by dz
# phi_t0 = np.linspace(phi_0, sol*L_0+phi_0, N+1)  # initial polymer volume fraction in each cell
phi_t0 = np.ones(N+1)*0.2
m = phi_t0*rho_p + (1-phi_t0)*rho_w
# u_check2 = u_fun(phi_t0[-1], phi_t0[-2], dz0)
up_0 = np.zeros(N+1)  # Initial polymer velocity in each cell


# construct initial condition vectors
x0 = np.concatenate((np.array(L_0), phi_t0, m, up_0), axis=None)  # [L_0, phi_t0, up_0]
dx0 = np.zeros(len(x0))  # list of initial guesses for the derivative of each variable


# time points to evaluate system at
times = np.linspace(0, 3600*100, 60*100+1)
# constraints for algebraic variables
constraints_type = np.zeros(len(x0))
constraints_type[:N+2] = 1
constraints_type[a:b+1] = -1

#  SUNDIALS DAE SOLVE using ida method
solver = dae('ida', residual,
            # compute_initcond='yp0',
            # compute_initcond_t0= 1e-18,
            first_step_size=1e-18,
```

```
            atol=1e-12,
            rtol=1e-12,
            max_steps=10000,
            algebraic_vars_idx=[i for i in range(c, d+1)],
            #constraints_type=constraints_type,
            # exclude_algvar_from_error=True,
            old_api=False)

from time import perf_counter_ns

num_runs = 1
start = perf_counter_ns()
for _ in range(num_runs):
    # Evaluate the solver
    solution = solver.solve(times, x0, dx0)

print((perf_counter_ns() - start) / 1000. / 1000. / num_runs)

# Create animated plot of the system dynamics
y = solution.values.y[:,1:N+2]
y = 1 - y
yp = solution.values.y[:,1:N+2]
up_result = solution.values.y[:,c:d+1]
l = solution.values.y[:,0]*1000
t = solution.values.t
# fig, (ax1, ax2) = plt.subplots(1,2)
dzz = l/N
dzz = dzz.reshape(-1,1)
m = solution.values.y[:, a:b+1]
mass_total = np.sum(m*dzz, axis=1)
mass_polymer = np.sum((1-y)*rho_p*dzz, axis=1)/rho_p
dphidt_result = solution.values.ydot[:,1:N+2]

n_w = h * Cs * (np.exp(-e * (1 - y[-1,-1] - phi_0) / phi_0) - RH)  # convective flux out of domain
u_L = n_w / rho_w  # Volumetric flux out of boundary (aka the darcy's flux)
print('-'*5)
print(n_w*3600*1000)
print(l[-1]/L_0/1000)


# generate RH data for plotting
RH_list = []
for i in range(len(t)):
    if t[i] < ramp:
        rh_room =  1 - (1-RH) * np.sin(np.pi * t[i] / (ramp*2))
```

```
    elif t[i] < 3600*24:
        rh_room = RH
    elif t[i] < 3600*24 + ramp:
        rh_room = RH - (RH) * np.sin(np.pi * (t[i]-3600*48)/(ramp*2))
    elif  t[i] < 3600*48:
        rh_room = 0
    elif t[i] < 3600*48 + ramp:
        rh_room = (RH+0.2) * np.sin(np.pi * (t[i]-3600*24)/(ramp*2))
    else:
        rh_room = RH + 0.2
    # if time < ramp:
    #     rh_room =  1 - (1-RH) * np.sin(np.pi * time / (ramp*2))
    # else:
    #     rh_room = RH
    RH_list.append(rh_room)

RH_np = np.array(RH_list)

# calculate the flux out of domain
n_flux = h * Cs * (np.exp(-v_w * pi_0 / (R * T) * (yp[:, -1]-phi_0) / phi_0) - RH_np)*3600*1000


# plot the flux vs time and relative humidity
fig, ax1 = plt.subplots()
color = 'tab:blue'
ax1.set_xlabel('time (h)')
ax1.set_ylabel(r"Water Transport $g \; h^{-1} m^{-2}$", color=color)
ax1.plot(t/60/60, n_flux, color=color)
# ax1.plot([x1[0]/60/60, x1[-1]/60/60], [y1[0], y1[-1]], '-g')
ax1.tick_params(axis='y', labelcolor=color)
ax_inset = inset_axes(ax1, width="30%", height="30%", loc='center right')
ax_inset.plot(t[60*48:60*50]/60/60, n_flux[60*48:60*50])
ax_inset.set_ylim(21, 21.25)
ax_inset.set_xlabel('h')
ax_inset.set_ylabel(r"$g \; h^{-1} m^{-2}$")
ax2 = ax1.twinx()  # instantiate a second axes that shares the same x-axis
color = 'gray'
ax2.set_ylabel('Relative Humidity', color=color)  # we already handled the x-label with ax1
# ax2.plot(index, ypraw, c='lightgray')
ax2.plot(t/60/60, RH_np, color=color, linestyle='dashed')
ax2.tick_params(axis='y', labelcolor=color)
fig.tight_layout()  # otherwise the right y-label is slightly clipped
plt.show()

# plot the dimensionless length vs time and relative humidity
```

```
fig, ax1 = plt.subplots()
color = 'tab:blue'
ax1.set_xlabel('time (h)')
ax1.set_ylabel(r"Dimensionless Length", color=color)
ax1.plot(t/60/60, l/L_0, color=color)
ax1.tick_params(axis='y', labelcolor=color)
ax2 = ax1.twinx()  # instantiate a second axes that shares the same x-axis
color = 'gray'
ax2.set_ylabel('Relative Humidity', color=color)  # we already handled the x-label with ax1
# ax2.plot(index, ypraw, c='lightgray')
ax2.plot(t/60/60, RH_np, color=color, linestyle='dashed')
ax2.tick_params(axis='y', labelcolor=color)
fig.tight_layout()  # otherwise the right y-label is slightly clipped
plt.show()
```

Listing 6: Steady-State Solution Script

```
import numpy as np
import matplotlib.pyplot as plt
from scipy.optimize import fsolve, least_squares
from scipy.integrate import quad
from scipy.stats import linregress
from sympy import *
import pandas as pd

pi_0 = (89.9*1000)  # [Pa] osmotic modulus
phi_0 = 0.2  # [] initial polymer volume fraction
eta = 1e-3  # [Pa s] dynamic viscosity of water
v_w = 1.8e-5  # [m3/mol] molar volume of water
rho_w = 1000  # [kg/m3] density of water
rho_p = 1200  # [kg/m3] density of polymer
h = 0.0027  # [m/s] convective mass transfer
Cs = 0.022  # [kg/m3] mass concentration of saturated water vapour (25C)
K_0 = 9e-19  # [m2] permeability of swollen gel
beta = 2 / 3  # [] Kozeny-Carman equation like parameter for permeability
L_0 = 5e-3  # [m] initial thickness of the gel (5 mm)
R = 8.314  # [m3Pa/K/mol] Ideal Gas Constant
T = 298  # [K] system temperature
e = pi_0*v_w/(phi_0*R*T)

def perm(p):
    return K_0*(phi_0 / p)**beta

data = pd.read_csv('data.csv')
data_np = data.to_numpy()
print(data)
```

```
output = np.load('output.npy')
print(output)

res = linregress(output[:,1], output[:,0]*100)
print(f"R-squared:{res.rvalue**2:.6f}")
new_RH = res.slope * data_np[:,1] + res.intercept
# print(new_RH)
data_np[:,0] = new_RH

plt.errorbar(data_np[:,1], data_np[:,2], yerr=data_np[:,4], xerr=data_np[:,3],  fmt='o', markersize=8,
    capsize=3,  ecolor='gray', label='Experimental Data')
plt.ylabel(r'$L/L_0$', fontsize=18)
plt.xlabel(r'Steady State $n_w$ ($g\;h^{-1}m^{-2}$)', fontsize=18)
plt.tick_params(axis='both', which='major', labelsize=12)
plt.plot(output[:,1], output[:,2], 'k', label='Model with Experimental Parameters')
plt.legend()
plt.tight_layout()
# plt.show()

plt.errorbar(data_np[:,0], data_np[:,1], yerr=data_np[:,3],  fmt='o', markersize=8, capsize=3,  ecolor='
    gray', label='Experimental Data')
plt.ylabel(r'Steady State $n_w$ ($g\;h^{-1}m^{-2}$)', fontsize=18)
plt.xlabel(r'$RH_{room}$ Adjusted', fontsize=18)
plt.tick_params(axis='both', which='major', labelsize=12)
plt.plot(output[:,0]*100, output[:,1], 'k', label='Model with Experimental Parameters')
plt.legend()
plt.tight_layout()
# plt.show()

plt.errorbar(data_np[:,0], data_np[:,2], yerr=data_np[:,4],  fmt='o', markersize=8, capsize=3,  ecolor='
    gray', label='Experimental Data')
plt.ylabel(r'$L/L_0$', fontsize=18)
plt.xlabel(r'$RH_{room}$ Adjusted', fontsize=18)
plt.tick_params(axis='both', which='major', labelsize=12)
plt.plot(output[:,0]*100, output[:,2], 'k', label='Model with Experimental Parameters')
plt.legend()
plt.tight_layout()
# plt.show()


def obj(x):
    c = x[1]  # I think it needs to be greater then 0
    z = x[0]  # needs to be less than 0
    phi_fun = lambda y: (c**3 * y**3)/(27 * phi_0**2) + (c**2 * y**2)/(3*phi_0) + c*y + phi_0
```

```
    phi_diff_fun = lambda y: (3*c**3 * y**2)/(27 * phi_0**2) + (2*c**2 * y)/(3*phi_0) + c
    phi = phi_fun(z)
    print(f'phi_l{phi}')
    n_w = (h * Cs * (np.exp(-e * (phi_fun(z) - phi_0) / phi_0) - rh_room))  # convective flux out of
      domain
    flux = n_w  # Volumetric flux out of boundary (aka the darcy's flux)
    u_L = phi**(-2/3) * phi_diff_fun(z) *((K_0*pi_0)/(L_0*eta*phi_0**(1/3)))*1000
    mass = quad(phi_fun, 0, z)[0]
    # print(f'flux {flux}')
    # print(f'u_L {u_L}')
    # print(f'eq1: {(flux - u_L)/flux}')
    # print(f'MB = {(phi_0 - mass)/phi_0}')
    # print(f'c = {c}')
    # print(f'z={z}')
    # print('-'*5)
    return [(phi_0 - mass)/phi_0, (flux - u_L)/flux]


# print(obj([.001, 1]))
index = 2
rh_room = output[index,0]
roots = least_squares(obj, [.8, 0.61], bounds=([0, 0], [1,1.1]))
print(roots)
z = roots.x[0]
c = roots.x[1]
phi_fun = lambda y: (c**3 * y**3)/(27 * phi_0**2) + (c**2 * y**2)/(3*phi_0) + c*y + phi_0
phi_diff_fun = lambda y: (3*c**3 * y**2)/(27 * phi_0**2) + (2*c**2 * y)/(3*phi_0) + c
flux = (h * Cs * (np.exp(-e * (phi_fun(z) - phi_0) / phi_0) - rh_room))*3600*1000
u_L = (phi_fun(z)**(-2/3) * phi_diff_fun(z))*((K_0*pi_0)/(L_0*eta*phi_0**(1/3)))*3600*1000

print('-'*5)
print(f'flux calc = {flux}')
print(f'u_L calc = {u_L}')
print(f'flux actual = {output[index,1]}')
print('-'*5)
print(f'L calc {z}')
print(f'L actual = {output[index,2]}')
print('-'*5)
print(f'MD = {quad(phi_fun, 0, z)[0]}')
print(f'c2 = {c}')

print('-'*5)
print(f'phi at boundary = {phi_fun(z)}')
aw = np.exp(-e * (phi_fun(z) - phi_0) / phi_0)
print(f'water activity = {aw}')
```

Listing 7: Surface Coverage Analysis Script

```
# import packages
import numpy as np
import cv2 as cv
import os
import matplotlib as plt

"""
This code is part of the supplementary work for "Hydrogel-based Photobioreactor for Solid-State
    Cultivation of Chlorella Vulgaris"

This code looks at analyzing the surface coverage of algae in the hydrogel photobioreactor (hPBR).


--------

Some material in this code was taken (or modified) from the following source:
"How calculate the area of irregular object in an image (opencv)?" - Antonino La Rosa
https://stackoverflow.com/questions/64394768/how-calculate-the-area-of-irregular-object-in-an-image-
    opencv

"""



# Open Image and read it into uint8 data type (BGR data) & resize image to fit on screen
image = 'pPVAa4.jpg'  # image file name
img = cv.imread(image)
folder = image[:-4] # set folder name (here it is file name - extension (.jpeg)
folder_path = os.path.join(os.getcwd(), folder)
if not os.path.exists(folder_path):
    # If the folder does not exist, create it
    os.makedirs(folder_path)

print(img.shape)
img = cv.resize(img, (round(.25*img.shape[1]), round(.25*img.shape[0])))
assert img is not None,  "Did not read Correctly"

num = 2  # contour index in list to analyze (change value to counter of interest)

# convert image to gray scale and display it
gray_scaled_img = cv.cvtColor(img, cv.COLOR_BGR2GRAY)
# cv.imshow("new", new)
# cv.waitKey(0),
```

```
# using Canny edge detection.
edges = cv.Canny(gray_scaled_img, 190, 200) # threshold for edge linking
cv.imshow("Edge detection", edges)
cv.imwrite("{}/Edge_detection.png".format(folder), edges)
cv.imshow("img", img)
cv.imwrite("{}/img.png".format(folder), img)


# dilate the edges so they are more defined.
kernel = np.ones((2, 2))
imgDil = cv.dilate(edges, kernel, iterations=3) #
imgThre = cv.erode(imgDil, kernel, iterations = 3) #eroding edges may help make contours more
    defined
# cv.imshow("Dil", imgDil)
# cv.imshow("Erod", imgThre)

# Project the contour lines from the Canny method onto the original image
contours,       hierarchy = cv.findContours(imgThre, cv.RETR_TREE, cv.CHAIN_APPROX_SIMPLE)
# cv.drawContours(img, contours, -1, (0,255,0), 3)
# cv.imshow("w/ contours", img)

# make a list of the large contours so that the gel contour can be manually found.
a = []
cont = []
for con in contours:
    i = 0
    area = cv.contourArea(con)
    a.append(area)
    i += 1
    if area > 5000: # only look at contours larger than 5000 pixel^2
        perimeter = cv.arcLength(con, True)

        # smaller epsilon -> more vertices detected [= more precision]
        epsilon = 0.0002 * perimeter
        # check how many vertices
        approx = cv.approxPolyDP(con, epsilon, True)
        # print(len(approx))

        cont.append([len(approx), area, approx, con])

print(max(a))
print("---\nfinal number of contours:", len(cont))


# Removing Background
```

```
# Get Dimensions
hh, ww = img.shape[:2]

# draw white contour on black background to make a mask
mask = np.zeros((hh,ww), dtype=np.uint8)

#contour number that represents hydrogel.
# num = 1 # contour number
cv.drawContours(mask,[cont[num][2]], -1, (255,255,255), cv.FILLED)

# apply mask to image
image_masked = cv.bitwise_and(img, img, mask=mask)

# convert to HSV colouring
hsv = cv.cvtColor(image_masked, cv.COLOR_BGR2HSV)
# set lower and upper color limits
lowerVal2 = np.array([28,100,0])
upperVal2 = np.array([80,255,255])
# (120,100,0) (80,255,255) pPVAa0
light_green_mask = cv.inRange(hsv, lowerVal2, upperVal2)
# mask for dark greens
lowerVal3 = np.array([40,10,0])
upperVal3 = np.array([75,255,200])
# Threshold the HSV image to get only red colors
dark_green_mask = cv.inRange(hsv, lowerVal3, upperVal3)
not_dark_green = cv.bitwise_not(dark_green_mask)
light_green_mask = cv.bitwise_and(light_green_mask, not_dark_green)
final_mask = cv.bitwise_or(light_green_mask, dark_green_mask)
# apply mask to original image
final = cv.bitwise_and(hsv, hsv, mask=final_mask) # can change to other mask to visualize like
    dark_green_mask
# gray final image after applying mask
gray = cv.cvtColor(final, cv.COLOR_BGR2GRAY)
algae_area = cv.countNonZero(gray)
dark_green = cv.countNonZero(dark_green_mask)
print('percent-dark-green')
try:
   print(dark_green/algae_area*100)
except:
   print("area-is-0")

print("algae_area")
print(algae_area)
algae_coverage = algae_area / cont[num][1] * 100
print("Aglae-Coverage-%")
```

```
print(algae_coverage)


dst = cv.add(image_masked, final)
cv.imshow("final", final)
cv.imwrite("{}/final.png".format(folder), final)
cv.imshow("hsv", hsv)
cv.imwrite("{}/hsv.png".format(folder), hsv)
cv.imshow("over", dst)
cv.imwrite("{}/over.png".format(folder), dst)
cv.waitKey(0)
```

Listing 8: Scale Data Logging Script

```
import serial
import time
import csv
import schedule
from serial.tools import list_ports


def save_data():
    with open("test_data2.csv", "a") as f:
        writer = csv.writer(f, delimiter=",")
        t = time.time()
        writer.writerow([time.strftime('%Y-%m-%d-%H:%M:%S', time.localtime(t)), ser_bytes])


port = list(list_ports.comports(include_links=False))  # gives a list of ports on device
for p in port:  # the return is an object that holds details like name, description, location and interface
    print(p)

ser = serial.Serial(port='COM5',
                    baudrate=4800,
                    parity=serial.PARITY_NONE,
                    stopbits=serial.STOPBITS_ONE,
                    bytesize=serial.EIGHTBITS
                    )

schedule.every(1).seconds.do(save_data)

# ser.reset_input_buffer()
while True:
    try:
```

```
        ser_bytes = str(ser.readline())
        schedule.run_pending()
    except KeyboardInterrupt:
        print("Keyboard-Interrupt")
        break
```

Listing 9: Scale Data Analysis Script

```
import matplotlib.pyplot as plt
import pandas as pd
from scipy.stats import linregress
from scipy.signal import savgol_filter
import numpy as np
import csv
import numpy as np
from datetime import datetime
import matplotlib.pyplot as plt
from scipy import integrate
from scipy.fft import fft, ifft

# data = pd.read_csv("test_data_Nov2.csv")
# x = data["Time"].iloc[500:50000:10].astype(float).to_numpy()
# y = data["Mass"].iloc[500:50000:10].astype(float).to_numpy()
file = 'h_April30_1.csv'
xmn = 10  # from beginning
xmx = 4000  # from end
ss_min = 2000  # from beginning
ss_max = 6000  # from beginning

with open(file, 'r') as f:
    data = list(csv.reader(f, delimiter=","))
s = 0
x = []
date_str = data[0][0]
date_format = '%Y-%m-%d-%H:%M:%S'
start_time = datetime.strptime(date_str, date_format)
data = np.array(data)
y = []
for row in data:
    date_str = row[0]
    date_format = '%Y-%m-%d-%H:%M:%S'
    end_time = datetime.strptime(date_str, date_format)
    minutes = (end_time - start_time).total_seconds()
    temp_time = minutes
    row[1] = row[1].strip("rn-~Ove-'\-b-g-S")
    s += 1
```

```
    if s % 4 == 0:
        x.append(temp_time)
        try:
            y.append(float(row[1]))
        except:
            y.append(float(0))

print(len(x))
print(len(y))
print('-'*5)
print('graph range')
print(x[xmn])
print(x[-xmx])
hours = (x[-xmx] - x[xmn])/60/60
print(f'{hours:.2f} hours')
print('mass range')
print(y[xmn])
print(y[-xmx])
mass_range = y[xmn] - y[-xmx]
print(mass_range)
slope = ((y[-xmx] - y[xmn])/ hours)
print(f'slope = {slope:3f} g/h')


y1 = y[xmn:-xmx]
x1 = x[xmn:-xmx]
x1 = [i - x[xmn] for i in x1]
index = [_/60/60 for i, _ in enumerate(x1)]
# index = [i for i, _ in enumerate(x1)] # to plot the indices instead of time

#y1 = savgol_filter(y1, window_length=100, polyorder=3, deriv=0)
ypraw = savgol_filter(y1, window_length=2, polyorder=1, deriv=1, delta=(x1[1] - x1[0]))*60*60
yp = savgol_filter(y1, window_length=300, polyorder=1, deriv=1, delta=(x1[1] - x1[0]))*60*60


print("-"*5)
ss = np.sum(yp[ss_min:ss_max])/len(yp[ss_min:ss_max])
print(ss)
ss_f = ss*np.ones(len(x1))
timess = (x1[ss_max] - x1[ss_min]) / 60
print(f'{timess} minutes')

area = integrate.simpson(-yp,index)
print(f'area under curve: {area:3f}')
error = (area - mass_range)/ mass_range * 100
```

```
print(f'error is {error:2f} %')

# ypnew = yp
# fft_data = fft(ypnew)
# frequencies = np.fft.fftfreq(len(fft_data), d=x1[1]-x1[0])
#
# plt.figure(figsize=(10, 4))
# plt.plot(np.abs(frequencies[1:]), np.abs(fft_data[1:]))
# plt.title('Fourier Transform of Time Series Data')
# plt.xlabel('Frequency')
# plt.ylabel('Amplitude')
# plt.grid(True)
# plt.show()
# cutoff_frequency = 0.01/4
# fft_data_filtered = fft_data.copy()
# fft_data_filtered[np.abs(frequencies) > cutoff_frequency] = 0
#
# # Inverse Fourier transform to get denoised data
# denoised_data = ifft(fft_data_filtered)
#
# plt.figure(figsize=(10, 4))
# plt.plot(x1, ypnew, label='Original Data', alpha=0.7)
# plt.plot(x1, denoised_data, label='Denoised Data', linestyle='--', linewidth=2)
# #plt.plot(x1, yp, "--g")
# plt.title('Original vs Denoised Time Series Data')
# plt.xlabel('Time')
# plt.ylabel('Amplitude')
# plt.legend()
# plt.grid(True)
# plt.ylim((-3,0))
# plt.show()
#
# area = integrate.simpson(-denoised_data,index)
# print(f'area under curve: {area:3f}')
# error = (area - mass_range)/ mass_range * 100
# print(f'error is {error:2f} %')


fig, ax1 = plt.subplots()
color = 'tab:red'
ax1.set_xlabel('time (h)')
ax1.set_ylabel('mass (g)', color=color)
ax1.plot(index, y1, color=color)
# ax1.plot([x1[0]/60/60, x1[-1]/60/60], [y1[0], y1[-1]], '-g')
ax1.tick_params(axis='y', labelcolor=color)
```

```
ax2 = ax1.twinx()  # instantiate a second axes that shares the same x-axis



color = 'tab:blue'
ax2.set_ylabel('Derivative (g/h)', color=color)  # we already handled the x-label with ax1
# ax2.plot(index, ypraw, c='lightgray')
ax2.plot(index, yp, color=color)
ax2.plot(index, ss_f, 'k')
ax2.plot([x1[0]/60/60, x1[-1]/60/60], [slope,slope], '-g')
ax2.set_ylim(-3, 0)
ax2.tick_params(axis='y', labelcolor=color)
ax2.set_title(file)
fig.tight_layout()  # otherwise the right y-label is slightly clipped

plt.show()


# xt = np.array(x[2000:-8000])
# yt = np.array(y[2000:-8000])
#
# xp = np.array(x[500:-7000])
# yp = np.array(y[500:-7000])
#
# regr = linear_model.LinearRegression()
# regr.fit(xt.reshape(-1,1),yt.reshape(-1,1))
# y_pred = regr.predict(xt.reshape(-1,1))
# print(regr.coef_[0])
# print(regr.intercept_)
# r = r2_score(yt, y_pred)
# print(r)
# equation = "m = {:.2E}t + {:.2} \n R$^2$ = {:.3}".format(regr.coef_[0][0], regr.intercept_[0], r)
#
# # result = linregress(x, y)
# # slope = result.slope
# # inter = result.intercept
# # r2 = result.rvalue
# # x_fit = np.linspace(10000, 40000, 100)
# # y_fit = slope*x_fit + inter
# # equation = "m = {}t + {}".format(round(slope,5) ,round(inter,3))
# # print(inter)
# # print(r2)
#
# plt.rcParams.update({'font.size': 14, "figure.figsize": (7, 5)})
# plt.plot(xp,yp, "gray", xt, y_pred, "r")
```

```
# plt.xlabel("Time (s)")
# plt.ylabel("Mass (g)")
# plt.ylim(50,90)
# plt.text(0.52*xp[-1], 85, equation)
# plt.show()
# print(equation)
#
```

Figure A.1 is an example of the diffusion rate analysis. The red line is the scale measured mass data, while the blue line is the smoothed flux rate (mass derivative). The black line is the estimated steady-state flux.

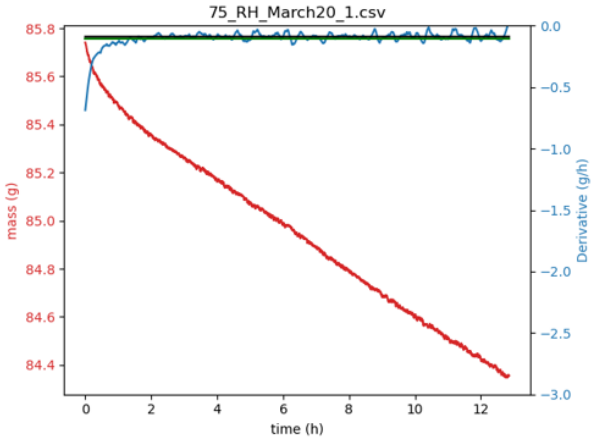

Figure A.1: Scale Data Analysis Example

						SS estimate range		g/h	g/h/m2	minutes	%	Thickness (mm)			Average Values			
date	RH	trail	x min	- x max	time graphed (h)	min	max	SS	SS	time range	mass int error	Initial	final	L/L0	SS rate	thickness		
2024-03-13	0	1	680	10	3.92	1000	1350	-0.514936086	-223.8852547	34.78	2.09	0.49	0.28	0.571429				
2024-03-14	0	2	750	10	4.24	1000	1800	-0.307985051	-133.9065438	111.46	2.14	0.55	0.36	0.654545				
2024-03-15	0	3	10	10	7.59	1200	3000	-0.333318486	-144.9210807	139	0.87	0.52	0.28	0.538462				
2024-03-18	0	4	250	10	6.65	2000	3000	-0.226000753	-98.26119683	139	-3.84	0.49	0.26	0.530612	-150.244	0.573762	7.788454	0.056685
2024-03-20	75	1	1650	10	12.85	1800	4000	-0.088697459	-38.56411281	306.02	-7.38	0.5	0.37	0.74				
2024-03-21	75	2	10	10	17.93	5000	70000	-0.181297765	-78.8251152	278	1.96	0.51	0.43	0.843137				
2024-03-25	75	3	400	100	20.03	5000	7000	-0.118066927	-51.33344652	278	-7.86	0.54	0.47	0.87037				
2024-03-25	75	3	120	10	23.86	5000	7000	-0.167990693	-73.03943195	278	-5.48	0.48	0.38	0.791667	-54.3123	0.800679	17.42964	0.065651
2024-04-03		Al Test	10	10	24.95	100	7000	-0.01626885	-7.073412935	960.1	6.16							
2024-04-04	33	1	10	2200	20.13	2000	8000	-0.110703853	-48.13211004	833	-3.34	0.52	0.34	0.653846				
2024-04-05	33	2	250	10	21.16	2000	8000	-0.146059123	-63.50396649	833	3.92	0.48	0.28	0.583333				
2024-04-06	33	3	40	1400	28.08	2000	8000	-0.18488729	-80.38577845	832.51	4.399	0.49	0.33	0.673469				
2024-04-07	33	4	10	10	23.41	2000	80000	-0.180265513	-78.37631002	832.51	3.597	0.49	0.31	0.632653	-79.381	0.629819	9.221534	0.045135
2024-04-09	93	1	ISSUE															
2024-04-10	93	2	150	5000	9.03	2500	3500	-0.041335488	-17.97195135	138	-7.04	0.43	0.39	0.906977				
2024-04-11	93	3	750	100	7.21	0	1500	-0.035222967	-15.3143336	209	-15.19	0.48	0.44	0.916667				
2024-04-12	93	4	10	10	23.41	8000	10000	-0.167318191	-72.74703954	227.55	1.332	0.43	0.39	0.906977				
2024-04-13	93	5	100	100	20.34	4000	7000	-0.041603135	-18.08831959	417	-7.34	0.43	0.4	0.930233	-17.1249	0.917959	1.569048	0.011006
2024-04-17	53	1	180	10	20.84	3000	8000	-0.145334504	-63.18891491	695	0.7248	0.43	0.33	0.767442				
2024-04-18	53	2	150	10	22.88	3000	8000	-0.100083917	-43.51474674	695	-6.88	0.43	0.27	0.627907				
2024-04-19	53	3	130	10	23.63	3000	8000	-0.137531166	-59.79615904	695	-7.141	0.35	0.26	0.742857				
2024-04-20	53	4	250	10	23.92	3000	8000	-0.136859747	-59.50423794	693	3.136	0.44	0.3	0.681818				
2024-04-21	53	5	200	10	20.89	4000	8000	-0.121001893	-52.60951874	555.58	4.3	0.47	0.3	0.638298	-58.7747	0.707604	4.437355	0.058571
2024-04-23	10	1	10	100	22.18	3000	7000	-0.169557859	-73.72080811	555	4.87	0.45	0.27	0.6				
2024-04-24	10	2	10	10	20.31	500	2500	-0.269393862	-117.1277659	277	3.1	0.45	0.25	0.555556				
2024-04-26	10	3	100	10	22.17	5000	9000	-0.225418194	-98.00791059	555	2.806	0.33	0.22	0.666667				
2024-04-27	10	4	100	10	21.31	5000	9000	-0.246307772	-107.0903358	555	2.355	0.45	0.26	0.577778	-107.409	0.6	9.563902	0.048005

Table A.9: Mass transfer data